2016

Structure and Dynamics of Layered Transition Metal Compounds Driven by Broken Symmetry

Chen Chen
Louisiana State University and Agricultural and Mechanical College, cchen22@lsu.edu

STRUCTURE AND DYNAMICS OF LAYERED TRANSITION
METAL COMPOUNDS DRIVEN BY BROKEN SYMMETRY

A Dissertation

Submitted to the Graduate Faculty of the
Louisiana State University and
Agricultural and Mechanical College
in partial fulfillment of the
requirements for the degree of
Doctor of Philosophy

in

The Department of Physics and Astronomy

by
Chen Chen
B.S., University of Science and Technology of China, 2009
May 2016

Acknowledgments

Freshly coming out of college, I would never imagine this is how my graduate school life would be like. The seven years of study at LSU is such an important part in my life that it shaped me mentally. While enjoying the moment that this period is reaching an end, I will never forget the days and nights when I was having no clue about future and thinking deeply. It is definitely the help of countless people that pushed me forward, whom I would like to acknowledge here.

First, I want to thank my advisor, Prof. Ward Plummer, for his scientific insight and guidance leading me through the whole journey. Being a pure scientist from the old generation, his calm but persistent and honest way of doing science sets up the standard for me to pursue every single goal in my future. Working in Ward's group is a unique experience with infinite possibilities to realize my own ideas along with even more experiences knowing when things do not work. Without his encouragement I could never imagine I can persist for the seven years.

I would thank Prof. Jiandi Zhang for teaching me the fantastic and profound physics concepts, as well his hospitality and assistance for me and my wife during our hard time. I would also thank Prof. Rongying Jin for her supply of high quality samples, and her and Dr. Zhang's effort to build up the family like environment for the whole group. I would acknowledge my committee: Prof. Phillip Sprunger for his passionate explanation of EELS and support of fixing the instrument, and Prof. Andrew Maverick for his advice on this thesis. I give special thanks to Prof. Jiandong Guo from Institute of Physics in China for introducing me to this field and his encouragement to me so that I realize I will not regret any single decision that I make.

Experimental physics research is such a complicated process that no one can make grate achievements singly with his/her own diligence. Fortunately I have been taught by so many experts in their fields. I would like to thank Dr. Jing Teng for her initial guidance to bring me into the field of surface physics, Dr. Von Braun Nascimento for his help in LEED experiment and calculation, and Dr. Jisun Kim for her help in STM experiments. I acknowledge the help from Oak Ridge National Laboratory for the four-probe measurements: Prof. An-Ping Li, and Dr. Corentin Durand. Also the help from LSU electronic shop and machine shop for their help: Randy Gould, Douglas smith, Donnie Olano, Vincent Vaughn, Brandon Amos; the secretaries from main office: Arnell Nelson, Shemeka Ezeff, Ophelia Dudley, etc.

I made many true friends out of my colleagues: Fangyang Liu with whom I have the friendship for eleven years and counting, Dr. Hangwen Guo who shines me with his brilliant ideas, Mohammad Saghayezhian the professor-to-be with great minds, and all the LSU tigers: Zhenyu Diao, Lina Chen, Yifan Yang, Gaomin Wang, Xiaobo He, Biao Hu, Jianneng Li, Guorong Li, Weimei Xie, Guixin Cao, David Howe, Joel Taylor, Yi Li, Zhaoliang Liao and his wife Lin Li, Dalgis Mesa, and Zhenyu Zhang.

I save my final thanks for my wife Qianxi Yang and my family. It is their support to keep me calm and patient, make wise decisions and not give up. Also they are the reason that I could achieve my doctorate, and will always be the reason that I do anything for.

Table of Contents

List of Tables

List of Figures

Abstract

Correlated Electron Systems have attracted attention because of their complex phase diagrams that often contain several exotic phases that cannot be understood at all with traditional ideas. This is driven by the competition between many low-lying states, competing to be the ground state. That means by tuning parameters like temperature, pressure, magnetic field, or doping concentration, one phase would be suppressed and another emerges. These phases are in such a delicate balance that they compete and interact with each other, and experimentally we can always find a way to alter this balance. In this work, two systems have been investigated: Fe-based superconducting compounds ($Ba(Fe_{1-x}Co_x)_2As_2$) and doped strontium ruthenates ($Sr_3(Ru_{1-x}Mn_x)_2O_7$). It is going to be shown that the broken symmetry at the surface disturbs the balance, offering new couplings for both systems.

The discovery of Fe-based superconductors in 2008 with a superconducting transition temperature higher than 55 K has generated great interest in the materials community in 2008. This superconducting family is based on the conducting layers of iron and pnictides (typically phosphorus or arsenic) and/or chalcogenide (typically selenium or tellurium). In this study, we focus on one compound of this family: $Ba(Fe_{1-x}Co_x)_2As_2$, where giagantic phonon frequency change with temperature and a higher phase transition temperature has been observed at its

surface. This anomalous surface lattice dynamics indicates a strong surface-spin-charge-lattice coupling.

Another system is the Rudelesden-Popper transition metal ruthenates with $Sr_{n+1}Ru_nO_{3n+1}$. This family is a classical example with strong coupling between charge (orbital), spin, and lattice. The specific compound in this study is Mn doped $Sr_3(Ru_{1-x}Mn_x)_2O_7$. In the bulk, $Sr_3Ru_2O_7$ shows metamagnetic quantum critical point behavior under magnetic field and low temperature [20]. Under pressure it shows ferromagnetic (FM) order with enhanced magnetic moment, indicating the ground state has FM instability [21]. With Mn doping there is a metal-to-insulator transition starting from $\sim 5\%$ [22], whose transition temperature is strongly coupled to the octahedral rotation. Through quantitative surface structure determination we found the surface phase of $Sr_3Ru_2O_7$ is dramatically different from the bulk with the enhanced octahedral rotation and the emergence of tilt. The surface metallicity is also studied through the phonon spectra mediated through the electron-phonon coupling. The asymmetry of the phonon peak is analyzed through the Fano line-shape, which is due to the interaction between the discrete phonon excitation with the electron-hole pairing continuum. With increasing Mn concentration the peak becomes more asymmetric, indicating the surface is more metallic with higher density of states near the Fermi energy. The surface of $Sr_3Ru_2O_7$ is less metallic and presumably antiferromagneticaly ordered while the bulk is metallic. In contrast, the surface of $Sr_3(Ru_{0.84}Mn_{0.16})_2O_7$ is metallic while the bulk is insulating. These unusual properties are intimately coupled with the surface structure.

Chapter 1
Introduction

1.1   Background: Correlated Electron Systems

The past few decades have seen extensive amount of discoveries of materials with novel properties, such as colossal magnetoresistance (CMR), high temperature superconductivity (HTSC), metal-to-insulator transitions (MIT), and quantum critical point (QCP) behaviors. This leads to tremendous effort both experimentally and theoretically to understand the physics behind these materials, which cannot be explained without involving principles of quantum mechanics and bringing down the scale into atomic level. These phenomena share a common character, which is the strong electron-electron interactions in such material systems. Although the fundamentals of magnetism, ferroelectricity, and superconductivity are known, it is still a grand challenge to understand the behaviors of systems made of large number (10^{23}) of particles interacting with each other (many-body problem) [23]. Therefore the correlated electron materials locate at the forefront of condensed matter physics research. Such materials usually exhibit complexity with distinct properties under different experimental conditions, such as temperature, pressure, magnetic field, and doping levels. This leads to a variety of exotic phase diagrams.

1.2   Phase Diagram of Superconducting Families: Cuprates and Fe Pnictides/Chalcogenides

One of the most famous example of correlated electron system is the cuprates which is HTSC containing copper anions. Originally discovered in 1986 in the Ba-La-Cu-O system with superconducting transition temperature higher than 30 K [24], cuprates draw great attention within the following decades and reached the highest temperature above the liquid nitrogen boiling point in this family

($HgBa_2Ca_2Cu_3O_x$, $Bi_2Sr_2Ca_2Cu_3O_{10}$, $YBa_2Cu_3O_7$, *etc*). The mechanism for super-conductivity in this family is still under debate after 30 years of research attempt, although certain common behaviors have been identified. One thing for sure is that it cannot be explained by the BCS theory for the conventional metallic supercon-ductors. Figure 1.1(a) is a schematic phase diagram of such compounds [25]. The undoped parent compounds are antiferromagneticaly (AFM) ordered Mott insu-lators. By changing the parameter x, which is usually the electron or hole doping level, the material becomes superconducting at low temperature. Note that in this situation often the superconductivity is achieved by killing the AFM order in the parent compound. Beyond these two phases there is another pseudogap phase, which is similar to a true gap but has non-zero density of states near the Fermi energy.
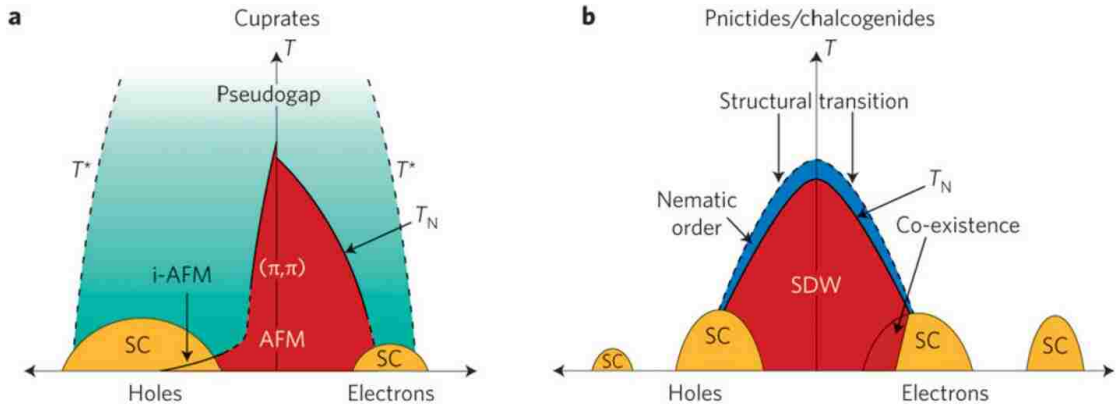
FIGURE 1.1: Schematic phase diagrams of (a) cuprates and (b) pnictides. Figure is adapted from [25].

In comparison, a general phase diagram of the Fe based superconductors is shown in Fig. 1.1(b). This type of materials were first discovered in 2008 by Kamihara *et. al.* [26]. In contrast to the copper and oxygen layer in cuprates, the new HTSC materials consist of iron and pnictides (arsenic or phosphorus) or chalcogenides (se-lenium or tellurium). The parent compound is AFM ordered metal, and becomes

superconducting with doping or pressure. This material is tetragonal at high temperature (HT) and orthorhombic at low temperature (LT). Close to the structural transition there is another magnetic transition from the HT paramagnetic state to the LT AFM state. (Whether or not it is a spin density wave phase is still under debate.)

The above two HTSC examples have shown that these compounds have superficially similar phase diagrams, where the superconductivity is achieved through doping. Possibly because of the suppression of the AFM order from the induced carriers. Further doping will kill the superconductivity because of the disorder. The doping sites for electrons and holes are often different using chemical replacement of element with another valence or deficiency of an element such as oxygen. For instance, from Fe pnictides parent compound $BaFe_2As_2$ the electron doping is usually by replacing Fe with Co [27] and the hole doping is usually by replacing Ba with K [28]. Since the superconducting layer in this system is the Fe-As layer, different doping sites will cause different effects for the same electron/hole level, and the phase diagrams shown in 1.1 are asymmetric. Tuning of the material parameters using pressure can also change the superconducting transition temperature T_c drastically. For example there is a large positive coefficient of T_c in the La-Ba-Cu-O system [29]. Another example is in Fe chalcogenides, where the high pressure can bring the T_c from 8 K to 36.7 K [30]. In fact, isovalent chemical substitution is considered a way of introducing external pressure ("chemical pressure"). For example replacing the La with the smaller isovalent Y leads to T_c higher than liquid nitrogen temperature in the Y-Ba-Cu-O cuprate [31]. Also substitution of Se with Te or S can enhance the T_c of the FeSe compound [32].

However the properties of their parent compounds along with the phases outside the superconducting regime are quite different. A big difference here is that there is
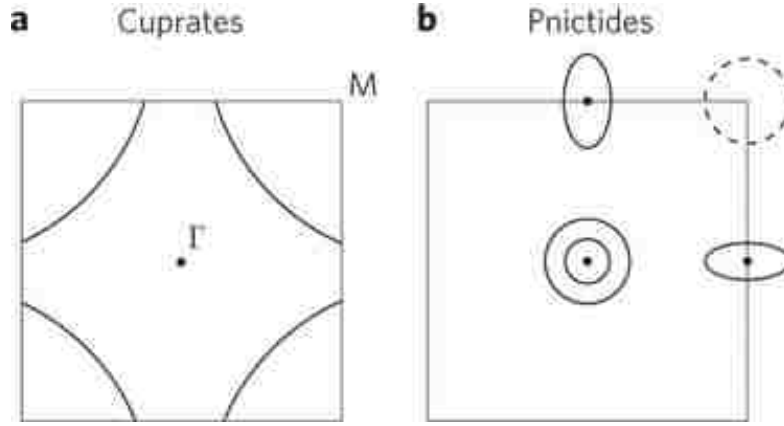
FIGURE 1.2: Schematic Fermi surfaces of (a) cuprates and (b) Fe pnictides. Figure is adapted from [25].

coexistence of the AFM order and superconductivity in such compounds, especially on the electron doped side. The Fe based superconductors also lack unexplained 'mystery' phases like the pseudogap and never become insulating throughout the phase diagram. Also their corresponding Fermi surfaces inside the superconducting regime have different number of sheets at different locations shown in Fig. 1.2 [25]. Cuprates have one Fermi surface while Fe pnictides have multi-bands and most compounds have five Fermi surfaces. This implies the interactions between the electrons of these materials are different, which leads to various ground state under certain conditions. The different interactions result in possibly different pairing mechanisms, which is fundamental to the superconductivity, and yet is still under debate. To answer this question, it is necessary to find out the reason behind each phase, that is, to identify each type of interaction and the cooperating & competing nature between them.

1.3 Ruddlesden-Popper Ruthenates

Another prototype correlated electron system is the Ruddlesden-Popper (RP) ruthenates $Sr_{n+1}Ru_nO_{3n+1}$ ($n = 1, 2, 3, ...\infty$) with structure shown in Fig. 1.3. The basic building block of this series of compound is the RuO_6 octahedra like perovskites. The Sr atoms locate at the cage sites surrounding the octahedra. The

dimensionality parameter n determines the number of octahedra stacking along the c-axis. This is a layered structure because there is a fairly large gap separating each octahedra stacking. Thus the interlayer interactions are relatively small, resulting in a quasi 2D system. Between the two stackings there is also a lateral shift of half tetragonal unit cell along the ab-plane along the diagonal direction, so the nearest neighbor of the top Sr atom of one stacking is the bottom O atom of the other stacking. When $n = \infty$, there are infinite octahedra in one stacking and the system becomes the perovskite structure.
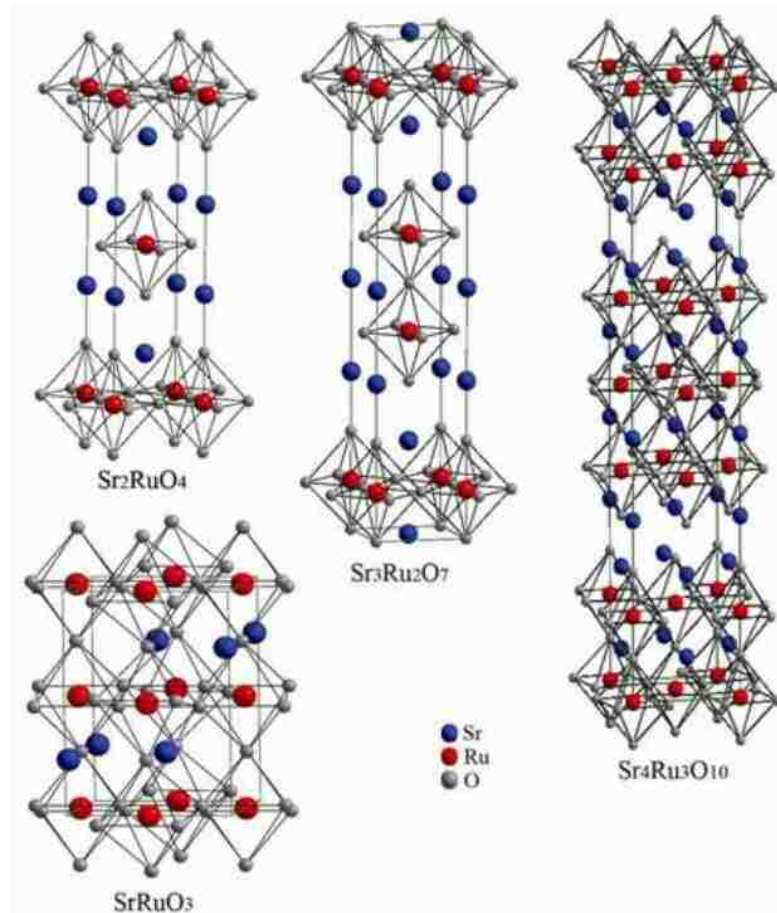
FIGURE 1.3: Crystal structures of RP series of layered perovskites.

Like other correlated electron systems the phase diagram is very complicated, especially when the dimensionality n plays a role. Figure 1.4 systematically shows

the different phases of the undoped compounds of this series. It presents various electronic and magnetic phases associated with different n. The number of exchange interactions per transition metal ion, mediated through n, systematically decreases from 6 for $n = \infty$ to 16/3 for $n = 3$, to 5 for $n = 2$, and finally 4 for $n = 1$ [33]. As a result, the exchange interactions and conductivity perpendicular to the Ru-O planes reduces as the in-plane conductivity of Ru-O layer increases.
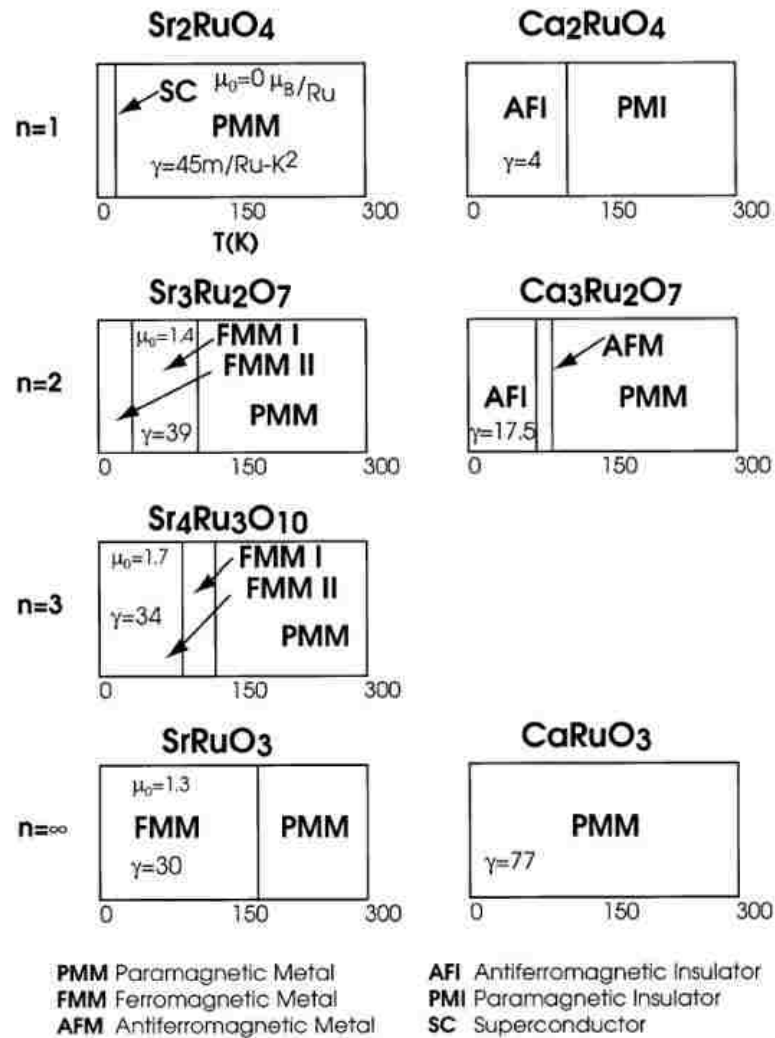
FIGURE 1.4: Different phases of the RP series. γ is the electronic specific heat coefficient and μ_0 is the magnetic moment. Figure is adapted from [33].

The $n = 1$ family $Ca_{2-x}Sr_xRuO_4$ is one of the most studied compound in the RP series, whose bulk and surface phases have been thoroughly explored [34, 35, 12]. The details of the various phases will be introduced below.

1.3.1 Bulk Structure of $Ca_{2-x}Sr_xRuO_4$

Sr_2RuO_4 has a unit cell shown in Fig. 1.6, which resembles La_2CuO_4, the parent compound of the $La_{2-x}M_xCuO_4$ (M can be Ca, Sr, Ba) superconducting cuprates. The building block is the RuO_6 octahedron with the Ru atom locates in the center. Each octahedron is surrounded by the 8 Sr atoms sitting at the corner of a cube. The whole lattice is constructed by stacking this single octahedral layer along the c-axis direction, with a displacement of (a/2, a/2, 0) against each layer, where "a" is the in-plane lattice vector.
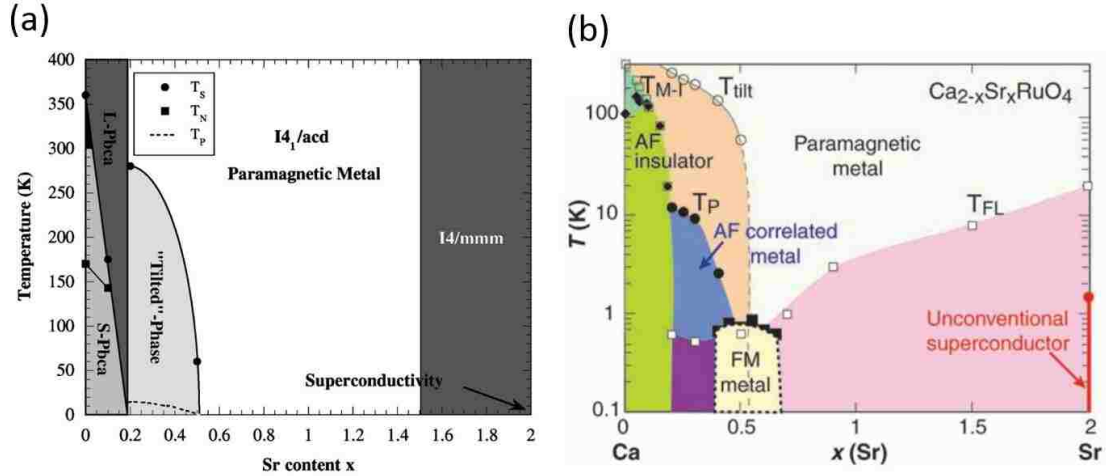
FIGURE 1.5: Phase diagram of the single layered ruthenates $Ca_{2-x}Sr_xRuO_4$. (a) Structural phase diagram. (b) Electronic and magnetic phase diagram. Figures are adapted from [34, 35, 36].

Substituting Sr by Ca is isovalent, because the two elements have the same valence. In this situation, the change in structure is mainly due to the chemical pressure induced from the size difference. The structural phase diagram is shown in Fig. 1.5(a). Starting from the undistorted Sr_2RuO_4 where $x = 2$ (right end point of the phase diagram), the unit cell is tetragonal with $I4/mmm$ space group, shown

in Fig. 1.6. With more Ca the lattice distorts in such a way that mainly involves the octahedral rotation and tilt. This movement involving the octahedra is displayed in Fig. 1.7. A single octahedron is shown in Fig. 1.7(a).

The lattice remains tetragonal with $I4/mmm$ space group until $x \sim 1.5$, when the octahedra start to rotate. Shown in Fig. 1.7(b) is the top view of such lattice. The reason for the lattice distortion originates from the reducing of the lattice parameters because of the smaller ionic size of Ca. With the overall lattice shrinking, the octahedra behave like a rigid body, thus they rotate along the c-axis in order to keep the same volume. Without rotation the red dashed square in Fig. 1.7(b) is the unit cell, with rotation the unit cell the black solid square is the new unit cell, which is $(\sqrt{2} \times \sqrt{2})R45°$ with a $I4_1/acd$ space group. This new lattice structure persists till $x > 0.5$, with larger rotational angle with increasing Ca doping level.

The octahedral tilt emerges when $x < 0.5$ at low temperatures. This tilt is shown in Fig. 1.7(c), where the octahedra rotate around an axis parallel to its edge. Similar to rotation, the appearance of tilt is to relieve the extra strain from the cage outside the octahedra due to more Ca doping. Usually the tilt starts when the rotational angle reaches around $\sim 12°$, which is also the critical condition that an extra distortion from the octahedra is required. With this distortion the O1 atoms mainly move along the c-axis and the O2 atoms along the ab-plane. The new lattice belongs to the orthorhombic $Pbca$ space group. Note that from the phase diagram Fig. 1.5(a) there is a structural transition from the high temperature tetragonal (HTT) to the low temperature orthorhombic (LTO) phase, where the transition temperature increases with more Ca in the compound. In other words, the structure is more distorted with more Ca. The end product Ca_2RuO_4 stabilizes the orthorhombic phase throughout the temperature range. One single layer of this orthorhombic lattice with both rotation and tilt is shown in Fig. 1.7(d).
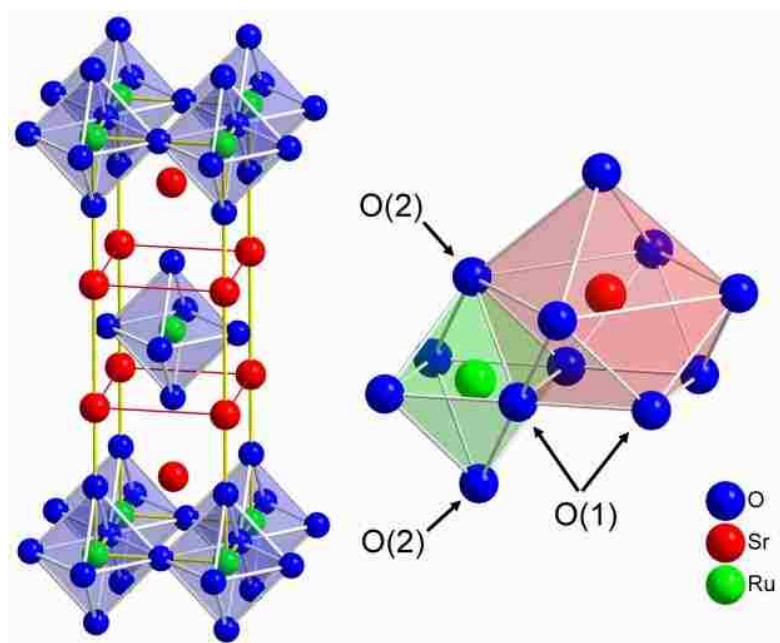
FIGURE 1.6: The unit cell and building block of parent Sr_2RuO_4. Figure is adapted from [12].
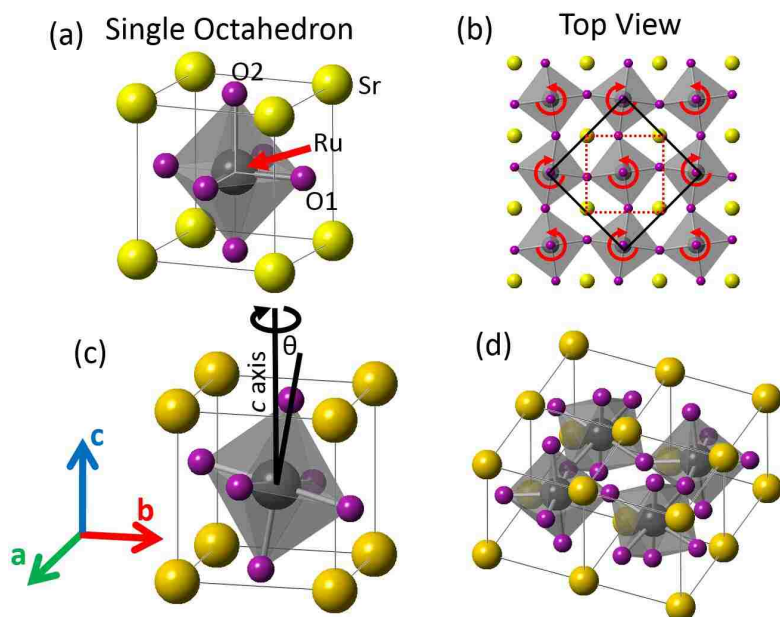
FIGURE 1.7: Octahedral rotational and tilt distortion of the $Ca_{2-x}Sr_xRuO_4$.

Significant phonon softening has also been observed through inelastic neutron scattering, indicating the structural instability. There are two modes in concern: a Σ_3 mode associated with octahedral rotation and a Σ_4 mode associated with octahedral tilt. In Sr_2RuO_4 there is an obvious drop in Σ_3 phonon energy (softening) near the zone boundary, shown in Fig. 1.8 [3]. This Σ_3 mode is a E_u mode which starts at 8.2 THz at Γ point and softening continuously in the Brillouin zone towards the [110] direction. The red curve is the dispersion of this softened phonon. Because of its interaction with an optical branch and an acoustic branch with the same symmetry, there is hybridization between the branches, resulting in the measured dispersion in Fig. 1.8.
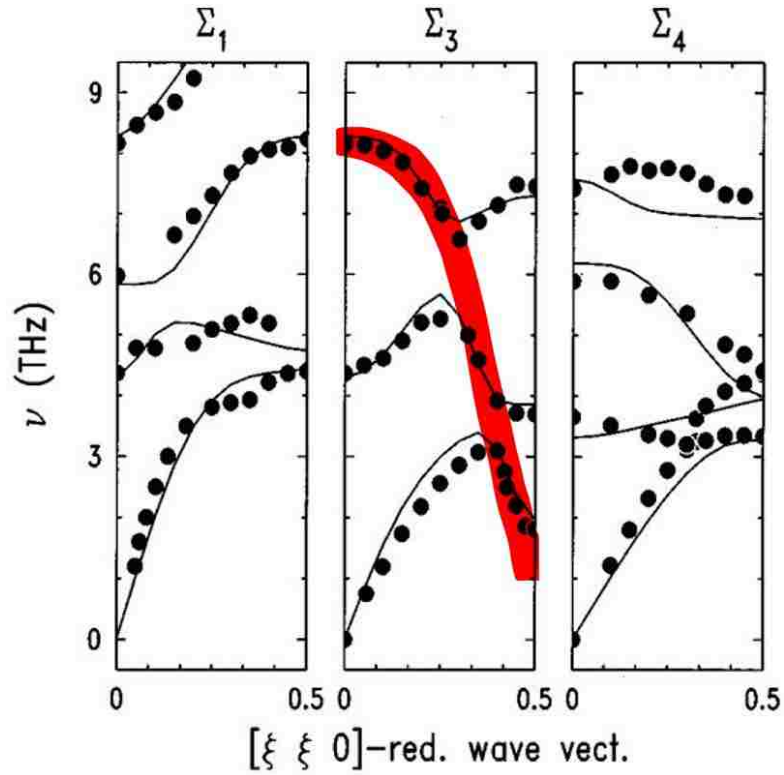
FIGURE 1.8: Phonon dispersion in Sr_2RuO_4. Phonon dispersion along [1 1 0]. Figure is adapted from [3].

The tilt structural instability happens at the doping level $x \sim 0.5$. For doped sample x=0.4 and 0.6, there is a comparison for the phonon softening but on Σ_4

mode, shown in Fig. 1.9 [37]. There are two types of phonons, Σ_4 mode (filled symbols) and anomalous mode (open symbols). The Σ_4 mode for the x=0.6 sample softens but never freezes to zero energy even at the lowest temperature. This same mode for the x=0.4 sample freezes to zero energy at 150 K below the structural transition temperature. The anomalous modes never freezes to zero energy at all doping levels and temperatures, which is explained through the intrinsic disorder from the stacking faults along the c-axis. Because of the weak inter-layer interaction, this disorder may occur with rotated and tilted octahedra stacking. Such disorder can lift the degeneracy of a phonon propagating along the ab-plane, resulting in non-zero value at the zone boundary.
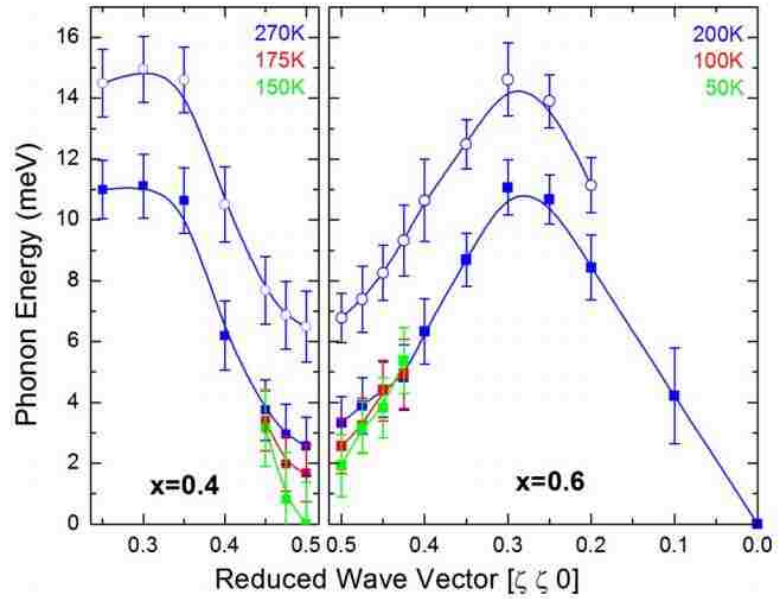
FIGURE 1.9: Phonon dispersion of Σ_4 mode in $Ca_{2-x}Sr_xRuO_4$ for x=0.4 and 0.6. There are two types of phonons, Σ_4 mode (filled symbols) and anomalous mode (open symbols). Figure is adapted from [37].

When an phonon mode goes to zero in energy, such as the 150 K phonon for the x=0.4 sample in Fig. 1.9, there is going to be a structural transition. For example, this soften phonon branch is symmetric with respect to the 0.25 wave vector. This means the original Brillouin zone spits into two Brillouin zones with the same size,

half of the original one. Meanwhile in real space the size of the unit cell doubles, which is a $2\times$ reconstruction along the direction of the corresponding wave vector. For $Ca_{2-x}Sr_xRuO_4$ the softening happens along the [110] direction, so that the reconstruction is $(\sqrt{2} \times \sqrt{2})R45°$ where along [110] direction the unit cell size is doubled.

1.3.2 Bulk Phases of $Ca_{2-x}Sr_xRuO_4$

Sr_2RuO_4 is a superconductor with transition temperature of 1.5 K [38]. Nuclear Magnetic Resonance (NMR) Knight-shift and Muon Spin Relaxation (μ-SR) measurements show that this is a spin triplet p-wave superconductor [39, 40]. Spin polarized neutron scattering also suggests the odd-parity pairing [41]. Unlike the cuprates La_2CuO_4 where the superconductivity is achieved through doping the Mott insulator, the pure Sr_2RuO_4 not only is superconducting, but also starts from a metallic state. In fact, its superconductivity is extremely sensitive to the impurities. A small amount of defects could suppress the transition temperature drastically [42].

The pureness of the sample makes it suitable for the de Haas-van Alphen (dHvA) measurements, where the Fermi velocity indicates the enhancement of the effective electron mass by a factor of 3-5 [7, 43]. The linear temperature dependence of the specific heat and the T^2 behavior of the resistivity also show that the parent Sr_2RuO_4 can be described by the Landau Fermi-liquid theory [44, 38], where the interactions between electrons become important.

The Fermi surface is also measured by angle resolved photoemission spectroscopy (ARPES) and calculated by local-density approximations (LDA), shown in Fig. 1.10. The electron-like β sheet centered at Γ, formed by d_{yz} and d_{zx} band, is projected to have peculiar behavior when perturbed [7, 43, 6]. Calculations show that this sheet can be changed into a hole-like sheet around X when the Fermi

level is shifted to higher energies [6]. Therefore there is a saddle point created when two bands meet each other, causing the electron density of states (DOS) diverge logarithmically. Such a point is called a Van Hove singularity (VHS), which often gives an enhancement in all two dimensional electronic properties because of the enhanced transition rate by the Fermi's golden rule. Currently in Sr_2RuO_4 the VHS is still above the Fermi energy [6].

Both the dHvA measurements and LDA calculations show a Fermi surface with two electron sheets and one hole sheet [7, 43, 6]. The early ARPES measurements suggest one electron sheet and two hole sheets [45, 46]. This issue was resolved after realizing a surface reconstruction [47] and the band folding in the ARPES results. The unfolded Fermi surface is shown in Fig. 1.10(left).
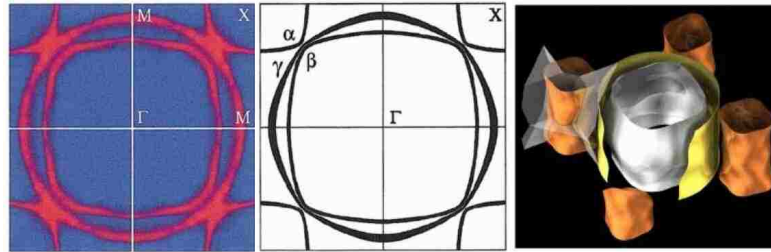
FIGURE 1.10: Fermi surface of Sr_2RuO_4. Fermi surface is determined from ARPES (left), LDA calculations (middle), and dHvA experiment (right). Figure is adapted from [4, 5, 6, 7].

Replacing the Sr with Ca can change the electronic properties more dramatically than expected for isovalent doping. The phase diagram is summarized in Fig. 1.5(b). The high temperature phase is still a paramagnetic metal, but with more Ca the transition temperature to the Fermi liquid reduces. More importantly, there is a MIT when $x < 0.2$. The transition temperature increases as x becomes smaller, stabilizing the insulating phase.

Such phase transitions can be understood through a band splitting model shown in Fig. 1.11 [48]. The rotational distortion narrows the bandwidth and enhances the

VHS, but does not lift the degeneracy of the d_{yz} and d_{zx} bands. With further doping the tilt distortion breaks the four-fold symmetry and lifts the degeneracy between the d_{yz} and d_{zx} bands. Here the xy band is fully occupied and the yz/zx bands are partially-filled. The onsite Coulomb repulsion opens the gap and stabilizes the Mott insulator state according to the LDA + U calculation [48].
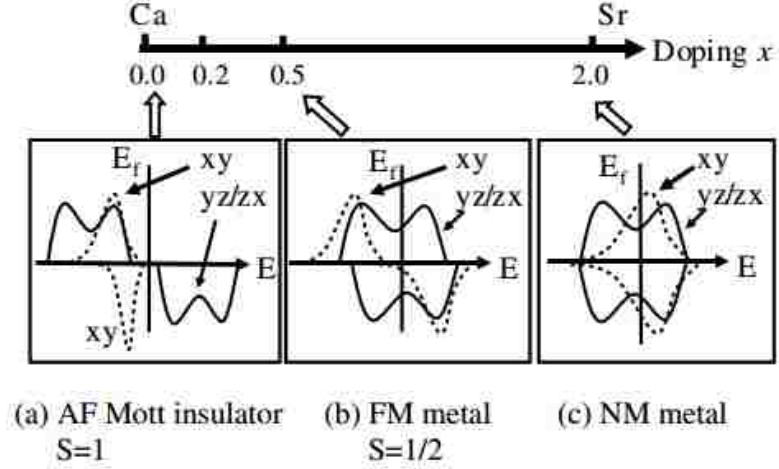
FIGURE 1.11: Schematic variation of the electronic configuration in $Ca_{2-x}Sr_xRuO_4$ calculated using LDA + U. Figure is adapted from [48].

Various magnetic states can also be established by different Ca/Sr concentrations. At room temperature Sr_2RuO_4 is a paramagnetic (PM) metal. Early nuclear magnetic resonance (NMR) measurements indicated FM fluctuations [49], which is also supported by LDA calculations [6]. Further investigations suggest the coexistence of FM and AFM fluctuations, where the AFM fluctuation is incommensurate based on inelastic neutron scattering measurements and theoretical calculations [50, 51, 52]. This AFM fluctuation is also projected to support the p-wave pairing [53].

The competition between the FM and AFM fluctuations become more evident with more Ca, resulting in a magnetic cluster glass region at low temperature around $x \sim 0.5$, shown in Fig. 1.5(b). When x becomes slight smaller than 0.5,

the system enters into a short range AF correlated state, suggesting possible QCP behavior at zero temperature. Meanwhile the high temperature state still keeps PM. For $0 < x < 0.2$, the system's ground state is AF ordered insulator. The magnetic transition temperature T_N is ~ 110 K for Ca_2RuO_4 [54, 34].
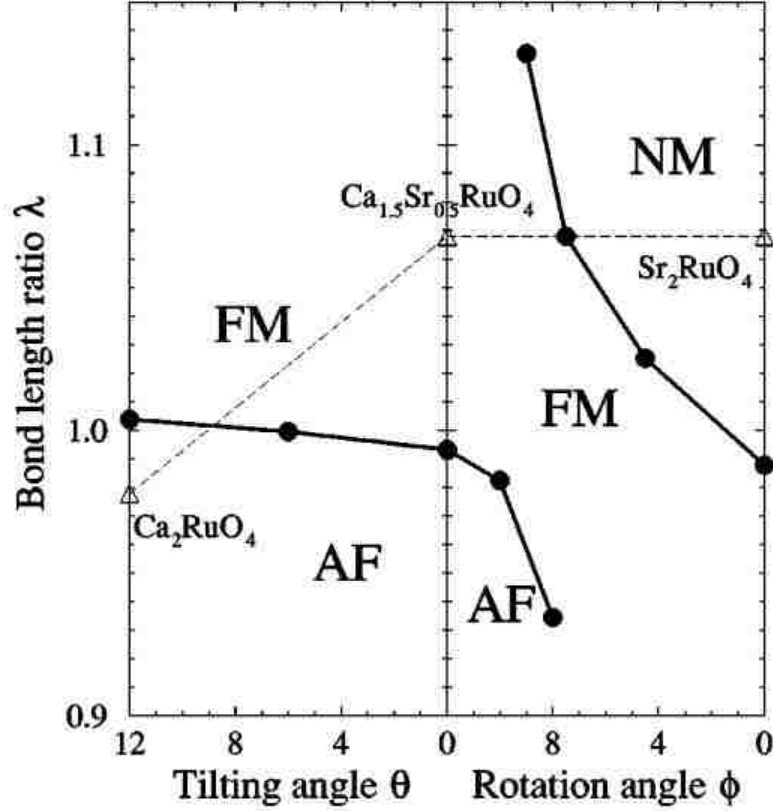
FIGURE 1.12: The calculated magnetic phase diagram of $Ca_{2-x}Sr_xRuO_4$ with structural distortions. Figure is adapted from [8].

It has been shown above that the structural, electronic, and magnetic properties are intimately coupled to each other, and can be tuned by two parameters of the doping level and temperature. This relationship can be summarized in a theoretically calculated phase diagram shown in Fig. 1.12 [8]. According to this phase diagram, the octahedral rotation and the tilt are responsible for the FM and AFM, respectively.

1.4 Coupling between Charge (Orbital), Spin, and Lattice

The previous examples have presented the complexity in correlated electron systems, which is the result of competition between several simultaneously active degrees of freedom. To understand this competition, it is beneficial to start with the fundamental properties of the electrons and multiple types of interactions.

An electron has intrinsic properties of charge $(-e)$ and spin $(\pm\frac{1}{2})$. The wave-particle duality from quantum mechanics states its wave-like behavior, which can be described by a wavefunction. This wavefunction is the probability density distribution of an electron, also known as atomic orbital for a single electron surrounding an ion core. In a single crystalline solid the atoms are stacked in a periodic manner, where the periodic ion cores form the lattice. In such case, the Bloch theorem states that the eigenstates for an electron in a crystal can be written as Bloch waves (a plane wave times a periodic function with the same periodicity as the crystal), which is the foundation of the concept of electronic band structures. The interactions between the coupling of charge, spin, orbital, and lattice degrees of freedom produces the complex phases.

There are different types of electron interactions coexisting in a solid, and the physical properties are determined by which one prevails and dominates. For example, in transition metal oxides, Coulomb repulsion prevents electron from hopping, tends to localize a single electron at lattice sites. Meanwhile the hybridization of the transition metal d electrons with the oxygen p electrons tend to delocalize the electrons. The strongly correlated systems are defined based on the inter-particle interaction. Assume W sets the scale of the energy band width and U measures the interaction strength. When $U/W > 1$ the system's Hamiltonian with N particles cannot be described as the sum of N one-particle Hamiltonians (mean-field ap-

proximation). In such systems, several interactions come into play and determine the system's property. These interactions are described below.

The magnetic property is determined by the spin magnetic moments, where the exchange interaction of the spin function is the quantum mechanical origin of magnetism. In transition metal oxides, there are two magnetic exchange mechanisms (different than the exchange interaction) that can strongly affect the overall magnetism of the materials. One of them is the double exchange shown in Fig. 1.13(a), originally proposed by Zener in 1951. In this situation, the two Mn ions have different valences. The spin-up electron from O hops to the empty Mn^{4+} e_g orbital, then another spin-up electron from the Mn^{3+} e_g orbital hops to fill the vacant O orbital. In this picture an electron moved between the neighboring ions without changing the spin direction. This mechanism favors FM metallic state. Another mechanism is the super exchange shown in Fig. 1.13(b), originally proposed by Kramers and Anderson. The example shown here is 180° of the Mn-O-Mn bond angle with the two Mn cations having the same valence. There is a magnetic interaction between the two Mn ions even though separated by a non magnetic O ion. In super exchange, the electrons do not actually move between the two metal positive ions. Thus this 180° favors the AFM insulating state. The competition of the coexisting FM metallic and AFM insulating phases is the key component for the colossal magnetoresistance (CMR) manganites, where the presence of magnetie field can have orders of magnitude change in resistivity [55, 36].

The crystal structure determines the orbital configurations for the transition metal d electrons. The octahedral environment of the oxygen will lift the five-fold degeneracy of the d-orbitals, splitting into a higher energy two-fold e_g level and lower energy three-fold t_{2g} level, shown in Fig. 1.14 (free ion to cubic).
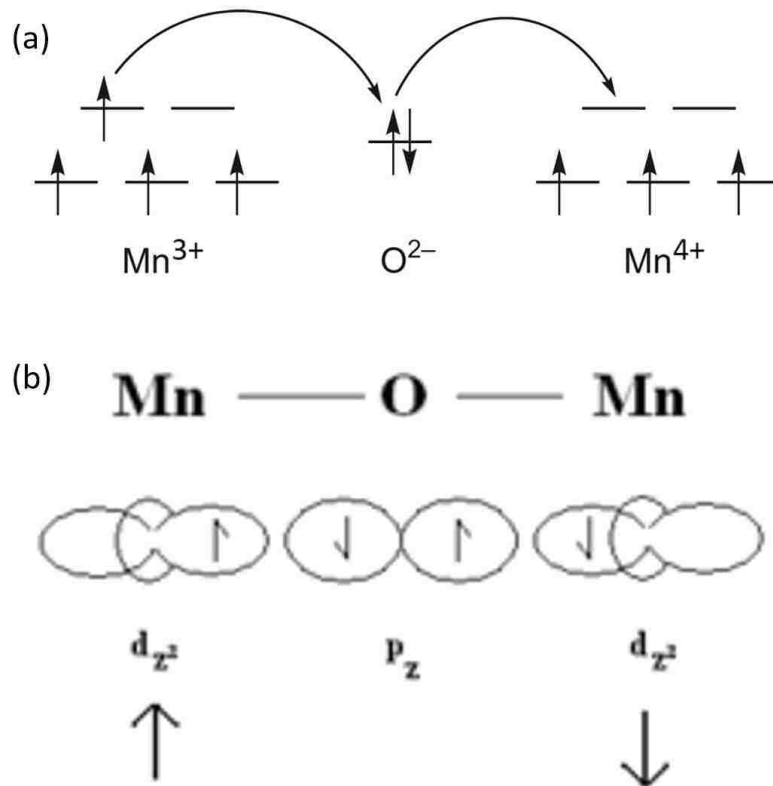
FIGURE 1.13: Magnetic exchange mechanism in manganites. (a) Doulbe exchange.
(b) Super exchange.

There is also another type of lattice distortion called Jahn-Teller distortion. In manganites $R_{1-x}A_xMnO_3$ (R is a rare earth element La, Nd, or Pr; A is an alkali earth metals Ca, Sr, or Ba), the octahedra elongate to reduce the Coulomb repulsion between the oxygen ions along the c-axis. This is accompanied by a compression of the octahedra along the ab-plane, with enhancement of in-plane Coulomb repulsion. The distortion is presented in Fig. 1.14 (cubic to tetragonal) The overall energy of the system is lowered compared to the undistorted structure. Such lattice distortion caused by the modified electron Coulomb interaction is called Jahn-Teller distortion [56]. In $Ca_{2-x}Sr_xRuO_4$, there is flattening of the octahedra which in order to stabilize the magnetic ground states [34, 8].
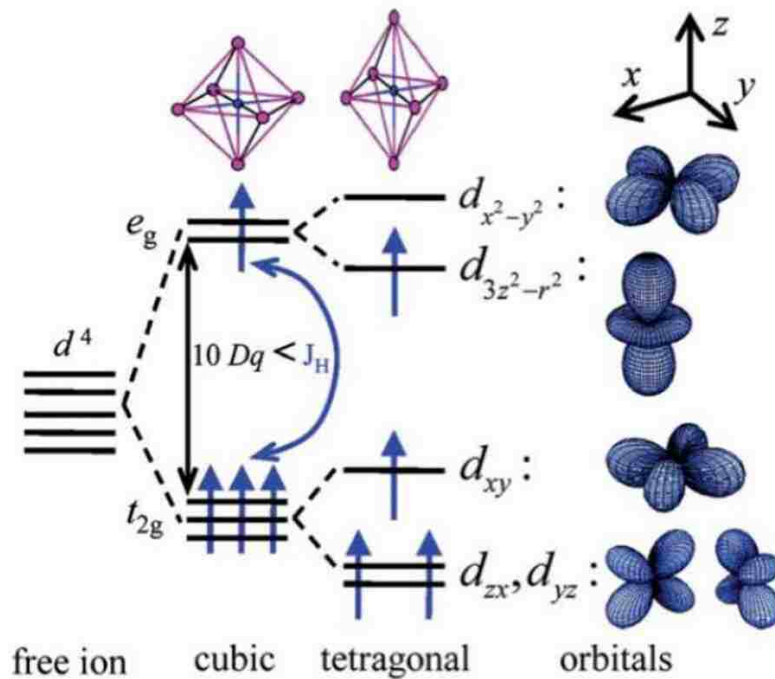
FIGURE 1.14: Schematic representation of the energy levels of the d-orbitals. The 5 degenerate energy levels are splitted by crystal field and Jahn-Teller distortion. Figure is adapted from [57].

In a real solid, the charge (orbital), spin, and lattice degrees of freedom are simultaneously important and one cannot simply describe the system with only

one or a few of them. The overall ground state stays at the delicate balance of their competition, that is why a weak external perturbation can create a large response. Therefore understanding the behavior of such system remains a grand challenge in condensed matter physics, meanwhile it offers a great opportunity to investigate and establish the physics behind their exotic properties.

1.5 Surface with Broken Symmetry

Wolfgang Pauli said "God made solids, but surfaces were the work of the devil.". Consider a solid with 10^{24} atoms, each side near its surface will have $\sim 10^8$ atoms. The surface has properties that resemble the bulk, but the unique environment of broken symmetry usually produces peculiar properties, serving as the playground of solid state physics.

1.5.1 Surface Electronic Behavior: Surface States

When a solid material terminates, there is a sharp transition from the bulk to the vacuum. There are localized electronic states living in the gap between the valence and conduction bands. Other conditions may also cause surface states such as dangling bonds, defects, adsorbates, surface reconstruction, etc [58].

Igor Tamm first predicted the existence of surface states in 1932 through calculation in the framework of a tight-binding model [59]. In 1939 William Shockley used nearly free electron approximation to show that surface states arise as solutions to the Schrdinger equation with modified potential due to bulk termination [60].

The Shockley states can be obtained using the following steps. First assuming the potential inside the crystal takes a cosine function with amplitude $2V$, while the potential at the surface takes a simple step function with height V_0 (1.1). This potential energy is shown in Fig. 1.15.
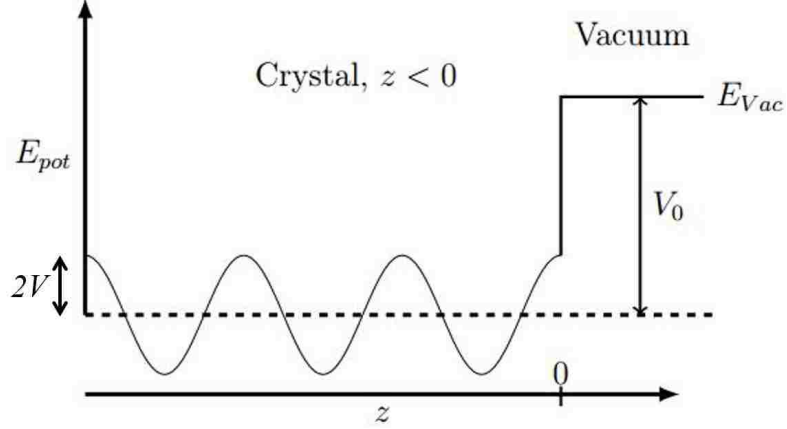
FIGURE 1.15: Potential energy at the surface.

$$V(z) = \begin{cases} V\left(e^{\frac{2\pi i z}{a}} + e^{-\frac{2\pi i z}{a}}\right) = 2V\cos\left(\frac{2\pi z}{a}\right), & z < 0 \\ V_0 & , \quad z > 0 \end{cases} \tag{1.1}$$

On one hand deep inside the crystal, the cosine function is chosen so that there is a band gap with width $2V$ in the band structure, shown in Fig. 1.16. Away from the Brillouin zone boundary the solution is a plane wave with parabolic dispersion. At the Brillouin zone boundary the solution is a standing wave composed of an incoming and a Bragg-reflected wave. The wavefunction takes the following form (1.2):

$$\psi_0 = Ae^{ikz} + Be^{i[k-(2\pi/a)]z} \tag{1.2}$$

Adapting this potential into the Schrodinger equation, the energies and eigenfunctions can be solved precisely for the bulk states with k near the zone boundary $k = \pi/a + \kappa$. On the other hand the wavefunction outside the crystal into the vacuum takes an exponential decaying form (1.3):

$$\psi_0 = De^{-\sqrt{\frac{2m}{\hbar^2}(V_0 - E)}z} \tag{1.3}$$
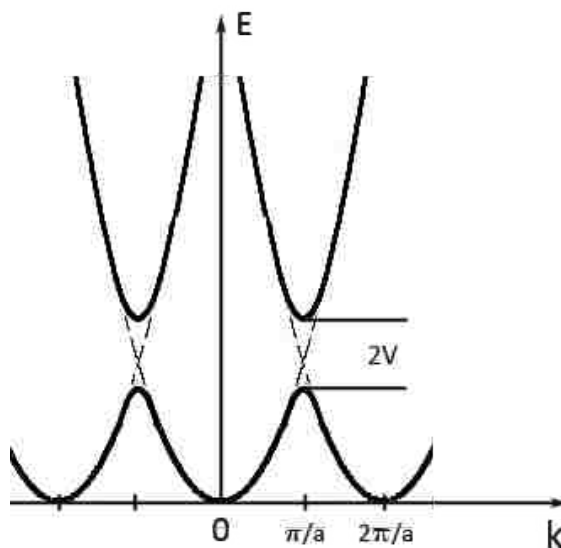
FIGURE 1.16: Electronic band structure in a crystal with cosine potential.

Matching the boundary conditions there are two possible solutions shown in Fig. 1.17: (1) If the κ parameter mentioned above is real, the wavefunction takes the form of an extended Bloch wave within the crystal with an exponentially decaying tail outside the surface, shown in Fig. 1.17(a). The corresponding energy levels lie in the bulk energy band. (2) If κ is imaginary, the wavefunction takes solutions with complex wave vectors. Such state can be viewed as bound states in a potential well and the wavefunction takes the form shown in Fig. 1.17(b). This is known as a Shockley state, which is localized at the surface, and decays both into the crystal and into the vacuum. All energies of this state are in the forbidden gap of the bulk band structure in Fig. 1.16.

In comparison, the surface states calculated using tight-binding model is called Tamm states. In this framework, the emergence of surface states can be understood via the change of atomic bondings and orbitals. Refer to [59] for more details.

The surface lattice still owns translational symmetry along the directions parallel to the surface plane. Therefore the surface states have Bloch type components with the same 2D periodicity. In addition, the surface states with energies in the gap

22
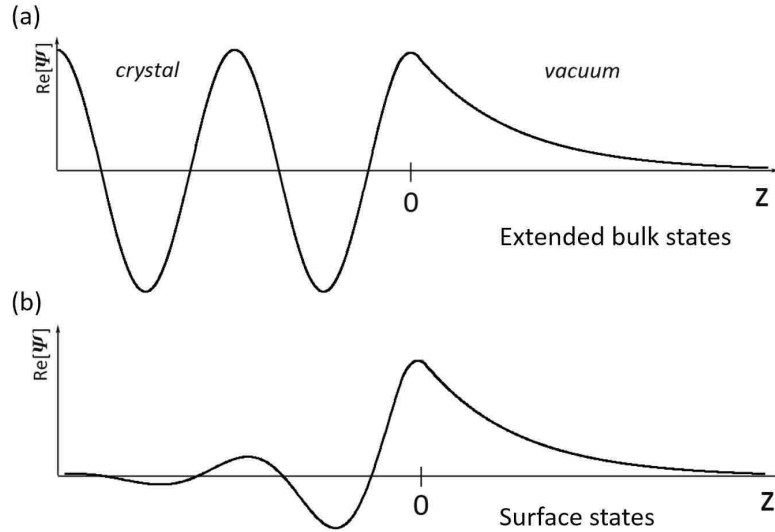
FIGURE 1.17: Two possible solutions of the Schrodinger equation with potential in 1.1. (a) Bulk-like solutions. (b) Surface state solutions.

penetrates a finite distance into the bulk, but the ones mixed with the bulk bands can propagate deep, forming a surface resonance.

The projection of a face centered cubic 3D Brillouin zone to a 2D Brillouin zone is shown in Fig. 1.18(a). The projection of the 3D bulk bands to a 2D surface is shown in Fig. 1.18(b), where shaded area is the filled states and the empty area is the place where a true surface state stays at. The comparison of surface states and surface resonance is shown in Fig. 1.19(a). The wave function of the surface resonance still decays in the vacuum, but penetrates indefinitely into the bulk. The surface state on Cu(111) is shown in Fig. 1.19(b) using ARPES [61].

One final word about the surface states is associated with the topology. Once the materials are classified with the topological invariant, there is an important consequence that there is going to be the existence of the gapless conducting states at interfaces where the topological invariant changes [62]. This rule serves as the fundamental of the surface states of topological insulators, which has generated great interest in recent years.
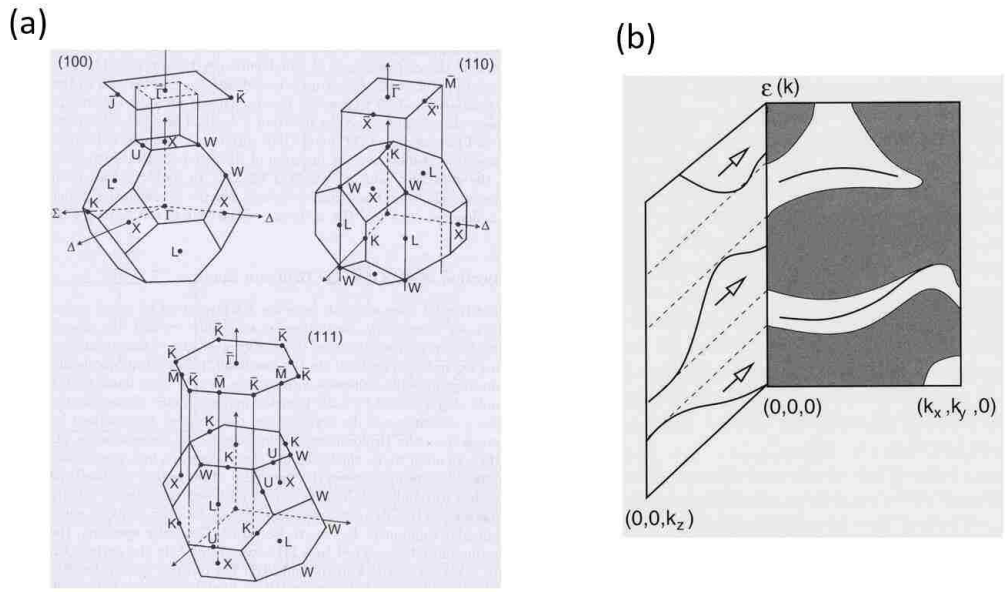
FIGURE 1.18: Projection of Brillouin zone and bulk bands to the surface. (a) Brillouin zone. (b) Bulk bands.
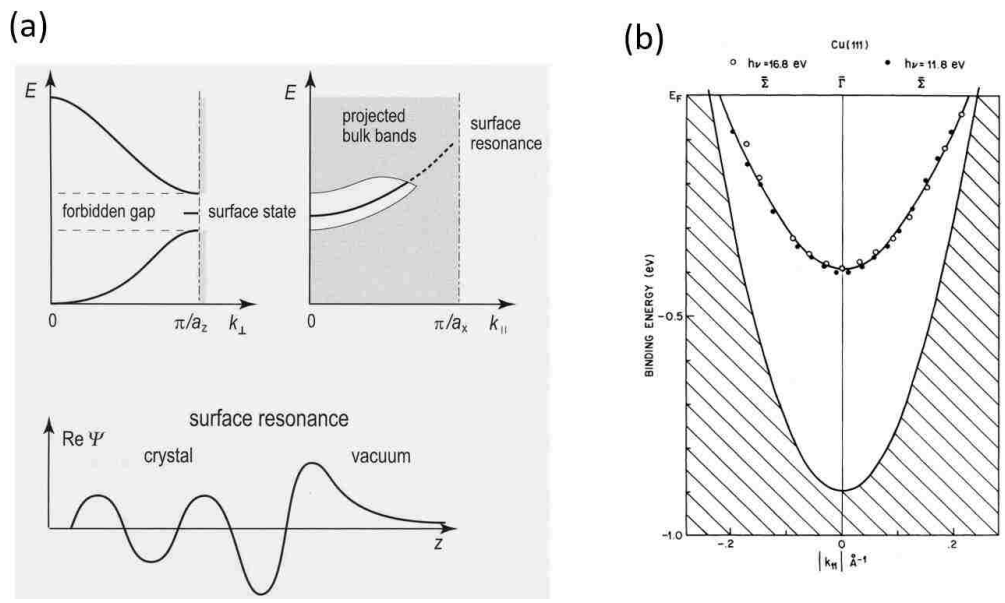
FIGURE 1.19: (a) Surface states and surface resonance. (b) Measured surface states of Cu(111) using ARPES. Figure is adapted from [61].
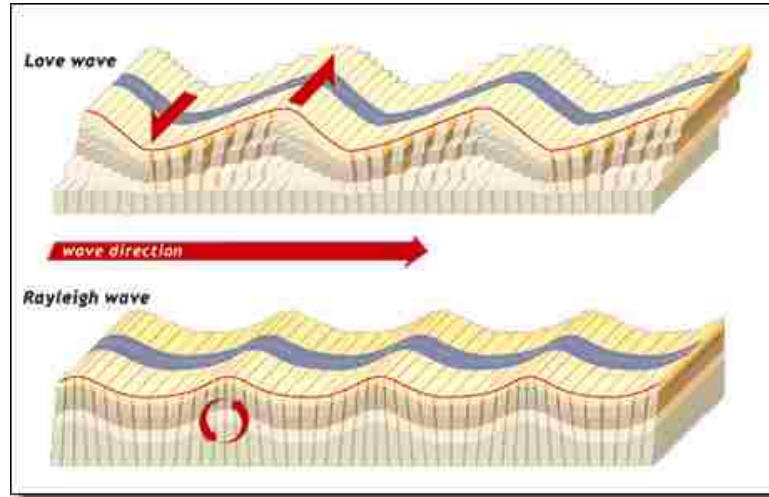
FIGURE 1.20: Two types of surface acoustic waves: Love wave (up) and Rayleigh wave (down).

1.5.2 Surface Phonon Behavior: Rayleigh Modes and Fuchs-Kliewer Modes

The movement of surface acoustic phonons can be understood in analogy to the surface seismic waves in geology. Shown in Fig. 1.20 are the two types: Love wave and Rayleigh wave, named after the people who predicted them, respectively. In Love wave the motion of the particles are shear horizontal, therefore it is definitely a transverse wave. In constrast, the motion in Rayleigh wave actually follows ellipses in planes normal to the surface and parallel to the direction of propagation. In other words, it is a mixture of the transverse and longitudinal waves depending on which has the largest relative amplitude.

Because of the movement inside the scattering plane for the Rayleigh modes, it is suitable for the surface phonon measurement. Two common experimental techniques for surface phonon dispersion measurement are high resolution electron loss spectroscopy (HREELS) and He atom scattering (HAS). For instance, Fig. 1.21 shows the phonon dispersion of Rayleigh wave on the Ni(100) surface [9]. Circles and squares are the experimental data, while the solid line is the calculated dispersion with force constant from the bulk value. After adjusting the force constant
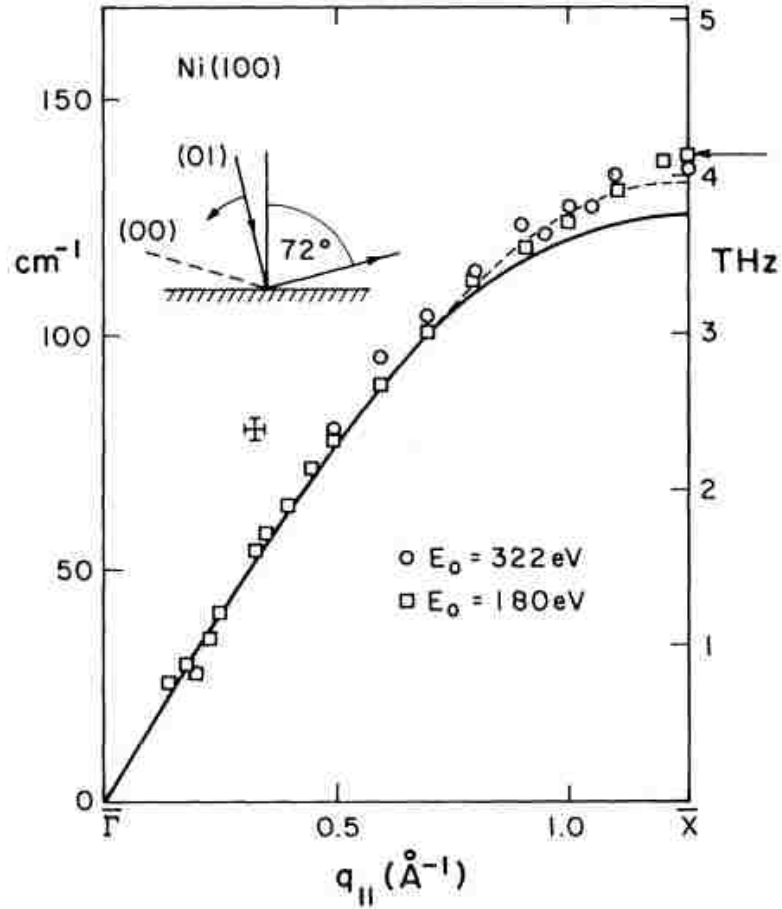
FIGURE 1.21: Phonon dispersion of Rayleigh wave on the Ni(100) surface. Figure is adapted from [9].

by a 20% increase between the first and second layers, the obtained dashed curve matches the experimental data better. Such higher than the bulk Rayleigh phonon energy at the zone boundary is observed for most metal surfaces. Originally this was interpreted through an increase of the force constant between first and second layer, or the tensile stress at metal surfaces, both lead to a stiffening of the Rayleigh wave frequency. For compressive stress, on the other hand, often causes softening of Rayleigh wave frequency.

However, first-principle calculation on the surface slabs shows that the surface Rayleigh wave energies can be understood very well without changing the force constants. In analogy to the bulk electronic bands, the bulk phonon bands can also

be projected to the surface Brillouin zone. Shown in Fig. 1.22 is the projection of the bulk phonon bands onto the Be(0001) surface [63]. The surface Rayleigh mode locates below the bulk bands and matches perfect with HREELS measurements.
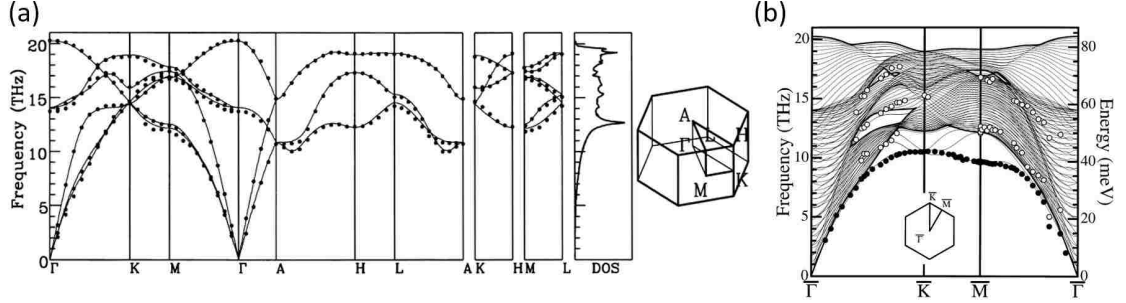
FIGURE 1.22: Bulk and surface phonon bands. (a) Calculated phonon bands of Be. (b) Projected bulk bands with the surface bands on the Be(0001) surface. Full and open circles are HREELS data. Figure is adapted from [63].

In contrast, surface optical phonon behaves differently, resulting in the so-called Fuchs-Kliewer (FK) modes in ionic crystals [64]. For an optical phonon, different atoms in a single unit cell move in opposite directions. For ionic compounds such as metal oxides, there is going to be strong electric filed when the positive and negative ions moving in opposite directions, creating the dipole field. The optical phonon mode associated with such movement and strong field has large energy.

The energies of the optical phonon can be estimated through the real part of the dielectric function $\epsilon(\omega)$. Shown in 1.23 is the dielectric function at different frequencies [10], when the real part becomes zero the corresponding frequency values are the optical phonon energies. Note in some tutorials this dielectric function diverge at the energy of the transverse optical phonon ω_{TO}. Meanwhile this dielectric function always crosses zero at the energy of the longitudinal phonon ω_{LO}. The value zero originates from the Maxwell's equation where $\nabla \cdot D$ vanishes when there is no net charge.
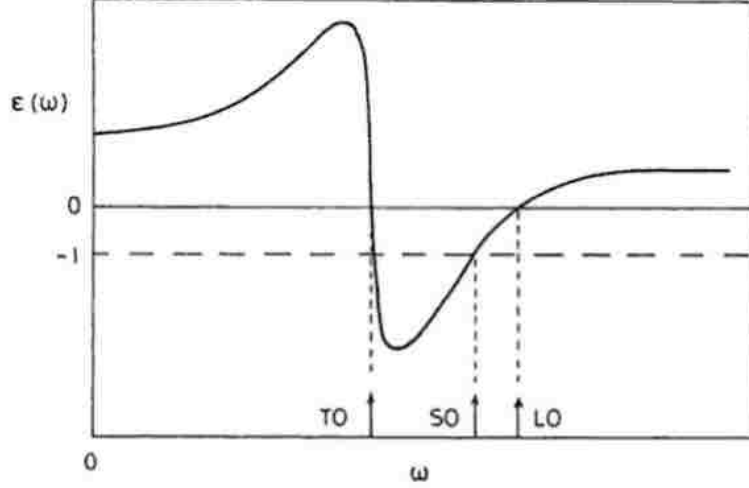
FIGURE 1.23: Real part of the dielectric function with frequency. Figure is adapted from [10].

The condition of the surface optical phonon is when $\epsilon(\omega) = -1$ proposed by Fuchs and Kliewer[64]. Shown in Fig. 1.23 the energy of the FK mode is always between ω_{TO} and ω_{LO}. The Lyddane-Sachs-Teller relation determines the ratio of ω_{TO} and ω_{LO} is

$$\frac{\omega_{LO}}{\omega_{TO}} = \sqrt{\frac{\epsilon_0}{\epsilon_\infty}} \qquad (1.4)$$

In comparison, the relationship between ω_{TO} and ω_{FK} is

$$\frac{\omega_{FK}}{\omega_{TO}} = \sqrt{\frac{\epsilon_0 + 1}{\epsilon_\infty + 1}} \qquad (1.5)$$

The dispersion of the FK mode is rarely discussed or measured. The main reason is that HREELS is most sensitive to this phonon mode along the c-axis when the analyzer is at specular direction, which means the momentum transfer is zero. There is a measurement on the GaAs(100) surface that maps out the whole $\Gamma - X$ direction, which shows the FK band is flat [65].

28

1.6 Probing the Surface with Combination of Techniques: Example of $Ca_{2-x}Sr_xRuO_4$

Study of $Ca_{2-x}Sr_xRuO_4$ is a classical example of applying many tools to probe the surface with different behavior than the bulk. Two major results are presented here.

1.6.1 Surface Structural Analysis and Phase Diagram: $Ca_{2-x}Sr_xRuO_4$

The surface structure of Sr_2RuO_4 was first studied by low energy electron diffraction (LEED), where a $(\sqrt{2} \times \sqrt{2})R45°$ pattern was observed [47]. This surface unit cell is assigned to a $p4gm$ plane group, where there is octahedral rotation compared to the bulk. A quantitative LEED I-V analysis shows the rotation angle is $8.5° \pm 2.5°$ [66].

Replacing the Sr atom with Ca changes the lattice distortion. Near the projected QCP at $x_c \sim 0.5$, the LEED pattern appears identical compared to Sr_2RuO_4. There is slight enhancement of the octahedral rotation with no obvious signature of the surface tilt at the temperatures measured (300 K and 80 K), although the error bar of the rotation angle is so large that the results are suggestive. Similar results are obtained for the $x = 0.4$ sample $Ca_{1.6}Sr_{0.4}RuO_4$, where the high temperature still shows tetragonal structure with rotation only. At $T \sim 120K$ weak diffusive scattering emerges but there is no clear sign for tilt even at 80 K.

When $x < 0.3$ the tilt appears at low temperature, indicated by the emergence of the $(\pm 3,0)$ beams of the broken glideline. For $x = 0.3$ the surface structural transition happens at $\sim$240 K, about 50 K higher than the bulk transition temperature. For lower x this transition temperature increases that there is tilt on the surface even at room temperature. From this trend the transition temperature of $x = 0.4$ is estimated to be between 60 to 75 K.

29
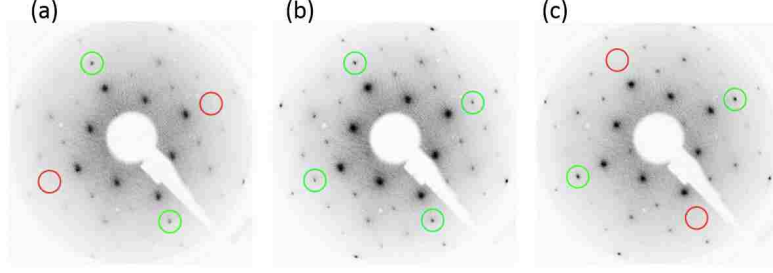
FIGURE 1.24: Tilt domains on the surface of $Ca_{1.9}Sr_{0.1}RuO_4$. Figure is adapted from [11].

The size of the tilt domains can also be estimated accordingly. Shown in Fig. 1.24 are three LEED patterns taken at the same temperature of the same surface. The only difference is that Fig. 1.24(b) is after a sample translation of $\sim$1mm from (a), and (c) is another $\sim$1mm from (b). Therefore Fig. 1.24(b) can be viewed as a superposition of the two patterns from (a) and (c), which are two domains oriented 90° with respect to each other.

Finally the surface phase diagram is concluded from these results, shown in Fig. 1.25. *p4gm* is the surface plane group with rotation only. *pm* is the surface plane group with both rotaion and tilt, but there are two domains 90° oriented so the pattern shows an additional mirror symmetry. *pg* is the surface plane group with both rotaion and tilt, and there is only one single domain.

1.6.2 Pure Electronic Mott Transition: $Ca_{1.9}Sr_{0.1}RuO_4$

The bulk phase diagram has been introduced in Fig. 1.5. For $Ca_{1.9}Sr_{0.1}RuO_4$ bulk there is a first-order Mott MIT at 154 K, while for its surface this transition happens at 130 K, shown in Fig. 1.26. Figure 1.26(a) shows the measurement of the bulk resistivity and the surface energy gap, the sudden jump of the resistivity and the opening of the gap indicate the occurrence of the phase transition. Figure 1.26(b) shows the Drude weight and phonon energy and intensity measured by HREELS, which are surface measurements. At the transition there is a sudden drop of the Drude weight accompanied by an energy shift, an abrupt linewidth
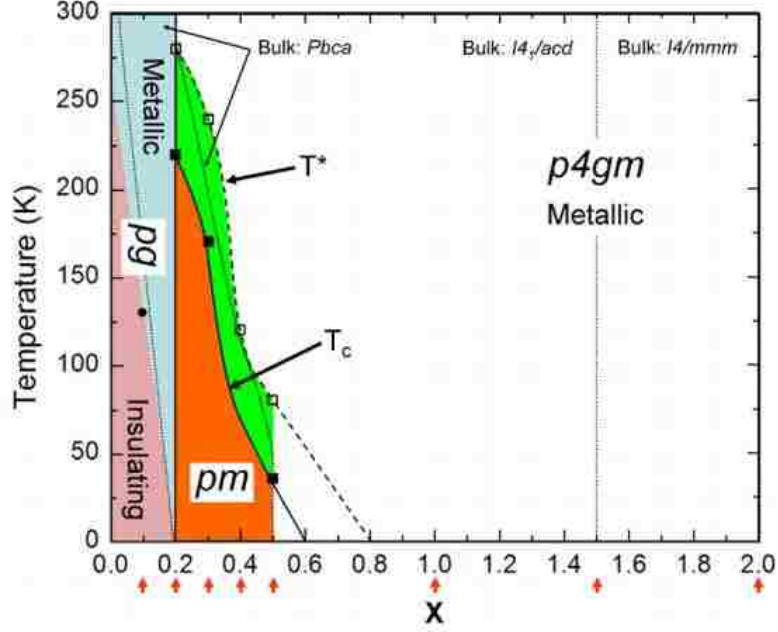
FIGURE 1.25: Surface phase diagram for $Ca_{2-x}Sr_xRuO_4$. Figure is adapted from [12].

reduction and a rapid intensity increase of the surface phonon. They are hallmarks of a surface Mott MIT.

Meanwhile the surface structure is characterized by LEED I-V calculation, where the pattern shows one single glideline at all temperatures, indicating the bulk-terminated orthorhombic structure. Detailed analysis shows no obvious change in the lattice distortion (octahedral rotation and tilt) across the MIT (see Table 1 of [67]), except for a very gradual thermal relaxation. Combining with DFT calculation show that there is a large inward motion of the Ca/Sr atom on the surface, which is responsible for the locking of the lattice distortion, impeding the structural transition across the MIT (see Fig. 4 of [67]). All the above evidence demonstrate that the Mott MIT transition on the surface of $Ca_{1.9}Sr_{0.1}RuO_4$ is pure electronic. This also explains the lower transition temperature on the surface because it has no assistance from the structure transition like the bulk does.

31
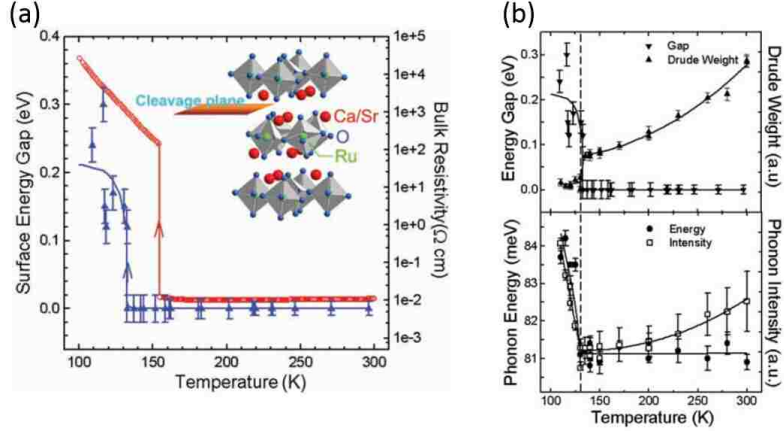
FIGURE 1.26: Surfce Mott MIT in $Ca_{1.9}Sr_{0.1}RuO_4$. (a) Temperature dependence of bulk resistivity (red) and surface energy gap measured by scanning tunneling spectroscopy (blue). (b) Temperature dependence of the Drude weight and phonon energy and intensity measured by HREELS. Figure is adapted from [67].

1.7 Focus of this Thesis

I have explored two different layered systems: one is the Fe-based superconducting compounds $Ba(Fe_{1-x}Co_x)_2As_2$; the other one is the Mn doped $Sr_3(Ru_{1-x}Mn_x)_2O_7$. In the bulk they both show rich phase diagrams with many low-lying states competing to be the ground state [27, 68]. More importantly, both of them have been proven to be extremely sensitive to the disturbance of external parameters, offering the perfect opportunities to study the coupling between charge (orbital), spin, and lattice under the broken symmetry at the surface.

1.7.1 Fe-based Superconducting Compounds $Ba(Fe_{1-x}Co_x)_2As_2$

There is one general conclusion from our studies of systems with coupled magnetic/structural transition. *The surface enhances the spin-charge-lattice coupling* [69]. For the surface of parent $BaFe_2As_2$ compound, scanning tunneling microscopy (STM) has observed surface-pinned antiphase domain walls [70], as shown in Figure 1.27(a). Topography shows each domain there is visible and invisible atom site, forming an orthorhombic-(1×1) unit cell. When crossing domain wall, visible switch to invisible, thus a π phase shifted at this structural anti-phase domain wall.

32
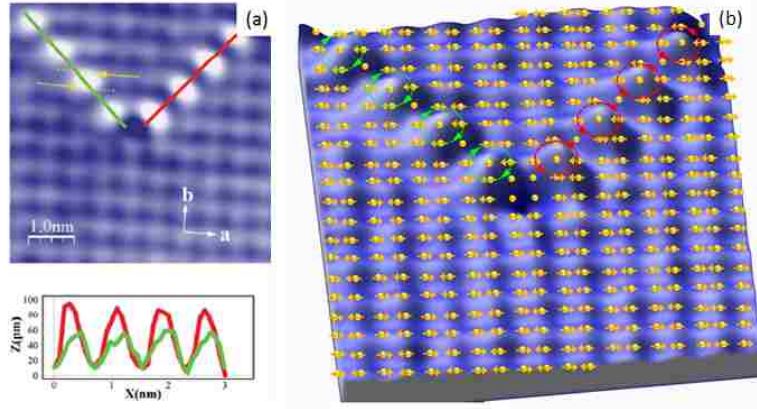
FIGURE 1.27: (a) 5.6 nm 5.6 nm low-bias constant-current STM topographies (Vbias = 23 mV, Itip = 200 pA) showing boundary structures at 80 K. The arrows with dashed lines indicate the half unit cell shift in the a and b directions, respectively. (b) Schematic of anti-phase spin domain coupled to the structural anti-phase domain. Figure is adapted from [70].

The interesting phenomenon is that there is no mirror symmetry on the domain walls at $45°$ and $135°$ direction, *i.e.* the intensity and shape of the bright spots along domain walls are different. Such lack of mirror symmetry was explained by an anti-phase spin domain coupled to this structural anti-phase domain, see Figure 1.27(b). A spin anti-phase domain lowers the symmetry, thus it gives a right- and left- chirality at $45°$ and $135°$ domain wall, respectively. The strong spin-lattice coupling at the surface results in the coexistence of structure and spin antiphase domain boundaries with a lower-than-bulk C_2 symmetry [70].

1.7.2 Mn-doped Double-layered $Sr_3(Ru_{1-x}Mn_x)_2O_7$

Shown in Fig. 1.28(a) is the tetragonal unit cell of the $n = 2$ RP family, while for $Sr_3Ru_2O_7$ there is octahedral rotation along the c-axis with opposite directions, leaving the stacking looks like Fig. 1.28(b). The unit cell with rotation is orthorhombic symmetry with a two-fold rotation axis, lattice parameters $a = b \neq c$ and $\alpha = \beta = \gamma = 90°$ [71]. There are two space groups proposed for such sturcture *Pban* [71] and *Bbcb* [72]. The difference between these two space groups can be described by stacking errors. In *Bbcb* the double layered octahedra stacking along
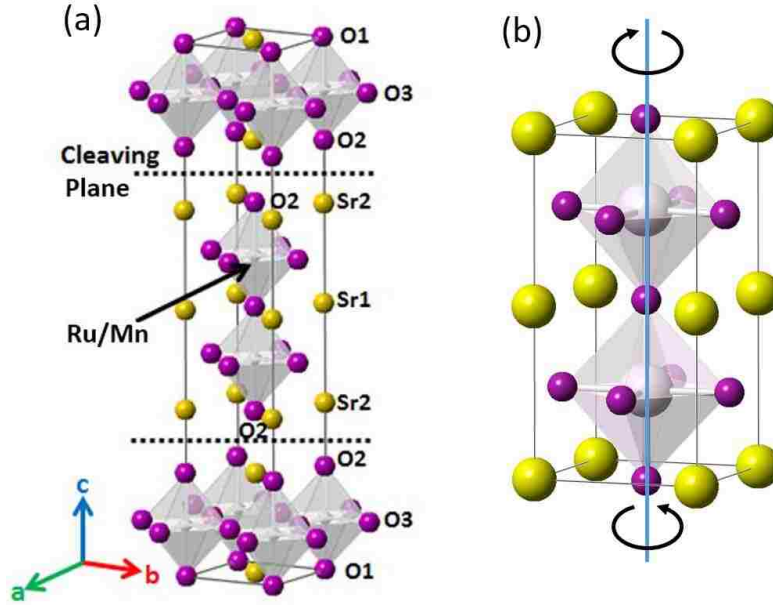
FIGURE 1.28: (a) Tetragonal (tet) unit-cell structure of $Sr_3Ru_2O_7$. The Ru atoms are located in the center of each octahedron. The cleaving plane is indicated by the dashed line, which results in a SrO surface layer. (b) Bulk structure of the double layered ocatahedra. The top and bottom octahedra are rotating in opposite directions.

the same direction (diagonal in tetragonal unit cell and x-axis in orthorhombic unit cell). In Pban the stacking errors happen so that the stacking changes to an perpendicular direction after certain stacking sequence. If there are similar amount of the two stacking directions, the experiment cannot differentiate them rather that the unit cell contains both stacking directions. Therefore the unit cell of *Pban* is twice the size of *Bbcb*.

The double layered $Sr_3Ru_2O_7$ generates great interest because of its quantum critical point (QCP) behavior under the magnetic field near zero temperature [73, 74, 20]. The classical definition of a phase transition is *the transformation of a thermodynamic system from one phase or state of matter to another one.* In Ehrenfests classification the first and second order phase transition is determined by the lowest derivative of the free energy that is discontinuous at the transition. In modern classification it is determined by the change in entropy at the transition:

discontinuous (1st order) and continuous (2nd order) phase transition. In comparison, the so-called quantum phase transition is a second order phase transition happens at absolute zero temperature, driven by quantum fluctuations demanded by Heisenbergs uncertainty principle, instead of thermal fluctuation, and tuned by external non-thermal external physical parameters such as pressure, magnetic field, and doping [75, 13, 76, 77]. The point that the quantum phase transition happens is named QCP. Schematic illustration of such a phase diagram is shown in Fig. 1.29.
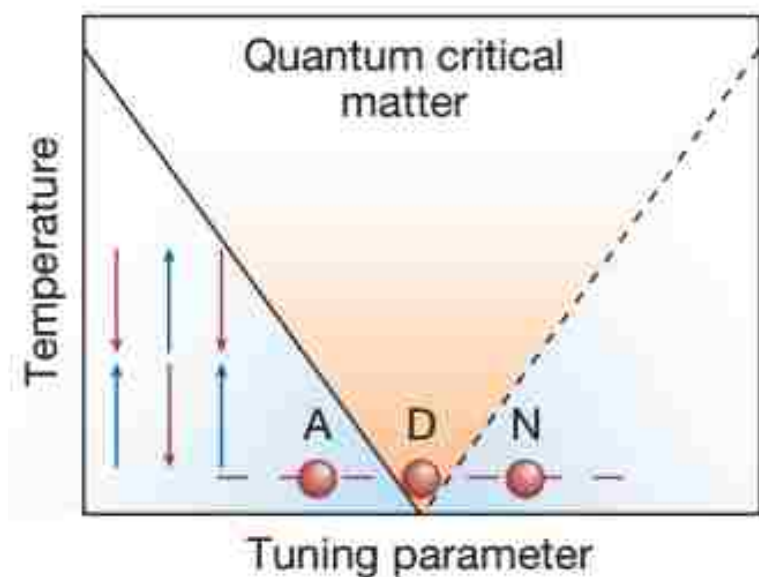
FIGURE 1.29: Phase diagram near a quantum critical point. Figure is adapted from [13].

The way that experimental physicists probe the properties is to look at the scaling behavior near the QCP. The scaling behavior can be understood by the studying the dependence of one physical property on another external parameter. For example the temperature dependence of resistivity ofter deviates from the T^2 behavior from the Fermi liquid theory, and exhibits the linear temperature dependence near QCP (YbRh$_2$Si$_2$ [76]). Other properties such as specific heat, magnetization, and

magnetic susceptibility also have quantum critical scaling behavior on parameters like magnetic field and pressure, derived by Hertz and Millis [78, 79].

Under this frame the behaviors of $Sr_3Ru_2O_7$ can be understood correspondingly. The well known one is the metamagnetic transition tuned by the magnetic field strength, where magnetization jumps when a magnetic field is applied within the directions of the layers. The magnetic field angle serves as the "tuning parameter", where when it is parallel to the c-axis, the critical point of the metamagnetism is tuned to zero at ~ 8 teslas [74]. With better sample quality there is unusual resistivity behavior exposed near the metamagnetic transition [80]. Also there is "saturation" of resistivity with magnetic field which is independent of the temperature under 1.1 K [81].
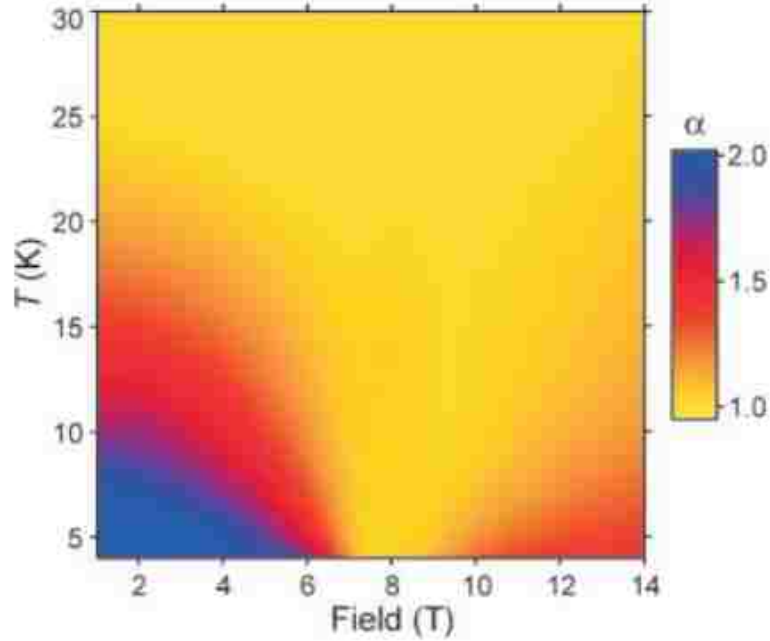
FIGURE 1.30: The resistivity behavior near the metamagnetic transition. The resistivity is derived in the formation $\rho = \rho_{res} + AT^\alpha$. Figure is adapted from [20].

It is generally agreed that the ground state of $Sr_3Ru_2O_7$ is strongly enhanced paramagnetic metal on the verge of ferromagnetism, where the FM order emerges

with the application of pressure [21, 72]. Shown in Fig. 1.31, the magnetization is greatly enhanced under pressure at low temperature, indicating its ground state has FM instability [21]. In constrast, with 16%Mn doping on the Ru site there is E-type AFM studied by neutron [82]. This AFM has zigzag chains along the plain, while the magnetic moment are parallel along the c-axis within a double octahedra unit cell. This means the there are competing phases beyond the ground state, which can be tuned by doping.
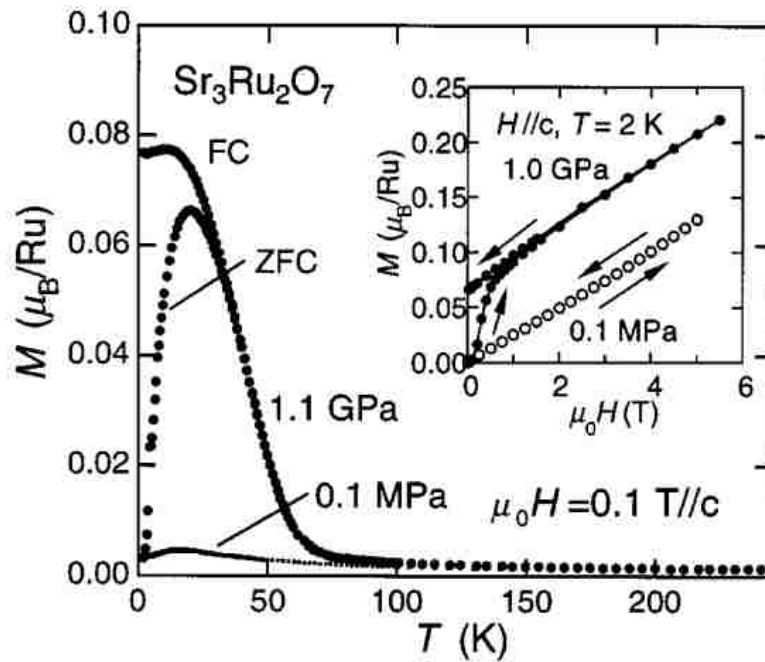
FIGURE 1.31: The pressure dependence of magnetization for field parallel to c-axis. The FM order is obvious with the large difference between the field cooling (FC) and zero field cooling (ZFC) at low temperature. Inset is the field dependence of magnetization under different pressures. Figure is adapted from [21].

The magnetic properties of Ca doped $(Sr_{1-x}Ca_x)_3Ru_2O_7$ was first investigated [83]. Shown in Fig. 1.32(a), at high temperature the material shows PM behavior. When Ca is doped into the system, the transition temperature of the metamagnetic state is yield to zero. However there is never long-range FM ordering, although there is considerably strong FM correlations. Instead it freezes into a cluster-spin

glass at low temperatures. With even more Ca the system is AFM ground state with a surprisingly large Wilson ratio R_W.

Shown in Fig. 1.32(b) is its electronic phase diagram which is intimated related to the magnetic one [84]. Starting with the metallic Fermi-liquid state of $Sr_3Ru_2O_7$, the system is turning more insulating with more Ca doping. Within the spin glass regime, it could be either metallic or weakly localized state. In contrast, within the AFM regime at low temperature, it is the AFM Anderson localized state. Again at high temperature, the system is metallic.

The magnetic properties are strongly coupled with the structure, shown in Fig. 1.32(c) [85]. The $Bb2_1m$ phase is associated with both octahedral rotation and tilt. It can be seen here when tilt emerges, the Bohr magneton, saturated moment, and the Curie-Weiss temperature all change abruptly.

The bulk phase diagram of $Sr_3(Ru_{1-x}Mn_x)_2O_7$ has been shown in Fig. 4.1. The MIT due to Mn doping was originally discovered by Mathieu *et. al.* [22], where there is a resistivity increase at low temperature starting from $x = 0.05$, along with the reduce of spectra weight measured by optical conductivity.

Detailed measurements show that this transition is coupled with the octahedral rotation, where T_{MIT} increases with less rotation. Meanwhile the short range AFM correlation develops into long range AFM ordering with more Mn, and finally reduces to short range magnetic correlation when $x > 0.2$. Beyond $x = 0.33$, the system is insulating even at room temperature.

Preliminary surface measurements have been done using scanning tunneling microscope (STM) and low energy electron diffraction (LEED). shown in Fig. 1.33 is the comparison of Sr_2RuO_4 and $Sr_3Ru_2O_7$ [47, 86, 87]. In Fig. 1.33(b) there are two kinds of hollow sites presented by arrows, but the two sites in (a) are similar, This indicates the STM image of $Sr_3Ru_2O_7$ has C_{2v} symmetry, lower than the Sr_2RuO_4
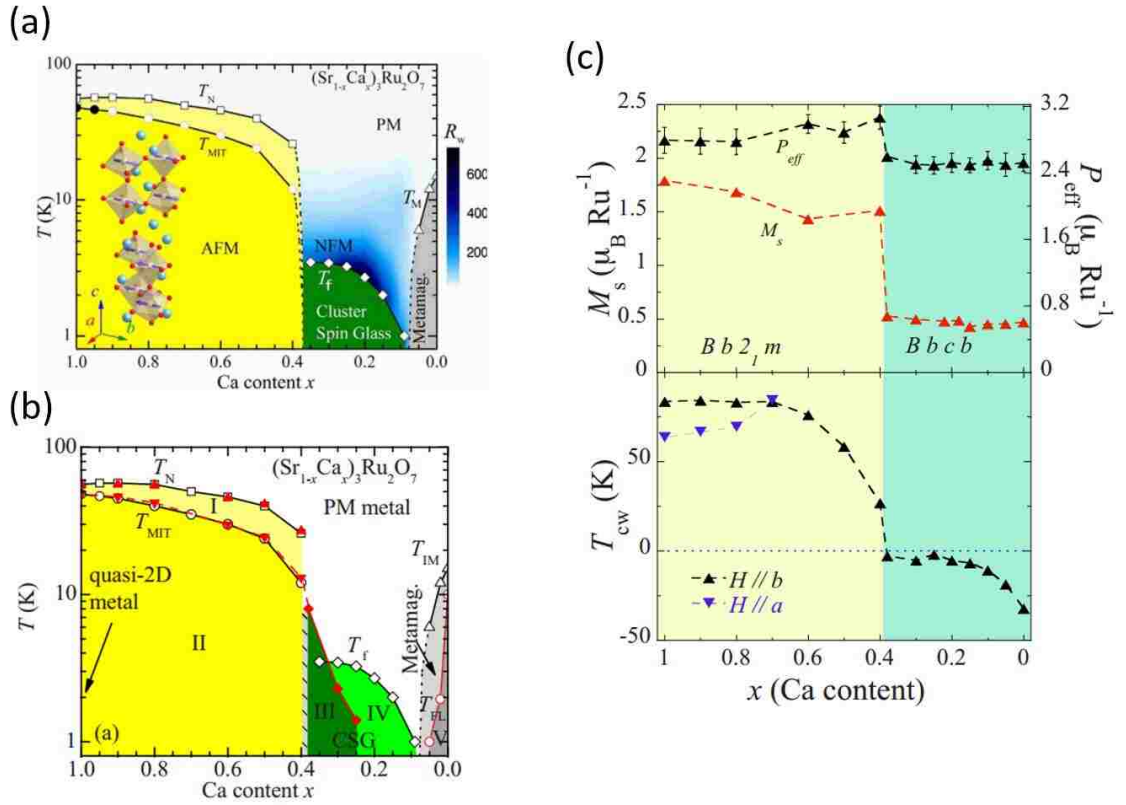
FIGURE 1.32: Phase diagrams of $Sr_{1-x}Ca_x)_3Ru_2O_7$. (a) Magnetic phase diagram. (b) Electronic Phase diagram. (b) Interaction between the magnetism and structure. Figures are adapted from [83, 84, 85].

which is C_{4v}. In Fig. 1.33(d) the spots at the green circles are existing, indicating a broken glideline symmetry (The glideline symmetry will be introduced at 2.1.5), which is different than the LEED pattern for Sr_2RuO_4.
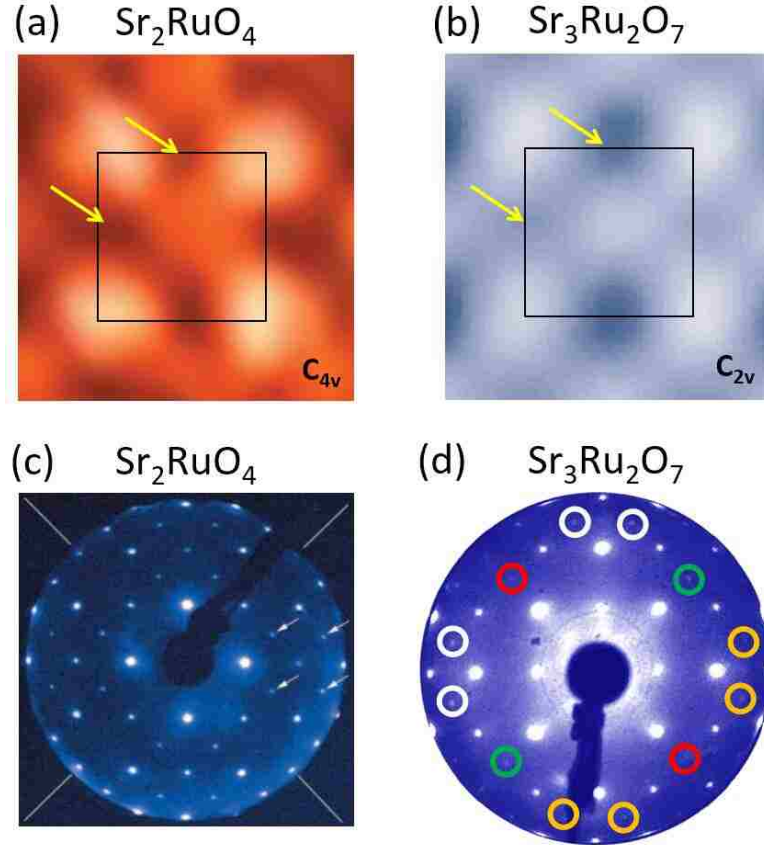
FIGURE 1.33: STM and LEED measurements of Sr_2RuO_4 and $Sr_3Ru_2O_7$. (a) STM image of Sr_2RuO_4 at 300 K. Figure is adapted from [47]. (b) STM image of $Sr_3Ru_2O_7$ at 0.56 K. Figure is adapted from [86]. (c) LEED pattern of Sr_2RuO_4 at 80 K. Figure is adapted from [47]. (d) LEED pattern of $Sr_3Ru_2O_7$ at 300 K. Figure is adapted from [87].

In this study, a complete picture of the $Sr_3(Ru_{1-x}Mn_x)_2O_7$ surface is explored, with the combination of surface techniques to probe the surface structure and metallicity. LEED I-V analysis is used to probe the surface rotational and tilt distortion. HREELS is used to explore the surface electron-phonon coupling for the surface metallicity as a function of Mn doping.

Chapter 2
Experimental Techniques

2.1 Low Energy Electron Diffraction (LEED)
2.1.1 Basic Principles

LEED is a surface sensitive technique for the determination of the surface structure of crystalline materials which uses a collimated beam of low energy electrons (20-600 eV) and observes diffracted electron pattern on a fluorescent screen, sketched in Figure 2.1. LEED can be used in two ways: qualitatively the surface symmetry information can be obtained from the diffraction pattern. Quantitatively the structure information can be obtained through calculation of the intensity-voltage (I-V) curves, which collects the intensities of diffracted spots as a function of incident electron beam energy.
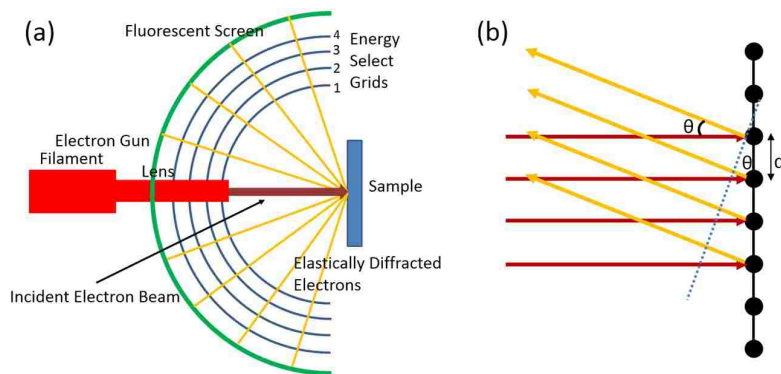
FIGURE 2.1: (a) Schematic of the LEED. The electron beam is elastically reflected by the sample surface and constructing diffractions are shown on the fluorescent screen as spots. (b) Diffraction condition for the 2D surface lattice.

The reason of using such a low energy electron beam is that its wavelength is comparable or shorter than the lattice constant but with a penetration depth in the range of several Å. From de Broglie relation, wavelength of an electron is related

to its momentum in a similar way as for a photon:

$$\lambda = h/p = h/mv = h/\sqrt{2mE}$$

where λ is the electrons wavelength which has a momentum p with mass m, velocity v, and energy E. h is Plancks constant. From this equation, for an electron with kinetic energy of 150.4eV, its wavelength is 1 Å. That is:

$$\lambda_e[\text{Å}] = \sqrt{150.4/E[eV]}$$

In comparison, if a photon has the same wavelength, its energy will be:

$$E = \frac{hc}{\lambda}$$

With similar calculation, this relation becomes:

$$E[eV] \approx \frac{1.24}{\lambda[\mu m]} = \frac{12400}{\lambda[\text{Å}]}$$

for the same 1 Å wavelength a photon needs to be 12400 eV, which is in the range of X-ray.

Another comparison is neutron scattering, where 1 Å wavelength corresponds to 3956 m/s neutron speed or 81.807 meV in energy, in the range of thermal neutrons.

The diffraction condition for LEED is sketched in Figure 2.1(b). Based on Braggs law, constructive diffraction happens when the pathlength difference satisfies $d\sin\theta = n\lambda$, where n is an integer. This relation shows three features: (1) At the same wavelength (electron energy) for the same n value (order of diffraction), $\sin\theta$ is proportional to $1/d$, meaning the smaller the lattice constant, the larger the diffraction angle. (2) At different electron energy for the same sample, $\sin\theta$ is proportional to λ which is $\sim 1/\sqrt{E}$, meaning the smaller the electron beam energy, the larger the diffraction angle. (3) If only the first layer is considered, n could be

either positive or negative, and the diffraction is symmetric. Therefore the diffraction pattern is always centrosymmetric. This is known as Friedel's law states that "a twin operation (aka Operation de maclage) is equivalent to an inversion centre and the intensities from the individuals are equivalent" [88]. Such rule widely holds in X-ray diffraction unless anomalous scattering happens [89]. However in LEED, the electron beam not only probes the top layer, but also several layers below, Friedels law breaks down resulting a non-centrosymmetric diffraction pattern.

2.1.2 Surface Sensitivity

LEED is a highly surface sensitive technique which only probes ~ 10 Å of the sample's top surface layer [90]. It uses elastically scattered electrons without any energy loss for the diffraction. The inelastic electrons are filtered out by the grids in Figure 2.1(a) using a high pass filter (retarding field analyzer or suppressor). The 4 grids work in a way that grid 1 and 4 are grounded, with one floating ground (grid 1) and one real ground (grid 4). The other two (grid 2 and 3) are biased by an energy slightly smaller than the beam energy such that electrons with energy loss cannot pass through.

The energy distribution from electron scattering process is presented in Figure 2.2[14]. Majority of the scattered electrons having very small energy are secondary electrons (SE). They could be excited electrons either from conduction/valence bands or inner shells. When they are moving towards the surface after excitation, they undergo a series of collisions with other electrons thus losing their energy. Other scattered electrons are named back scattered electrons (BSE), and they could be either elastic or inelastic. The inelastic BSE normally include Auger electrons (AE) and electrons with energy loss due to plasmons, intra-band transitions, and phonons. Only a small portion are back scattered without losing any energy, which is indicated by E_0 in Figure 2.2[14].
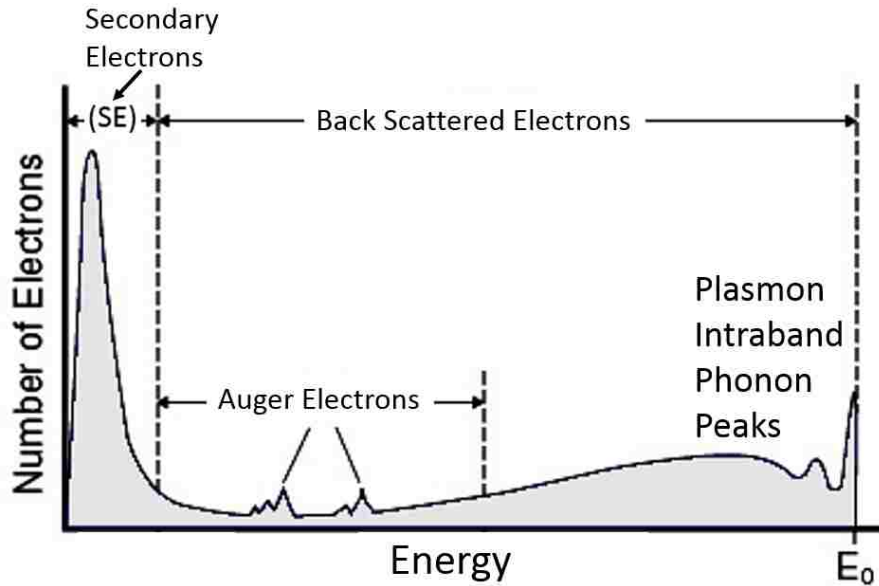
FIGURE 2.2: Energy spectrum of scattered electrons from a solid. Figure is adapted from [14].

The consequence of such strong energy loss of the electrons is that the mean free path of the electrons is short, presented in Figure 2.3[15]. From this figure the mean free path of the electrons that LEED uses is about 5~10 Å, corresponding to only a few atomic layers in a solid. The contributions to the diffraction from deeper atoms are exponentially reduced.
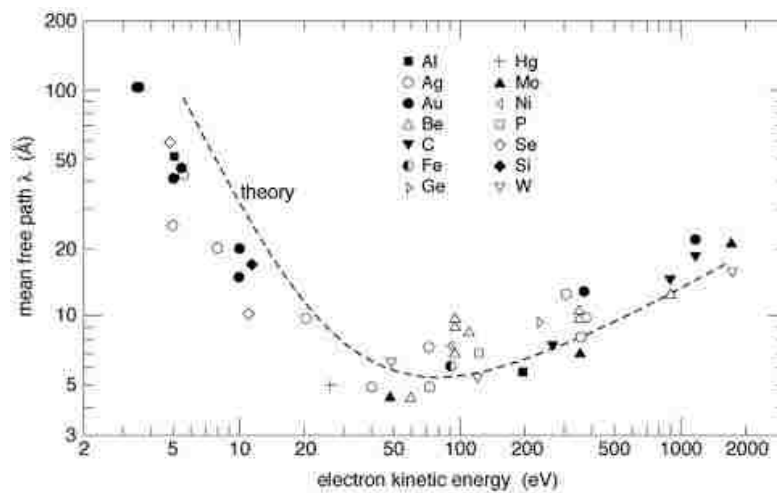
FIGURE 2.3: "Universal curve" of electron inelastic mean free path λ (IMFP) versus kinetic energy (KE). Figure is adapted from [15]

Another important feature of LEED is its coherence length, which is about 100~200 Å. In comparison, the coherence length for neutron scattering is ~200 Å and for X-ray scattering is to the order of ~10^4 Å. The coherence length defines the diameter of area that is coherently scattered. If the two scattered places are separated by a distance smaller than the coherence length, their scattering amplitude will be added together. If the two scattered places are separated by a distance larger than the coherence length, their scattering intensity will be added together. It is determined by the energy resolution of the electron beam ΔE. The smaller ΔE gives more monochromatic electron beam, thus a larger coherence length. If the sample has a domain larger than this coherence length, it will result in a sharp LEED pattern. However in reality the observation of a LEED pattern does not mean the whole surface is ordered. This is because LEED pattern is a superposition of patterns from different domains all over the surface area under the beam. The analysis of the LEED pattern will be discussed below.

2.1.3   2D Reciprocal Space

The Laue's condition of diffraction requires that the change in wave vector between the incoming and outgoing beams is equal to a vector of the reciprocal space[91]. It is an equivalent condition compared to the Braggs condition mentioned before. Based on this idea, one can build an Ewald sphere in the three dimensional reciprocal space. The spheres radius is equal to the wave vector of the incident beam. Under such scheme, whenever the surface of the Ewald sphere cuts through two reciprocal space, there exists a constructive interference with direction indicated by the two wave vectors, shown in Figure 2.4.

For the 2D surface lattice, there is only two real space lattice vectors **a** and **b**. When constructing the 2D reciprocal space, the process is simplified with the **c**
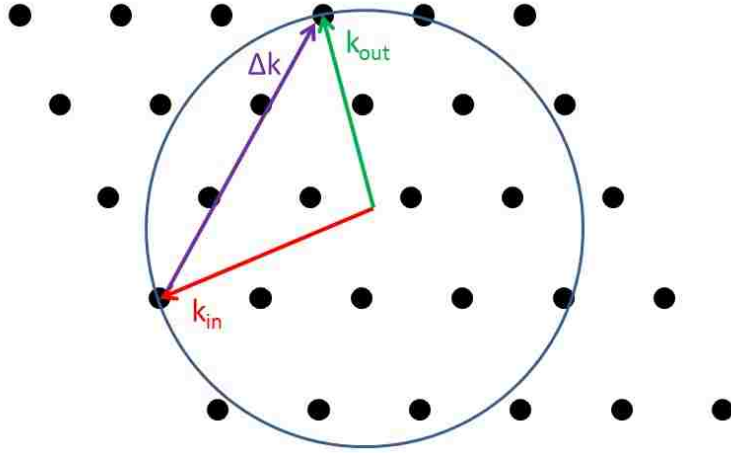
FIGURE 2.4: Ewald sphere construction in reciprocal space.

vector is replaced by a unit vector $\hat{\mathbf{n}}$ always pointing along the normal direction. That is

$$\mathbf{a}^* = \frac{2\pi\mathbf{b}\times\hat{\mathbf{n}}}{|\mathbf{a}\times\mathbf{b}|} \text{ and } \mathbf{b}^* = \frac{2\pi\hat{\mathbf{n}}\times\mathbf{a}}{|\mathbf{a}\times\mathbf{b}|}$$

With such definition the Ewald sphere construction in LEED is applied by considering the 2D reciprocal lattice with rods extending perpendicular from each lattice point, shown in Figure 2.5. Note that the incident electron beam is always perpendicular to the surface, and the directions of which the diffraction spots form on the fluorescent screen is also shown.

2.1.4 Pattern Analysis

The simplest LEED pattern is the (1×1) pattern which represents the 2D reciprocal lattice of the bulk-truncated surface, shown in Figure 2.6(a)&(b). For example the grey grids in Figure 2.6(a) indicate the bulk unit cell, and the red dots are the surface lattice with bold red lines indicating the surface lattice vectors. The LEED pattern from such a surface is simulated, shown in Figure 2.6(b). In this simulated pattern, the circles are diffraction pattern from the bulk unit cell, and the dots from surface unit cell. They locate at the same positions, indicating the surface and the bulk have the same unit cell. Such a pattern is named a (1×1) pattern.
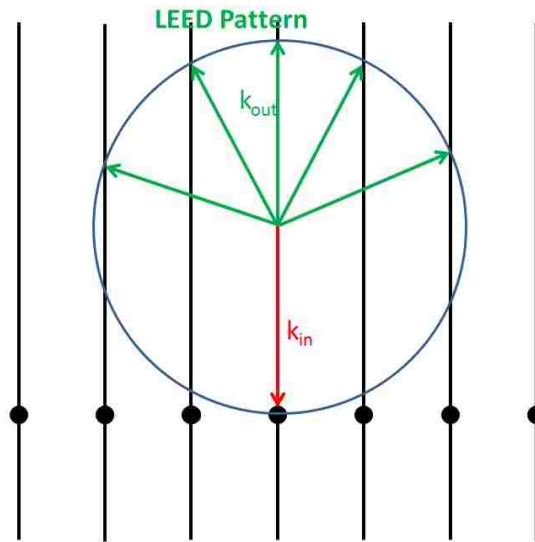
FIGURE 2.5: Ewald sphere construction for LEED with normal incidence of the primary electron beam.
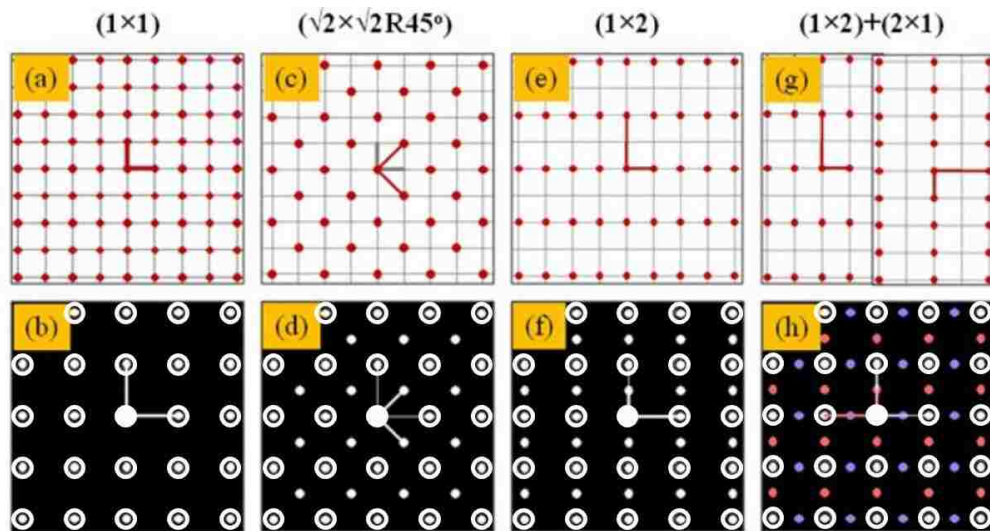
FIGURE 2.6: The corresponding LEED pattern of bulk truncated (1×1) square lattice phase and several surface reconstruction phases including (1×1), $(\sqrt{2} \times \sqrt{2})R45°$, (1×2) and its twin domains. Figure is adapted from [16].

In many situations the surface unit cell is larger than the bulk. For instance in Figure 2.6(c) half of the atoms are missing at the surface, resulting in a larger surface unit cell indicated by the red lines. In the current situation, the atoms arrange in such a diagonal way compared to the bulk lattice, such that the surface lattice parameter is $\sqrt{2}$ times and also 45° rotated compared to the bulk. This behavior is surface reconstruction or super lattice. In this specific surface order, this is named $(\sqrt{2} \times \sqrt{2})R45°$ or $c(2 \times 2)$ reconstruction.

The $(\sqrt{2} \times \sqrt{2})R45°$ LEED pattern is shown in Figure 2.6(d) with the real space lattice in (c). The (1×1) pattern from the bulk indicated by the circles has the larger size than the $(\sqrt{2} \times \sqrt{2})R45°$ from the surface unit cell indicated by the dots. Normally these circles are named integer spots while the dots are fractional spots. This is because the LEED pattern represents the reciprocal space (or k-space), and the larger in real space, the smaller in k-space. Meanwhile they keep the same length scale and rotational degrees with respect to each other.

Another example of surface reconstruction is the (1×2) reconstruction, shown in Figure 2.6(e). In this case, the lattice vector doubles its size along one direction while remains unchanged along the other direction. The original 4-fold unit cell symmetry is now 2-fold. Its LEED pattern is shown in Figure 2.6(f), which retains the same 2-fold symmetry as in real space but rotated 90°.

However in real experiment one often sees a LEED pattern with 4-fold symmetry instead. This is because there always domains on a sample surface. Shown in Figure 2.6(g), the two domains can have exactly the same (1×2) reconstruction (twin domains) but perpendicular to each other. The resulting LEED pattern will be the superposition constructed from two perpendicular patterns, which ends up with a 4-fold symmetry instead of 2-fold, as presented in Figure 2.6(h). Note that the

(1×2) reconstruction with domains is different from a (2×2), because of the missing spots which supposed to locate at the $(\sqrt{2} \times \sqrt{2})R45°$ fractional sites.

Except for the tetragonal and orthorhombic surface unit cell, another often observed pattern is the trigonal cell, such as the (111) surface of the face-centered lattice. A good example is the (001) surface of the IrTe$_2$ material, shown in Fig. 2.7.
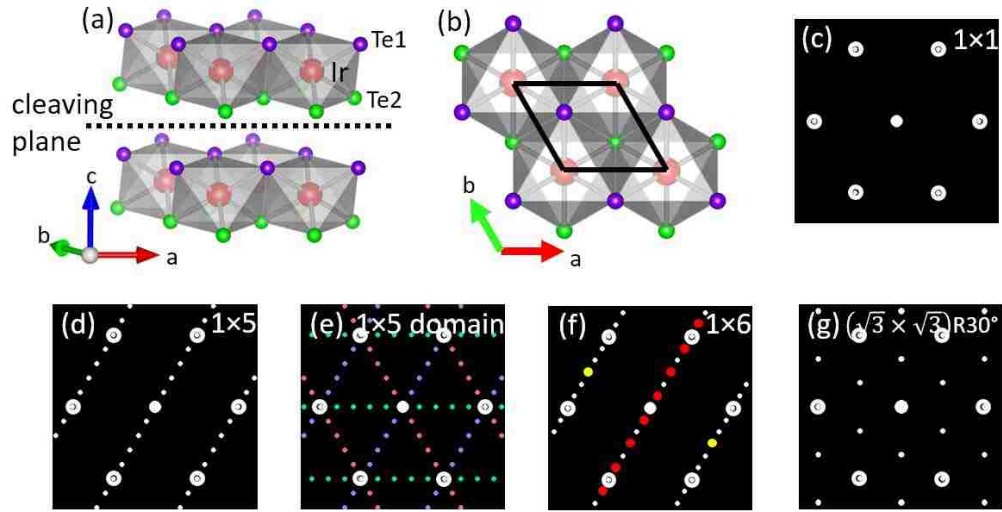
FIGURE 2.7: Crystal structure and schematic LEED pattern for a surface with trigonal symmetry. (a) Structure of IrTe$_2$ lattice. (b) Bulk truncated surface. (c) Schematic 1×1 LEED pattern from the surface without any reconstruction. (d) Schematic LEED pattern from 1×5 surface reconstruction. (e) Same 1×5 LEED pattern but with three domains 120° with respect to each other. (f) Schematic LEED pattern from 1×6 surface reconstruction. (g) Schematic LEED pattern from $(\sqrt{3} \times \sqrt{3})R30°$ surface reconstruction.

Fig. 2.7(a) is the structure of IrTe$_2$ lattice. The two Te atoms labeled in purple and green are equivalent in the bulk. Samples are cleaved between the two Te layers. Figure 2.7 (b) is the bulk truncated surface, which will result in a 1×1 LEED pattern shown in (c). In principle the surface is three-fold so that the three spots of the equilateral triangle actually have larger intensity than the other three of the triangle in opposite direction. This could be better resolved from their LEED I-V information.

There is a 1×5 structural transition due to the Ir-Ir dimerization which will result in a surface like Fig. 2.7(d) [92]. Because of the unit cell's three-fold symmetry, there are often domains existing on the surface which are 120° with respect to each other. The corresponding LEED pattern is a superposition of three patterns with the same angle difference, shown in Fig. 2.7(e). STM measurements have observed the ground state of the surface is 1×6, and the LEED pattern corresponds to the Fourier transform of the image is shown in Fig. 2.7(f) [93].

Fig. 2.7(g) is a schematic LEED pattern of the $(\sqrt{3} \times \sqrt{3})R30°$ reconstruction, which happens a lot on the surface with trigonal symmetry, such as Si(111) [94]. Note that this structure has not been observed on IrTe$_2$, Fig. 2.7(g) is simply an illustration of the $(\sqrt{3} \times \sqrt{3})R30°$ pattern.

2.1.5 Structure Factor and Glide Plane Symmetry

The diffraction intensity for a 3D crystal can be obtained by calculating its structure factor. As introduced before, any constructive interference requires the wave vector change is equal to a reciprocal space vector $\mathbf{q} = h\mathbf{a}^* + k\mathbf{b}^* + l\mathbf{c}^*$. If the basis consists of N atoms, the structure factor can be written as

$$S(\mathbf{q}) = \sum_{i=1}^{N} f_i(\mathbf{q})e^{i(\mathbf{q} \cdot \mathbf{r_i})}$$

where $f_i(\mathbf{q})$ is a factor determined by the phase change in the scattering process of each atom, $\mathbf{r_i}$ is the position vector of each atom in the basis.

Now we consider a symmetry operation named glide plane symmetry, in 2D it is often named glide reflection. It is defined as a mirror reflection with respect to a plane, followed by a translation parallel to the plane by certain fraction of the lattice parameter. Figure 2.8(a) is an example of such symmetry with the glide plane indicated by the dashed line.
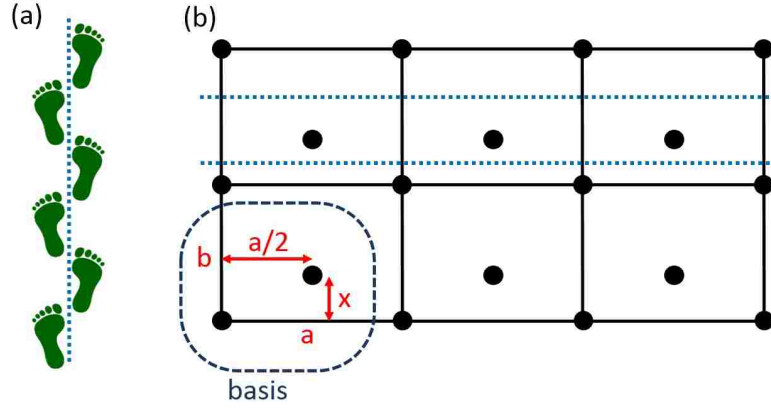
FIGURE 2.8: Glide plane symmetry. (a) An example of glide plane symmetry. (b) An orthorhombic crystal lattice with an atom locates at half way along one side and arbitrary location along the other. Two dashed lines indicate the glide plane. The dashed rounded rectangle indicates the basis.

When the surface has glide plane symmetry, in LEED pattern the odd-integer spots towards [10] and/or [01] directions will be missing depending on the direction. For example Figure 2.8(b) is a 2D crystal lattice with such symmetry. Starting from orthorhombic lattice made of rectangular unit cells, an extra atom is added at a position half way along one side and arbitrary location along the other as labeled. By simple geometrical consideration it can be shown that the two dashed lines are the glide planes. Now we can prove the above argument by calculating its structure factor.

First we need to pick up its basis and in this case it includes two atoms within the dashed rounded rectangle. The coordinates for these two atoms are (0,0) and $(1/2,x)$. Then note that the reciprocal space lattice vector has the property $\mathbf{a_i^*} \cdot \mathbf{a_j} = \delta_{ij}$. Assume these are identical atoms so $f_i(\mathbf{q}) = f$ is a constant. This yields

$$
\begin{aligned}
S(\mathbf{q}) = \sum_{i=1}^{N} f_i(\mathbf{q}) e^{i(\mathbf{q} \cdot \mathbf{r_i})} &= f \cdot \left(e^{i(\mathbf{q} \cdot 0)} + e^{i(\mathbf{q} \cdot (\mathbf{a}/2 + x \cdot \mathbf{b}))} \right) \\
&= f \cdot \left(1 + e^{i((h\mathbf{a}^* + k\mathbf{b}^*) \cdot (\mathbf{a}/2 + x \cdot \mathbf{b}))} \right) \\
&= f \cdot \left(1 + e^{2\pi i((h/2 + k \cdot x))} \right) \\
&= f \cdot \left(1 + e^{\pi i((h + 2k \cdot x))} \right)
\end{aligned}
$$

where S=0 when h is odd and k is 0.

One of the materials with this property is the Ruthenates where the RuO_6 octahedra can have rotational and tilt distortion. Figure 2.9 is a representative top view of the surface octahedra with three different structures. For single layer $Ca_{2-x}Sr_xRuO_4$, the non-doped compound Sr_2RuO_4 has no octahedra distortion in the bulk [95, 34]. Figure 2.9(a) is the bulk-truncated and Figure 2.9(b) is its LEED pattern. However a rotational distortion is actually seen on the surface [47] resulting in surface reconstruction, shown in Figure 2.9(c)&(d). One thing worth mentioning is that there are glide planes shown by the dashed lines. These cause the missing spots in the LEED pattern shown by the arrows. The two corresponding perpendicular lines are called glide lines. When the doping level $x¡0.2$, there is further tilt distortion on the surface, shown by different colors in Figure 2.9(e). In this case, two glide planes along the vertical direction are broken, resulting in missing of one glide line, shown in Figure 2.9(f).
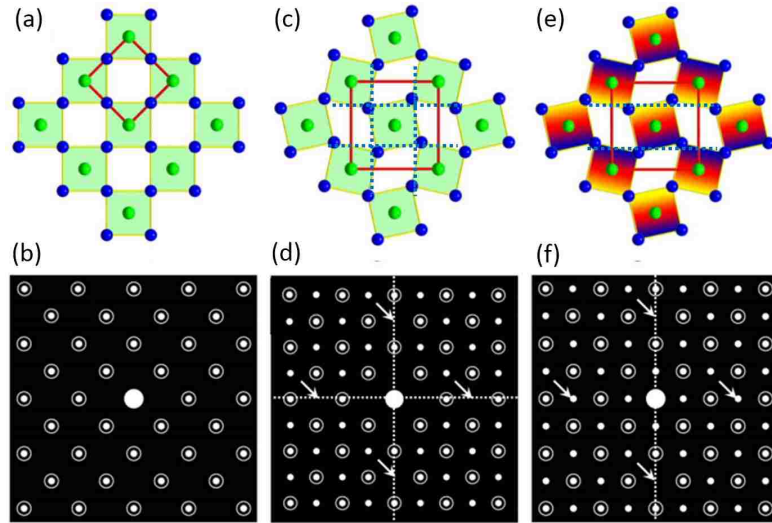
FIGURE 2.9: Top view of Ruthenates octahedra with different structural distortions and their corresponding simulated LEED patterns. Figure is adapted from [16]

2.1.6 LEED I-V Analysis

To obtain information about the structure within the unit cell such as the atomic positions, one needs to analyze the intensity-voltage (I-V) curve and perform corresponding calculations. Comprehensive understanding and detailed method of LEED I-V calculation has been described in several books [96, 97, 98]. When the electron beam is assumed to be scattered only once by the top surface atomic layer like in Fig. 2.10(a), the pattern can be well described by a simple kinematic theory. Under this approximation, the incident electron can be described by a plane wave with form $A_i = A_0 e^{-i\mathbf{k}_i \cdot \mathbf{r}}$. The scattered beam can be written in similar form with a phase shift from the scattering process

$$A_s = A_0 \sum_{j=0}^{\infty} R e^{-i\mathbf{k}_i \cdot 2\mathbf{d_j}} e^{-i\mathbf{k}_i \cdot \mathbf{r}} = A_0 \frac{i\sqrt{1-T^2}}{1 - e^{-i\mathbf{k}_i \cdot 2\mathbf{d_j}}} e^{-i\mathbf{k}_i \cdot \mathbf{r}} \tag{2.1}$$

where R and T are the reflection and transmission coefficients respectively. Here T is assumed to be real, which is valid when the scattering is weak enough. Thus R is pure imaginary. When $\mathbf{k}_i \cdot 2\mathbf{d_j} = 2n\pi$, the Bragg's condition satisfies. Then the denominator in Equation 2.1 becomes zero and the amplitude diverges. This is when the constructive diffraction happens. The I-V curves are delta functions for $T = 1$ shown in Fig. 2.10(b). When T is not 1 the peak intensity does not go to inifity.

The infinite peak intensity in 2.10(b) violates the current conservation. One solution is to consider the fact that the electron wavefunction is transmitted twice at each atom: one from the surface to the $j+1$ atom, and one from the reflected wave. This is considered to be a simple multiple scattering situation shown in Fig. 2.10(d). Taking this into account there is a modified term in the denominator as

$$A_s = A_0 \sum_{j=0}^{\infty} R T^{2j} e^{-i\mathbf{k}_i \cdot 2\mathbf{d_j}} e^{-i\mathbf{k}_i \cdot \mathbf{r}} = A_0 \frac{i\sqrt{1-T^2}}{1 - T^2 e^{-i\mathbf{k}_i \cdot 2\mathbf{d_j}}} e^{-i\mathbf{k}_i \cdot \mathbf{r}} \tag{2.2}$$
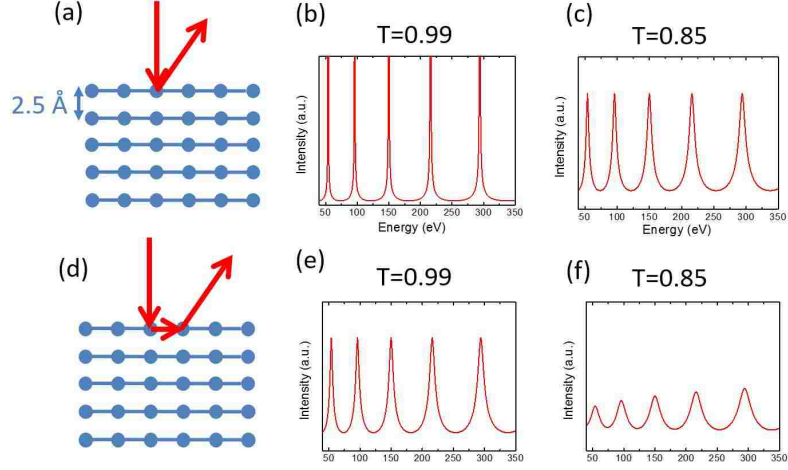
FIGURE 2.10: Simulated LEED I-V curves. The simulation uses lattice constant $d = 2.5\mathring{A}$, $T = 0.99$ for (b) and (c), and $T = 0.85$ for (e) and (f).

and the peak intensity is reduced as shown in Figure 2.10(e) and (f).

The electron also feels the crystal field around each atom. In a real material the extension of conduction electron wavefunctions beyond neighboring atoms will lead to non-zero charge density. The electron energy is shifted by this non-zero charge density. To describe this situation a so-called inner potential is added with the form $V_o = V_{or} + iV_{oi}$. The real part shifts the electron energy and the imaginary part broadens the peak linewidth. Thus the wave vector of the energy altered electron beam is

$$k = \sqrt{\frac{2m(E - V_o)}{\hbar^2}} = \frac{2\pi}{\sqrt{150[eV]}}\sqrt{E - V_{or} - iV_{oi}} \qquad (2.3)$$

Put Equation 2.3 into Equation 2.2, the modified I-V curves are presented in Fig. 2.11. The real part shifts the peak position by the same value, while the imaginary part increases the linewidth so that with higher V_{oi} the peak looks "shorter" and "fatter". For simple metals $V_{or} \sim 10$ eV and $V_{oi} \sim 4$ eV are good estimate. In real situations they should be calculated in an energy dependent manner because electrons with different energies (speed) "sees" the potential differently during
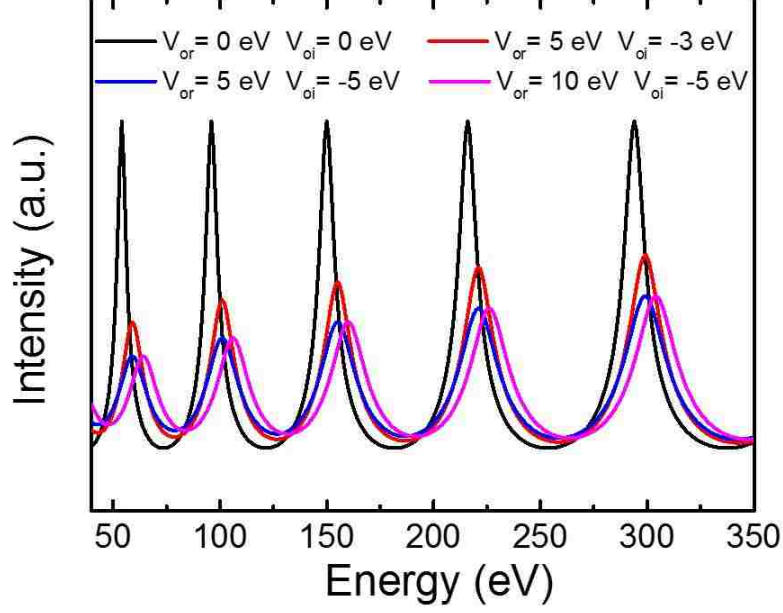
FIGURE 2.11: LEED IV simulation for different inner potentials.

the scattering process. In the end the real part of the inner potential takes a phenomenological form:

$$V_{or}(E) = \begin{cases} \text{const}, & \text{when } E < E_c \\ A_0 + \frac{A_1}{\sqrt{E+A_2}}, & \text{when } E > E_c \end{cases} \qquad (2.4)$$

The imaginary part of the inner potential can be estimated based on the "Universal Curve" of the electron mean free path in Fig. 2.3 [15]. A simplified phenomenological form is:

$$V_{oi} = C\left(\frac{E}{200/27.21 + V_{or}}\right)^{1/3} \qquad (2.5)$$

One difference between incident photons and electrons is that photons interact weakly with the crystal, where kinematic methods work very well, such as in X-ray scattering. The interaction between electrons and crystal is much stronger. As seen in Fig. 2.2, only a small amount are back scattered elastically. Electrons undergo multiple scattering, meaning they are scattered back and forth between layers.

This process is best understood through renormalized forward scattering (RFS) shown in Fig. 2.12. Vertical black lines represent layers of the crystal. T and R are transmitted and reflected beams, respectively.
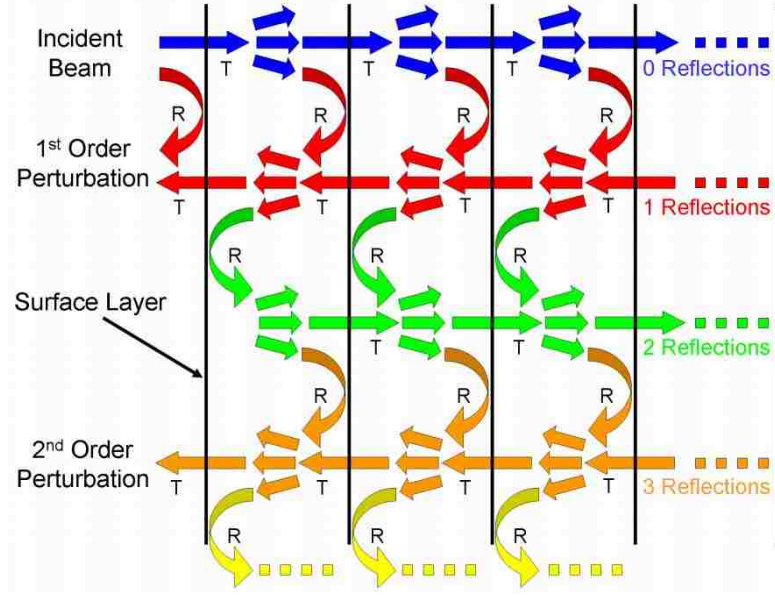
FIGURE 2.12: Renormalized forward scattering. Figure is adapted from [11].

The modification of the multiple scattering is presented in Fig. 2.13. This is simulated by adding an extra term on the denominator of Equation 2.2 simulating the higher order perturbation from the reflected beams. Although this cannot completely describe the multiple scattering, it shows some basic features such as the extra peaks shown by the red curve compared to the black curve in Fig. 2.13.

$$A_s = A_0 \frac{i\sqrt{1 - T^2}}{1 - T^2 e^{-i\mathbf{k}_i \cdot 2\mathbf{d_j}} - (T^2 - 1)T^2 e^{-i\mathbf{k}_i \cdot 4\mathbf{d_j}}} e^{-i\mathbf{k}_i \cdot \mathbf{r}}$$

In order to better describe the multiple scattering, one needs to perform calculation including the atomic phase shifts and the optical potential must be recalculated using atomic potential approximations such as muffin-tin (MT). The details of this method can be found elsewhere [11, 96, 97, 98].

Although the above figures describe a relationship between intensity and beam energy, it is not the real I-V curve. It is describing the intensity of a static spot on
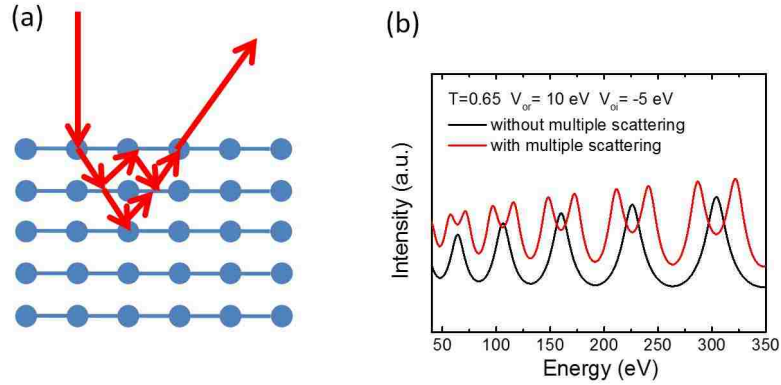
FIGURE 2.13: Sketch of the LEED I-V modified by multiple scattering.

LEED screen, rather than a diffraction spot. For example, in the simplest case of kinematic scattering of a single layer, there should always exists scattering spots because the Ewald sphere can always cut the grids. Then the corresponding I-V curve should be a straight line parallel to the x-axis, not Fig. 2.10(a). It is becase of the penetration of electrons into the first few layers, not only the first one, that the "straight line" becomes peaks. In this situation, Bragg rods in Fig. 2.5 are not infinite any more, and becomes intermittent rods. Imagine the extreme situation that the electrons penetrate deep into the bulk, just like X-ray scattering. Thus the rods become a line of spots and the sphere can only cut the spots at certain energies. In this case the I-V curve becomes an array of delta functions.

What will happen when the electrons only penetrate a few layers on the surface? Ref. [98] has discussed about such situation. Introduced here are some general results. First of all the diffraction condition still follows the Bragg's condition, which means the position of the peak energies are proportional to n^2 where n is the diffraction order in Bragg's condition equation (Fig. 2.10(b)). For the depth dependence of linewidth, we know that in two extreme situations: infinity linewidth for single layer and zero linewidth for infinite layers. This means the more layers involved in the diffraction process, the smaller the peak linewidth. This can be

estimated in analogy with optical interference calculations (single slit diffraction) [98]:

$$\Delta k = \Delta(\frac{2\pi}{\lambda}) \simeq \frac{\pi}{2Nd} \tag{2.6}$$

where d is the interlayer distance along the c-axis.

We know for a free electron $k \sim \sqrt{E}$, then the energy linewidth is

$$\Delta E \simeq \pi(2E)^{\frac{1}{2}}/(2Nd) \tag{2.7}$$

For 100 eV beam energy and 10 eV linewidth, the estimated penetration depth $Nd \sim 6\text{Å}$, which is ~ 4 atomic layers.

Note that LEED I-V calculation is a fitting process. There is no way to directly obtain the structure within the unit cell from the LEED pattern analysis. The first step in the procedure of LEED I-V analysis is to set up a model surface structure, which is chosen to be consistent with the symmetry of the LEED pattern. As a second step, calculations applying multiple-scattering theory produce theoretical I-V curves, which are compared to the experimental results. It usually requires a process of refinement: the model needs to have several structural and non-structural parameters systematically varied in order to minimize the differences between calculated and experimental spectra. Generally, the imaginary part of the optical-potential and the Debye temperature of the model surface are two non-structural parameters of the model until satisfactory agreement is obtained. So the surface structure is finally determined when the set of theoretical and experimental curves match. In LEED, the so-called reliability factor (R_P-factor) is used to quantitatively evaluate the goodness of fit between the theoretical and experimental I-V [99]. If $R_P=0$ there is perfect correlation between the theoretical and experimental I-V curves. $R_P>1$ means that theory and experiment are com-

pletely uncorrelated. The lower R_P factor acquired, the better is surface structural determination. Usually, it is confident if $R_P<0.3$.

The R_P factor is defined as following: For each curve (experimental and theory), a L function (differential of the logarithmic intensity curve) is generated as

$$L = \frac{1}{I(E)} \frac{dI(E)}{dE}$$

Then a Y function is generated to avoid the singularity when $I(E)$ is zero:

$$Y = \frac{L}{1 + V_{oi}^2 L^2}$$

The R_P factor between two curves is

$$R_P = \frac{\int (Y_{\exp} - Y_{\text{th}})^2 dE}{\int (Y_{\exp}^2 + Y_{th}^2) dE}$$

When there are several beams, the total R_P factor is estimated as

$$R_P^{Total} = \frac{\sum\limits_{i=1}^{N} (R_P)_i (\Delta E)_i}{\sum\limits_{i=1}^{N} (\Delta E)_i}$$

where ΔE is the energy range of each beam.

2.2 High Resolution Electron Energy Loss Spectroscopy (HREELS)

HREELS is a surface sensitive instrument which measures the energy loss of back scattered electron beam from the sample. The energy loss contains information of quasiparticle excitations such as: adsorbate vibrations, lattice vibrations (phonons), surface plasmons, and inter(intra)band electronic transitions.
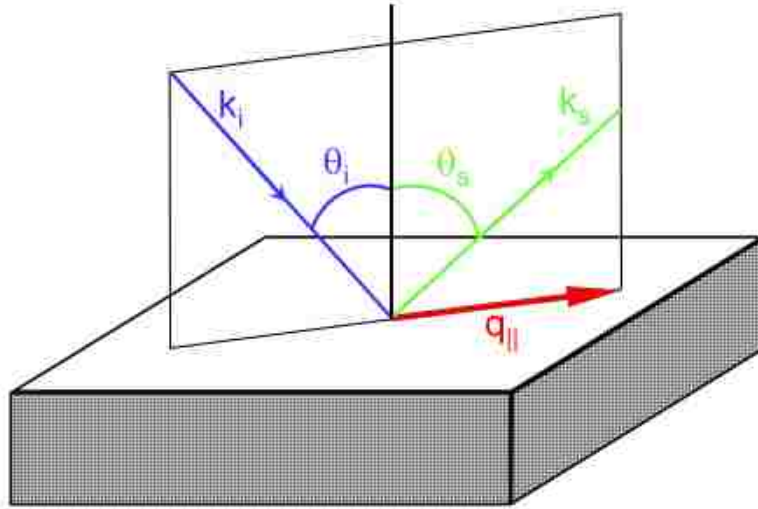
FIGURE 2.14: HREELS scattering geometry. Figure is adapted from [11].

HREELS applies simple conservation of energy and momentum to the electron beam. As shown in Figure 2.14, the incident electron beam has energy E_i with momentum $\mathbf{k_i}$, and the incident angle is θ_i. The corresponding scattered electron beam has the energy E_s, momentum $\mathbf{k_s}$ and scattering angle θ_s respectively. The conservation of energy has

$$E_s(\mathbf{k_s}) = E_i(\mathbf{k_i}) - \hbar\omega(\mathbf{q_{\|}})$$

where $\hbar\omega(\mathbf{q_{\|}})$ is the energy of the quasi particle excitation which has momentum transfer parallel to the surface $\mathbf{q_{\|}}$. Meanwhile from the conservation of momentum there is

$$\mathbf{k_{s\|}} = \mathbf{k_{i\|}} - \mathbf{q_{\|}} \pm \mathbf{G}_{hk}$$

where $\mathbf{G}_{hk}$ is the 2D reciprocal lattice vector parallel to the surface.

If we treat the incoming and scattering electron beams as plane waves, it will have the relationship $E = (\hbar\mathbf{k})^2/2m_e$, where m_e is the electron mass. Thus from the geometry in Figure 2.14 the momentum transfer parallel to the surface can be

calculated through the following equation:

$$\mathbf{q}_{\parallel} = \frac{\sqrt{2m_e}}{\hbar} \left(\sqrt{E_i} \sin\theta_i - \sqrt{E_i - \hbar\omega} \sin\theta_s \right) \pm \mathbf{G}_{hk} \tag{2.8}$$

From Equation 2.8 once the geometry and energy of the electron beams are de-termined, the energy and momentum transfer can be thus calculated. Since the probed quasiparticle excitation energy is usually very small ($\sim$ meV), low energy (normally 7 eV) and fine tuning of electron beam both in monochromator and analyzer are required.

2.2.1 Instrument

The sketch of a HREELS instrument is shown in Figure 2.15. An electron beam created by the cathode is tuned by two monochromators (one coarse and one fine) to tune an electron beam and then scattered off the sample surface. The analyzer works like another fine monochromator and tunes the scattered beam one more time. Finally the counting rate is collected at different energy levels by the channeltron electron multiplier (CEM).
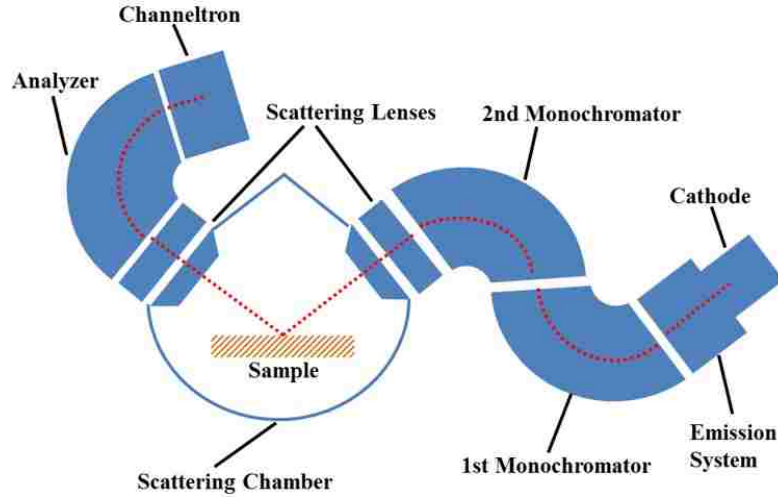
FIGURE 2.15: Sketch of a HREELS

Traditionally the different energy level is controlled through the voltage (energy) level of the analyzer. The CEM scans the analyzer's energy level with range and

step set by the user. Such step-by-step scan analyzer is called a single channel analyzer. The analyzer can be replaced by a multi channel analyzer (MCA) shown in Figure 2.16, which allows to collect data at multiple channels simultaneously over 800 channels and is 100-150 times faster.

FIGURE 2.16: Photo of a MCA analyzer

The comparison of a single channel analyzer and a MCA is sketched in Figure 2.17. For a single channel analyzer, the electron multiplier only "sees" the electrons that passing through the exit slit with a single energy (i.e. single channel). Through tuning the voltage level of the analyzer it can detect the electron counting rates with higher or lower energies. It is like virtually "moving" the analyzer positions, shown in Fig. 2.17(a) For a MCA, when electrons with slightly different velocities (energies) enters the analyzer, the faster ones with larger energy travel along the outside route while the slower ones travel inside. With proper calibration of energy vs position, a position analyzer can collect the information of counting rates at different locations, thus collecting data at multiple channels, shown in Fig. 2.17(b)
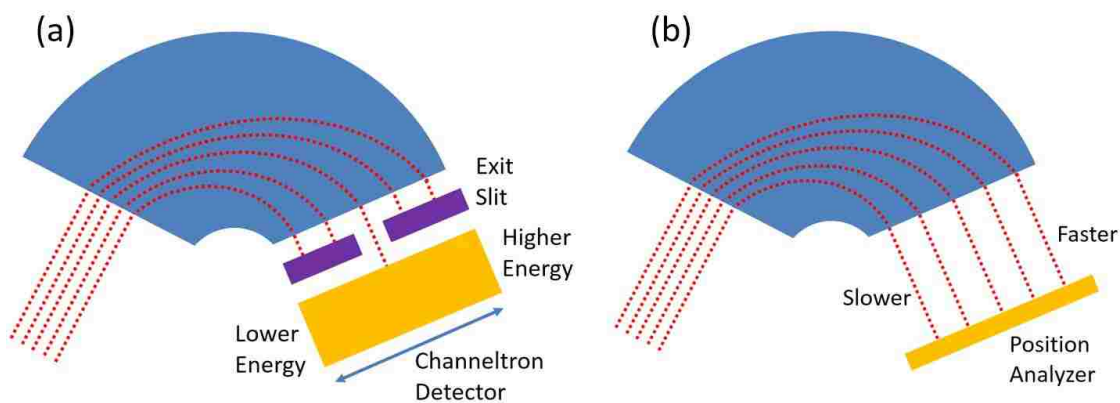
FIGURE 2.17: (a) Sketch of a single channel analyzer (channeltron multiplier). (b) Sketch of a MCA analyzer.

2.2.2   Dipole Scattering Regime
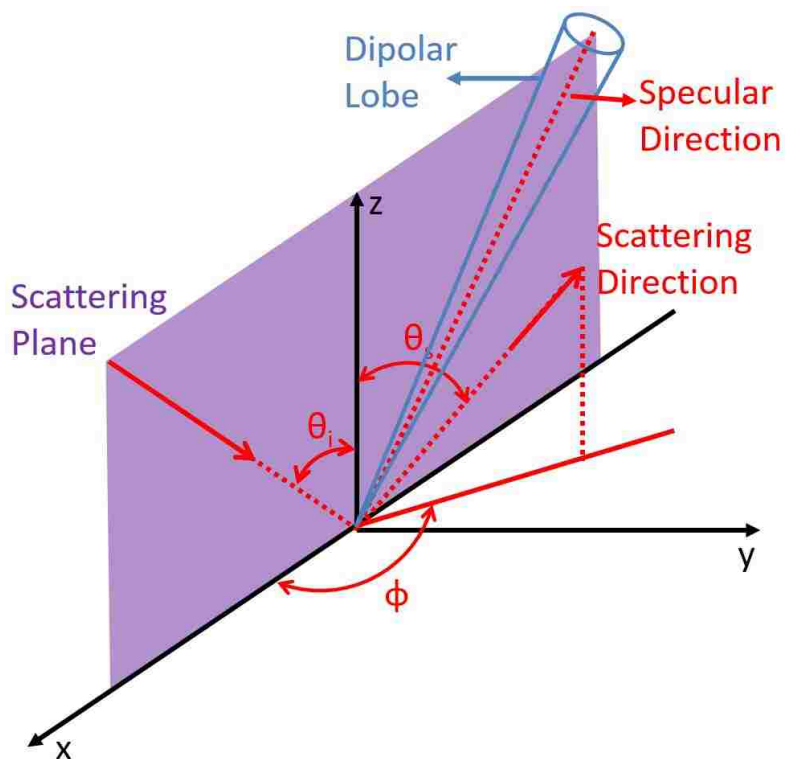
FIGURE 2.18: The scattering geometry for the impact scattering regime.

To understand the HREELS spectrum, there are two scattering regimes with different scattering mechanisms and selection rules: dipole scattering and impact scattering. Shown in Fig. 2.18, the scattering mechanism within the dipolar lobe

is ruled by the dipole scattering, and the scattering mechanism outside the dipolar lobe is ruled by the impact scattering. Although in general these two mechanisms are considered separately under different conditions, they govern the whole scattering process at the same time. For instance, the small angle dipolar lobe is actually superimposed on the broad impact regime. A complete understanding shall incorporate both into a single expression. It is for the convenience of theorists to develop and analyze them separately.

When the electrons are scattered in small angles around specular direction, the dipole scattering mechanism dominates the process. Technically the "small" angle can be approximately estimated around $\theta \approx \hbar\omega_0/2E_i$, where $\hbar\omega_0$ is the excitation energy, and E_i is the incident (impact) energy of the electron [100].

The dipole scattering selection rule states: within this scattering lobe, the electrons interact with the vibration mode that has a long range dipole moment perpendicular to the surface. The "long range" means the scattering event happens when the incoming or outgoing electron is above the sample surface. This can be estimated through $1/\mathbf{q}_\parallel$, where $\mathbf{q}_\parallel$ is the mementum transfer parallel to the surface as in Equation 2.8. For example, for an energy loss of 1000 cm^{-1} (124 meV), and impact electron of 5 eV. The scattering lobe is $\sim$7°, and the scattering distance is $\sim$60 $\mathring{A}$ above the surface [100].

The selection rule can be understood through the following image charge picture: Figure 2.19 shows two different situations of dipole moment on top of the surface. One is perpendicular (2.19a) and one is parallel (2.19b) with respect to the surface. In the former case the image charge created inside the material will enhance the surface dipole, while in the latter the image dipole and real dipole will cancel each other.
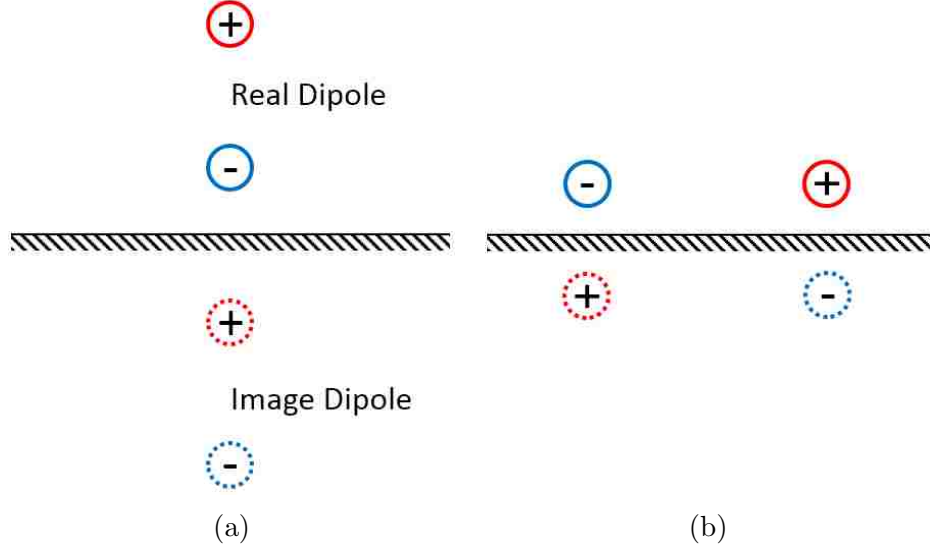
FIGURE 2.19: Two different types of image charges near the surface. (a) Image charge of a dipole perpendicular to the surface, and (b) Image charge of a dipole parallel to the surface.

A better understanding of the dipole scattering mechanism requires the calculation of the scattering cross section from the interaction of the dipole moment and the electric field generated by the incident electron and its image charge. One could refer to the book [100] for more details.

The incident electron feels the electric potential created by the surface dipole and its image. Taking into account different possible scattering processes, the probability of an electron scattering from its initial state into a final state in the solid angle $d\Omega(\hat{k}_S)$ and in the energy range $d\hbar\omega$ can be written as

$$
\frac{d^2 S}{d\Omega(\hat{k}_S)d\hbar\omega} = \frac{m^2 e^2 v_\perp^2}{2\pi^2 \hbar^5 \cos\theta_i} \left(\frac{k_s}{k_i}\right) \frac{P(\mathbf{Q}_\parallel,\omega)}{Q_\parallel^2}
$$
$$
\times \frac{\left| v_\perp Q_\parallel (R_s+R_i)+i(R_i-R_s)(\omega-\mathbf{v}_\parallel\cdot\mathbf{Q}_\parallel) \right|^2}{[v_\perp^2 Q_\parallel^2 + (\omega-\mathbf{v}_\parallel\cdot\mathbf{Q}_\parallel)^2]^2}
\tag{2.9}
$$

where $v_\perp$ and $v_\parallel$ are the speed of incident electron perpendicular and parallel to the surface, k_i and k_s are the magnitude of momentum of incident and scattered electron, $\mathbf{Q}_\parallel$ is the momentum transfer parallel to the surface which satisfies $\mathbf{k}_\parallel^\mathbf{s} = \mathbf{k}_\parallel^\mathbf{i} - \mathbf{Q}_\parallel$, R_i and R_s are the probablility amplitudes that describe specular reflection

of the incident and scattered electron, and the quantity $P(\mathbf{Q}_\parallel, \omega)$ is defined as

$$
\begin{aligned}
P(\mathbf{Q}_\parallel, \omega) = & \int d^2x_\parallel \int_{-\infty}^{+\infty} dt \exp(i\mathbf{x}_\parallel \cdot \mathbf{Q}_\parallel - i\omega t) \\
& \times \int_{-\infty}^{0+} dz' \int_{-\infty}^{0+} dz'' \exp(Q_\parallel[z' + z'']) \left\langle \rho_1(\mathbf{x}_\parallel z'', t)\rho_1(0z', 0) \right\rangle_T
\end{aligned}
\tag{2.10}
$$

which is related to the fluctuating charge density ρ (dynamic dipole) of the medium at different positions $\mathbf{x}$ under the average of quantity at temperature T.

With the assumption $R_s \cong R_i$, which usually satisfies when there is no fine structure resonances (requires special energy and angle), Equation 2.9 can be greatly simplified as

$$
\frac{d^2 S}{d\Omega(\hat{k}_S)d\hbar\omega} = \frac{2m^2 e^2 v_\perp^4}{\pi\hbar^5 \cos\theta_i} \left(\frac{k_s}{k_i}\right) \frac{|R_i|^2 P(\mathbf{Q}_\parallel, \omega)}{[v_\parallel^2 Q_\parallel^2 + (\omega - \mathbf{v}_\parallel \cdot \mathbf{Q}_\parallel)^2]^2}
\tag{2.11}
$$

It is seen that the probability is mainly related to the function $P(\mathbf{Q}_\parallel, \omega)$, while all other components are determined by the experimental setup. We will focus on $P(\mathbf{Q}_\parallel, \omega)$ in the following discussion.

We take the material into two parts: a surface layer with thickness d and dielectric constant ϵ_s, and a semi-infinite substrate with dielectric constant ϵ_b. Then the probability $\frac{d^2 S}{d\Omega(\hat{k}_S)d\hbar\omega}$ can be separated into two parts: surface and bulk contributions, from the electron scattering above the crystal by electric field fluctuations produced by surface and bulk excitations respectively. Here we only draw some important conclusions without equations: (1) The bulk contribution depends solely on the bulk property. However the surface contribution also includes a bulk dielectric constant term $\epsilon_s(\omega)$, which could be understood as the image charge inside the substrate for simplicity. (2) The surface contribution is proportional to a factor of $Q_\parallel d$, which makes the surface contribution decreases less rapidly than the bulk contribution when observed off specular direction ($Q_\parallel \neq 0$).

If we treat this excitation in the same analogy in as the infrared reflection spectroscopy, the energy loss excitation can be related to the imaginary part of the inverse dielectric constant, namely $\text{Im}(1/\epsilon_s(\omega))$. The integrated intensity of an electron loss from surface contribution divided by the elastic intensity can be written as, in the limit $\hbar\omega_s \gg k_B T$,

$$\frac{I_{inel}}{I_{el}} = \frac{2\pi\hbar}{a_0 E_i \cos\theta_i}(1 - 2\theta_E)^{1/2} F_s(\hat{\theta}_c)\frac{e^{*2} n_s}{M_r \omega_s \varepsilon_\infty^2} \tag{2.12}$$

where θ_E is the scattering lobe $\hbar\omega/2E_i$, e^* and M_r are reduced charge and mass, and $F_s(\hat{\theta}_c)$ is a function related to scattering geometry where $\hat{\theta}_c = \theta/\theta_E$.

The last part of Equation 2.12 can be rewritten using the expectation value of the perpendicular component of the dipole moment,

$$\frac{\hbar e^{*2}}{2M_r \omega_s} = |\langle 0\,|\mu_\perp|\,\nu\rangle|^2 \tag{2.13}$$

where $\langle 0\,|\mu_\perp|\,\nu\rangle$ is the transition probability from the 0th ground state to the νth excited vibrational state. Then Equation 2.12 becomes

$$\frac{I_{inel}}{I_{el}} = \frac{4\pi(1 - 2\theta_E)^{1/2} n_s}{a_0 E_i \cos\theta_i \varepsilon_\infty^2}|\langle 0\,|\mu_\perp|\,v\rangle|^2 F_s(\hat{\theta}_c) \tag{2.14}$$

From Equation 2.14, $\langle 0\,|\mu_\perp|\,\nu\rangle$ is only related to the perpendicular of the dipole moment, therefore the same dipole scattering selection rule can be again deduced.

2.2.3 Impact Scattering Regime

When the analyzer is at off specular direction with θ_s much different than θ_i, the simple phenomenological picture of dipole scattering fails to model the scattering process, especially for the emergence of peaks from the dipole forbidden vibration

modes. A complete description using a microscopic theory is necessary for this impact scattering regime.

The scattering distance is again examined by estimating $1/\mathbf{q}_\parallel$. At large off specular angle, the momentum transfer from the energy loss is small compared to geometry. For instance, when the incident energy is 10 eV, and the off specular angle is $\sim$20-30°, the momentum transfer is $\sim$1 Å, which is very close to the surface.

The vibration mode can be described by its wave number $\mathbf{Q}_{\parallel\nu}$, where ν is the phonon mode's label. Then the scattering cross section at the surface area A can be written as:

$$\frac{dS(\mathbf{k}_i, \mathbf{k}_s)}{d\Omega} = \frac{mE_i\cos^2\theta_s}{2\pi^2\hbar^2\cos\theta_i}A\big|M\left(\mathbf{k}_i, \mathbf{k}_s; \mathbf{Q}_{\parallel\nu}\right)\big|^2 \tag{2.15}$$

where M is the matrix element given by

$$M\left(\mathbf{k}_i, \mathbf{k}_s; \mathbf{Q}_{\parallel\nu}\right) = \sqrt{1 + n_\nu}\sqrt{\frac{\hbar}{2N\omega_\nu}}\left(\frac{\partial f}{\partial\mathbf{Q}_{\parallel\nu}}\right) \tag{2.16}$$

where N is the number of unit cells in the system, n_ν is the number of phonons present and

$$\frac{\partial f}{\partial\mathbf{Q}_{\parallel\nu}} = \sum_{j,\alpha}\left(\frac{\partial f}{\partial R_{j,\alpha}}\right)_0\frac{\xi_{j,\alpha}^\nu}{\sqrt{M_j}} \tag{2.17}$$

where f is the scattering amplitude, $R_{j,\alpha}$ is the atomic position of jth atom in Cartesian direction α, $\xi_{j,\alpha}^\nu$ is the amplitude of the displacement of nucleus j for the phonon mode $\mathbf{Q}_{\parallel\nu}$ (summing up $\xi_{j,\alpha}^\nu$ using creation and annihilation operators with respect to different normal modes can give the total displacement of the nucleus).

Now the problem is simplified into estimating the value of $\frac{\partial f}{\partial \mathbf{Q}_{\|\nu}}$, which can again be written in the following form under the crystal potential V:

$$\frac{\partial f}{\partial \mathbf{Q}_{\|\nu}} = \left\langle \psi_{k_s}^+ \left| \frac{\partial V}{\partial \mathbf{Q}_{\|\nu}} \right| \psi_{k_i}^- \right\rangle \tag{2.18}$$

where $\psi_{k_{s(i)}}^{+(-)}$ denotes the outgoing (incoming) scattered (incident) electron wave function.

A good model of the crystal potential is the muffin-tin potential and multiple scattering is also considered in the impact scattering theory. When the electron approaches the surface, it engages the crystal potential and goes through multiple scattering. Then it scatters off the nucleus which has certain displacement. The deflected electron subsequently follows the path that can be described in the theory of angle-resolved photoemission. Meanwhile it again goes through multiple scattering before finally leaving the crystal.

The scattering geometry is shown in Figure 2.18. The scattering plane is determined by the incident electron beam (k_i) and the surface normal, which is the xy plane in current situation. The scattering angle θ_s is between the scattered electron beam (k_s) and the surface normal, while ϕ is between the projection of k_s onto xy plane and x axis. When $\phi = 0$, the scattered electron is within the scattering plane, and additionally when $\theta_s = \theta_i$, the scattering is along specular direction.

The selection rule for impact scattering regime is intimated related to the surface symmetry, as it is deduced from symmetry argument of Equation 2.18. It can be understood in two folds. First, with the geometry setup in Figure 2.18, if the yz plane is a plane of reflection symmetry (or z axis is an axis of two fold rotation), and the vibrational mode is odd under the reflection (or rotation), then this symmetry operation combined with time-reversal invariance leads to the vanishing of the scattering amplitude ($\partial f / \partial \mathbf{Q}_{\|\nu}$) when the scattered electron is

69

along the specular direction. Note this calculation is under the assumption that the incident and scattering electrons are having the same energy thus same magnitude of wave vector.

Second, if the scattering plane, xz plane, is a plane of reflection of the surface, the scattering amplitude $(\partial f/\partial \mathbf{Q}_{\parallel\nu})$ vanishes when the symmetry of vibrational mode is odd with respect to this plane. If the symmetry of vibrational mode is odd within the plane and even under reflection, its scattering cross section is non-vanishing.

A simple understanding of the **impact scattering selection rule** is that the incoming and scattered electron both have even parity with respect to the scattering plane, thus the vibration mode must also be even with respect to the same plane in order to have non-vanishing cross section.

One famous example of impact scattering the vibrational modes of adsorbed H on the surface of W(100) [17]. Shown in Figure 2.20 is its angular profile of inelastically scattered electron intensities. It shows the intensity of the specular peak drops by two orders of magnitude when the angular deflection is 5°. The peak at 130 meV is from the vibrational mode of H normal to the surface. As seen the drop off behavior of this mode is almost the same as the elastic peak. The peak at 260 meV is the overtone of this mode.

Of importance is the peak at 80 meV, which is not seen at small off-specular angle. It is a mode of H moving parallel to the surface and out of the plane containing the H and two W atoms. This is forbidden in dipole scattering but allowed in impact scattering. The cross section increases with increased off-specular angle.
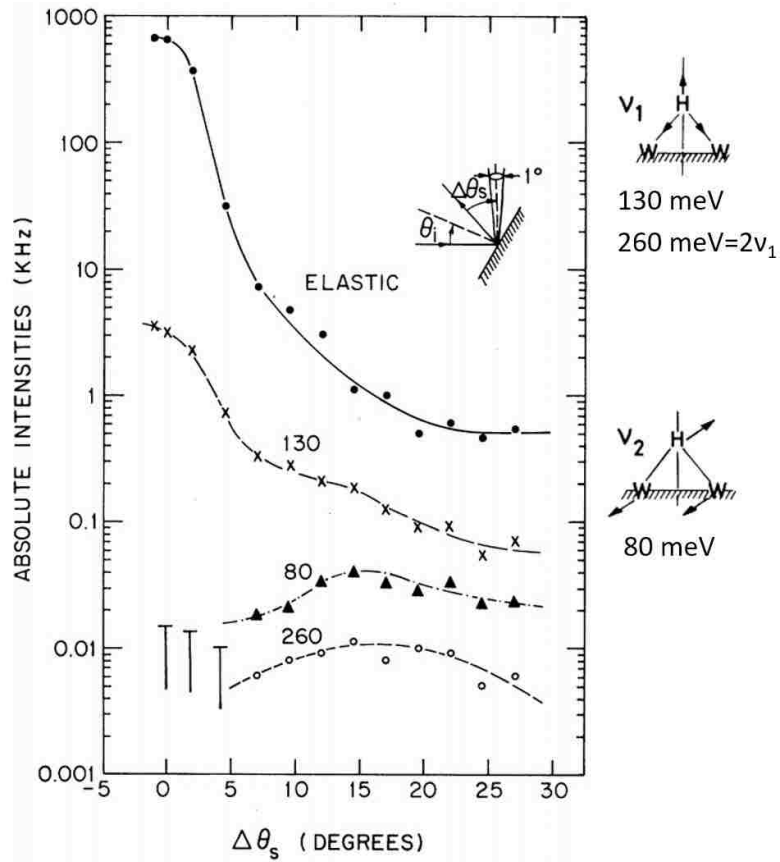
FIGURE 2.20: Angle dependence of the absolute intensities as a function of the collection angle $\Delta\theta_s = \theta_s - \theta_i$. Figure is adapted from [17].

In general, the impact scattering cross section increases with larger incident electron beam energy, which is in opposite to the dipole scattering. Therefore by applying different experimental setup and combining two selection rules, one can emphasize different vibrational modes.

Chapter 3

Anomalous Surface Lattice Dynamics in the Low-Temperature Phase of $Ba(Fe_{1-x}Co_x)_2As_2$

3.1 Introduction

The recent discovery of high-temperature superconductivity in layered iron-based compounds [26] has created enormous activity in the scientific community. One of the most intriguing aspects of these new compounds is the intimate coupling between spin and lattice, offering a wonderful platform to study and manipulate their relationship. The parent compounds (no disorder induced by doping) of the 122 family (Alkaline earth $(A)Fe_2As_2$) exhibit a coupled magnetic and structural transition from the low-temperature (LT) antiferromagnetic orthorhombic phase to a high-temperature (HT) paramagnetic tetragonal phase [101, 27, 102], which has the signature of being first order in the bulk. Figure 3.1 shows the phase diagram for the compound of interest, $Ba(Fe_{1-x}Co_x)_2As_2$ [27], where doping the parent compound (Co for Fe) lowers the transition temperatures and at $x \sim 2.2\%$, there seems to be a tricritical point beyond which the magnetic transition becomes second order [101, 102]. The strong spin-lattice coupling in these systems [102, 103, 104, 105], along with the presence of a tricritical point, creates an environment where either strongly first-order or nearly second-order phase transitions may be observed. Creating a surface by cleaving these layered materials is a controlled way to tip the balance between competing phases, thus providing a unique opportunity to study the subtle aspects of the interactions between lattice and spin through charge. Important for this study is the fact that broken symmetry at the surface creates a significant enhancement in the spin-orbit coupling [106, 107].

Although the nature of the coupled transitions in $BaFe_2As_2$ (Ba122) is still in debate, measurements on the sister compounds $CaFe_2As_2$ (Ca122) and $SrFe_2As_2$
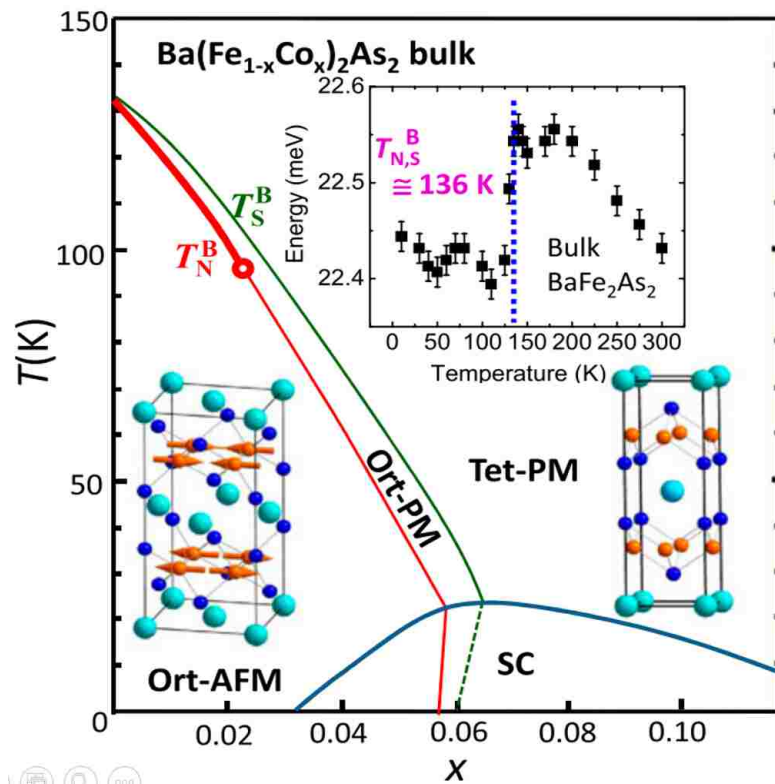
FIGURE 3.1: The T-x phase diagram for bulk $\mathrm{Ba(Fe_{1-x}Co_x)_2As_2}$, reproduced from [27]

show that the structural and magnetic transitions are discontinuous and hysteretic (i.e., a first-order transition) [101, 102, 103, 104]. One distinct signature of this coupled transition in the bulk, relevant to this study, is the change in energy and width of the phonon modes as a function of temperature (magnetoelastic coupling) [108, 109, 1, 110, 2]. Figure 3.1 inset shows the energy as a function of temperature for the A_{1g} mode (out-of-plane As vibration) for Ba122 [1], displaying a 0.7% jump to higher energy at the transition into the HT phase, always softer in the LT phase. This trend is in contrast to the modes in Ca122, where the transitions occur at a higher temperature and seem to be more intimately coupled. According to Raman spectroscopy measurements, the B_{1g} mode (out-of-plane vibration of Fe atoms) in Ca122 shows a 1.9% jump at the transition but to lower energy in the HT phase [2]. The phonon energy displays a large linear decrease as temperature increases in the LT phase, with a much smaller change in the HT phase. In many aspects, the result presented here is more consistent with the vibrational properties of Ca122 than Ba122. The surface transition temperature is higher than in the bulk mirroring that is seen in the bulk of Ba122 with the application of a uniaxial pressure [111]. The temperature dependence of the energy of the surface A_{1g} mode in the LT phase is gigantic, two orders of magnitude larger than in the bulk, a consequence of an enhanced surface spin-lattice coupling.

The close coupling between geometric and magnetic structure in these materials has been the subject of many theoretical papers, of which several are directly relevant to this study. Yin *et al.* [112] first noted the possibility of strong spin-phonon coupling and found that the magnetism is closely tied to the lattice deformation. Aktürk and Ciraci [113] predicted that phonon modes (associated with the motion of Fe-As) in the HT tetragonal phase of Ba122 will soften in the LT antiferromagnetic orthorhombic phase. This softening is not associated with the traditional

mode softening driving structural transition. Yildirim [114] calculated the influence of Fe magnetic moment on the Fe-As and As-As bonding, which changes dramatically as a function of magnetic moment, and pointed out that, through the spin-charge-lattice coupling, spin may play a much more significant role than generally assumed. Mazin and Johannes [115] describe a model with dynamic twin and antiphase spin domain walls that seems to explain many experimental observations, including the temperature separation of the structural and magnetic transitions. STM measurements show that the surface can stabilize these dynamic fluctuations at a structural antiphase boundary [70].

3.2   Experiments

Single crystals of $BaFe_2As_2$ and $Ba(Fe_{0.95}Co_{0.05})_2As_2$ are grown by the self-flux method out of an Sn flux using conventional high-temperature solution growth techniques [116]. The doping level of the doped sample is ~ 0.05 as determined by wavelength dispersive X-ray spectroscopy. X-ray diffraction, magnetic susceptibility, Hall, and transport measurements are used to characterize all of the samples. The typical crystal size is $\sim 0.1 \times 2 \times 2$ mm^3, with platelet morphology.

The samples are cleaved insitu at 86 K, producing a clean (001) surface and showing a sharp p(1×1) LEED pattern. The instrument used in this experiment is HREELS. The incident electron energy is 20 eV with 65° incident angle. The measurements are done in the specularly reflected direction, which means the momentum of the phonon is zero (*i.e.*, the Brillouin zone center). In other words, the probed phonon modes are surface dipole (infrared) active modes moving along the z-direction.

3.3   HREELS Results

Figure 3.2 displays an EELS spectrum from $Ba(Fe_{0.95}Co_{0.05})_2As_2$ single crystals taken at an incident electron energy E_0=20 eV and a temperature of 46 K. Three

phonon peaks are identified as $\hbar\omega_1$, $\hbar\omega_2$, and $\hbar\omega_3$ with energies 33.5, 26.5, and 14.0 meV, respectively. Based on the previous studies for the bulk [108, 109, 1, 110, 2, 113], we can identify these modes (Figure 3.2 inset): $\hbar\omega_1$ and $\hbar\omega_2$ are modes associated with Fe and As vibrations, corresponding to the bulk A_{2u} (out-of-plane Fe/As vibration) and the A_{1g} (out-of-plane As vibration), and $\hbar\omega_3$ seems to be related to the E_u mode involving the in-plane stretching vibration of Ba atoms. Both the A_{1g} and E_u modes are Raman active in the bulk but infrared active at the surface. The presence of the surface breaks the inversion symmetry present for the bulk A_{1g} mode. The background is a combination of the instrumental line shape and the Drude spectral weight, which is a measure of the electronic density of states near the Fermi energy (electron/hole excitation spectra). The dashed line is the Drude spectral weight background. The detail of the fitting procedure and Drude spectral weight analysis is explained below.

The HREELS spectra, like those spectra shown in Fig. 3.2, are composed of the quasielastic reflected beam, phonon modes (both excited and absorbed), and both interband transitions and intraband transitions. The phonons are observed as loss peaks in the spectra, whereas the intraband transitions are associated with a continuum of electron hole excitations around the Fermi energy. This continuum is known as the Drude spectral weight, and it is a measure of metallicity of the surface. The phonon modes are fit with the Lorentzian function. The process is shown in Fig. 3.3 for the 5% Co-doped sample at 46 K. The inherent line width of each phonon mode is obtained by deconvolution with the quasielastic peak, which is 1.4 meV for the doped sample and 3 meV for the undoped sample. The deconvolution function is inherent width = [(measured width)^2 - (instrument resolution)^2]$^{1/2}$.

The background after the loss peaks have been removed is analyzed to extract the Drude spectral weight at the surface to determine the temperature and doping
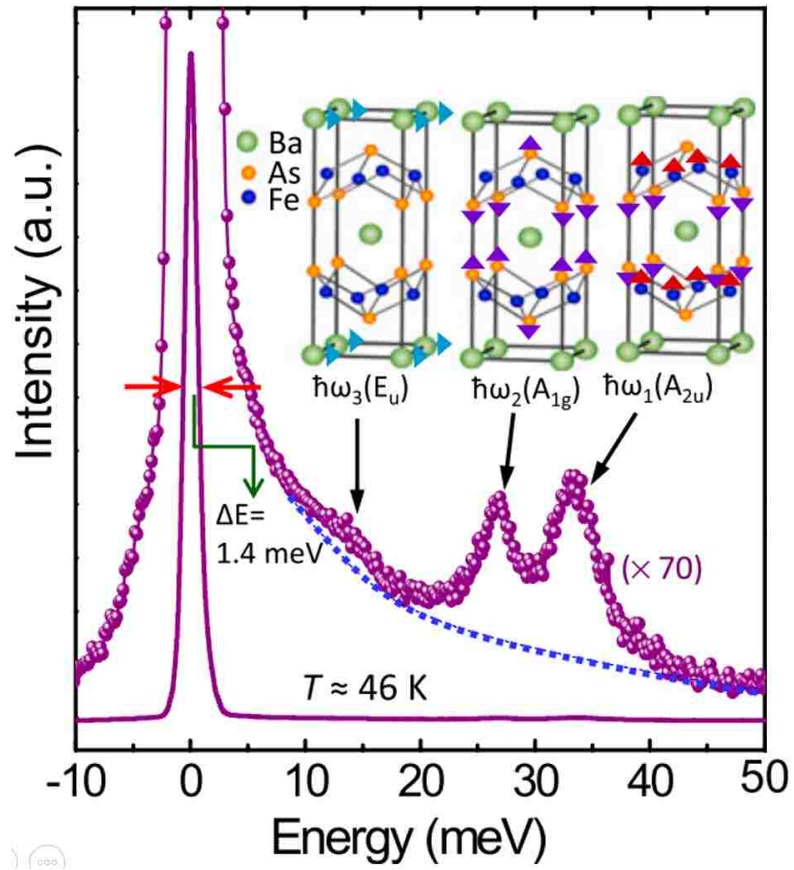
FIGURE 3.2: EELS phonon spectra for the surface of $Ba(Fe_{0.95}Co_{0.05})_2As_2$ at 46 K. The blue dotted line is the background caused by the Drude spectral weight. (Insets) Schematic representation of the three vibration modes.

dependence of electron density near the Fermi energy (i.e., the metallicity of the surface). There are detailed measurements of the optical conductivity that can be used to guide the fitting procedure [117, 118, 119]. In the energy range relevant to our study, the optical data are fit with a narrow Drude and a wide Drude spectral function. The narrow Drude spectral weight changes with different parent materials and as a function of doping, whereas the broad Drude spectral weight seems to reflect the considerable background in all of these Fe base 122 materials [118]. The wide Drude contribution will be treated as a background in our fitting. Therefore, we will fit the data with the following function:

$$I_{DSW}(\omega) = I_0 + \frac{A\Gamma}{(\omega - \omega_0)^2 + \Gamma^2} \tag{3.1}$$

where I_0 is a combination of the random background counts and the signal from the wide Drude spectral weight. Γ is the width, which can be a function of ω, T, and doping level. Optical measurements on Ba122 indicate that the width can be as small as ~ 7 meV at low temperature and increases appreciably when entering the tetragonal phase [118]. A is proportional to the electron density at or near the Fermi energy, which is a measure of carrier density at the Fermi energy.

For each spectra, we make sure that the voltage reading from the spectrometer gives the correct zero (ω_0). After the zero of energy is determined, the curves are normalized by integrating from -40 to 50 meV. The quasielastic peak is removed, and the remaining spectral function is fit with Eq. 3.1 over an energy range from 20 to 60 meV. Figure 3.4 shows the results of this fitting for the data from the undoped sample. The squares represent using a fixed width of 10 meV, and the circles are a fit with a width of 10 meV in the low-temperature phase and 50 meV for the high-temperature phase. Qualitatively, there is no difference; the Drude spectral weight in the low-temperature antiferromagnetic-order orthorhombic phase is appreciably
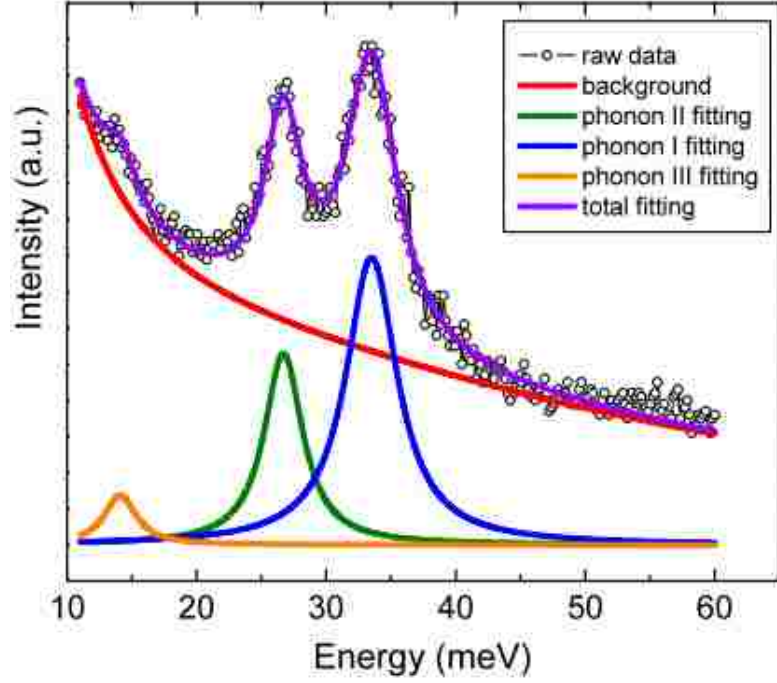
FIGURE 3.3: The fitting procedure for the HREELS spectral of $Ba(Fe_{0.95}Co_{0.05})_2As_2$. After subtracting the background (red line), the left-over phonon part is fitted with three Lorentz functions (purple line). The blue, green, and orange curves are fittings for the three phonon modes, respectively.

larger than in the high-temperature tetragonal phase. The data for the Drude spectral weight for the doped sample shown in Fig. 3.7(b) was obtained using a fitting with a constant width $\Gamma = 10$ meV.

Figure 3.5 displays the T dependence of the loss spectra for $Ba(Fe_{0.95}Co_{0.05})_2As_2$ after removal of the background discussed above. All of the modes soften and broaden as temperature increases. The data shown in Figure 3.5 are fit to determine the energy and line width for the intense A_{1g} and A_{2u} modes, with the results displayed in Figure 3.6. Figure 3.6 (a) and (c) is for the energy, and 3.6 (b) and (d) is for the line width. A simple linear fit (dashed line) to the data in the two temperature regions gives a surface transition temperature of $T^S \sim 65$ K, higher than both the bulk structural transition for $Ba(Fe_{0.95}Co_{0.05})_2As_2$ at 60 K and the
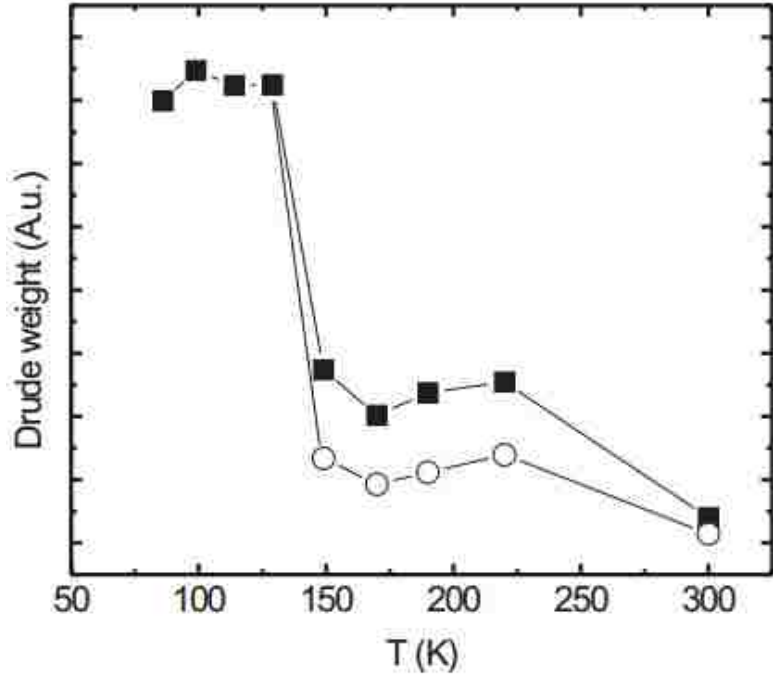
FIGURE 3.4: Drude spectral weight for BaFe$_2$As$_2$. Solid points are for a fixed width, and the open circles are for a larger width in the high-temperature phase.

magnetic transition at 45 K, as determined from the resistivity data shown in Figure 3.7(a).

Figure 3.8 shows the T dependence of the energy and line width of the $\hbar\omega_1$ and $\hbar\omega_2$ phonon modes for the parent compound BaFe$_2$As$_2$. Notice that the energy of each mode in the HT tetragonal paramagnetic phase is independent on doping level. 3.8(a), a repeat of Figure 3.9 inset, is included to enable a detailed comparison with the bulk A$_{1g}$ mode and a fit using an anharmonic potential. Clearly, the transition temperature $T^S \sim 150$ K for both modes is considerably higher than the coupled bulk structural/magnetic transition at 136 K (Figure 3.8 inset). All of modes, for $x = 0$ and $x = 0.05$, exhibit strong T dependence in the LT phase but very gradual (normal) changes in the HT phase. $dE(A_{1g})/dT$ is ~ 300 times larger at the surface than in the bulk (Figure 3.8) in the LT phase. The difference between the bulk and surface for $x = 0.05$ is probably even larger, because the temperature dependence

81
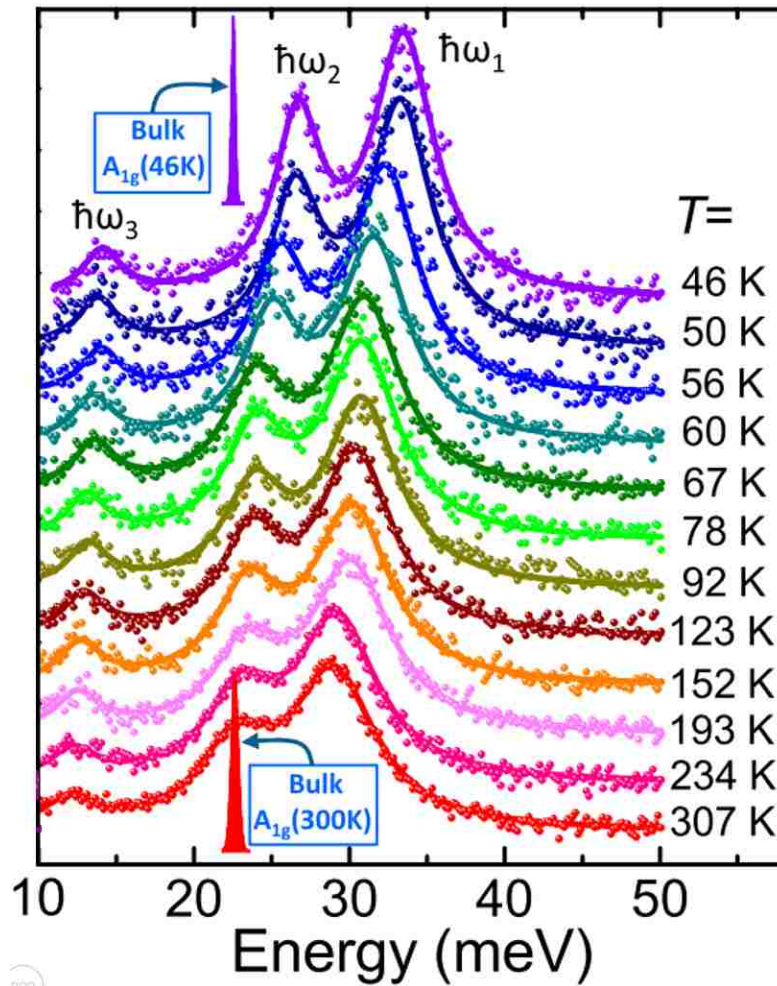
FIGURE 3.5: T-dependent spectra with background subtracted. The solid vertical peaks show the energy and width of the bulk A_{1g} mode at 46 and 300 K [1]
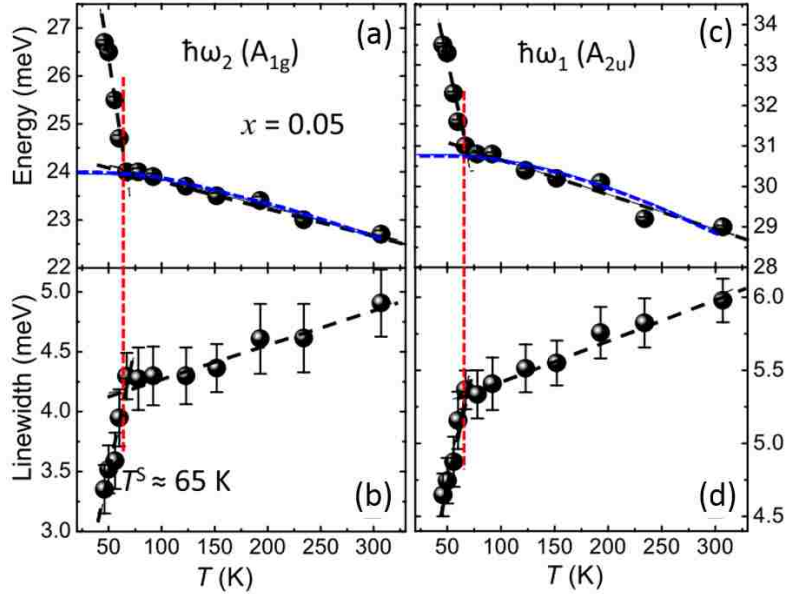
FIGURE 3.6: T dependence of the phonon energy and line width of the surface phonon modes $\hbar\omega_2$ ((a) and (b)) and $\hbar\omega_1$ ((c) and (d)). The vertical (red) lines mark the transition at 65 K. The blue line is the fit of the HT data to an anharmonic potential; the line is dashed in the LT phase.

in the bulk is very small [120]. Surprisingly, we do not see a discontinuous change in energy at the transition temperature as seen in the bulk (Figure 3.1 inset), but with the enhanced line width of ~ 9.5 meV ($x = 0$) at the transition temperature, the jump would have to be $\geq 5\%$ to be resolved. The jump observed in the bulk of Ba122 (Figure 3.1 inset) is only 0.7%[1]. The equivalent number for the jump in Ca122 is 1.9%[2].

Although the behavior in the HT phase is similar for both surface and bulk, there is a dramatic difference between the surface and the bulk in the LT phase. As clearly shown in Figure 3.6 and 3.8, there is gigantic softening accompanied by a sharp increase in the line width for the surface phonon modes as temperature increases in the orthorhombic LT phase. Experiment and theory both show that the phonon modes in the bulk for Ba122 (associated with Fe-As vibrations) soften in the orthorhombic phase compared with the tetragonal phase [1, 113] but obviously,
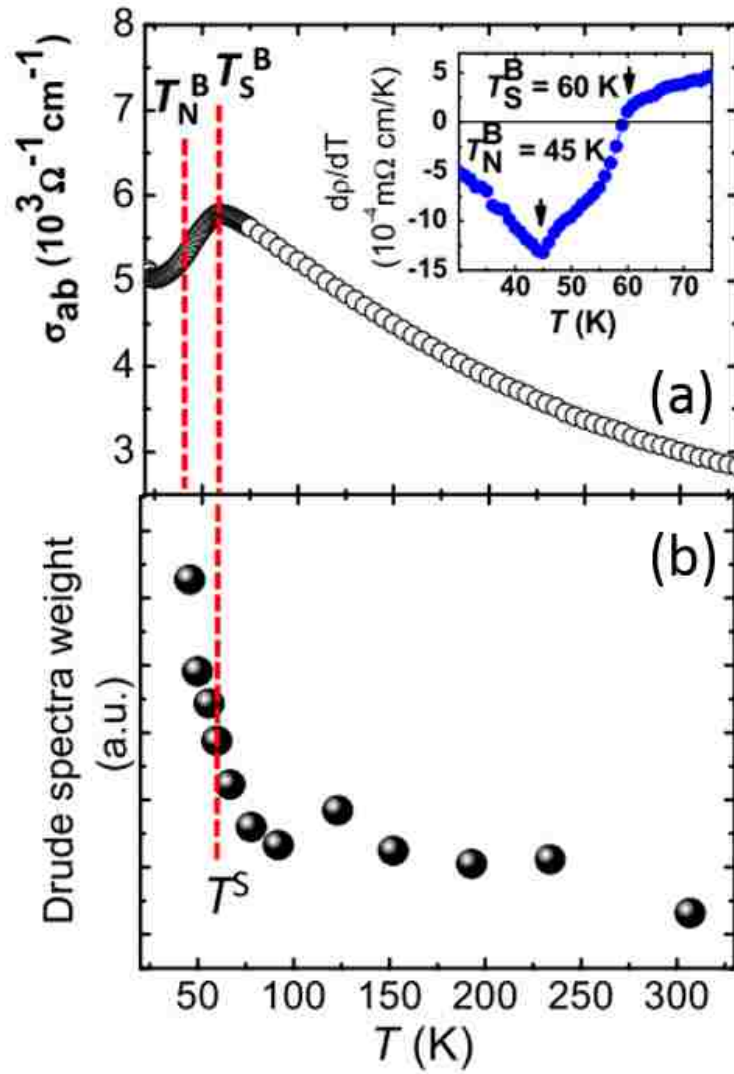
FIGURE 3.7: (a) In-plane conductivity. Inset is the derivative of the in-plane resistivity. (b) T dependence of Drude weight.
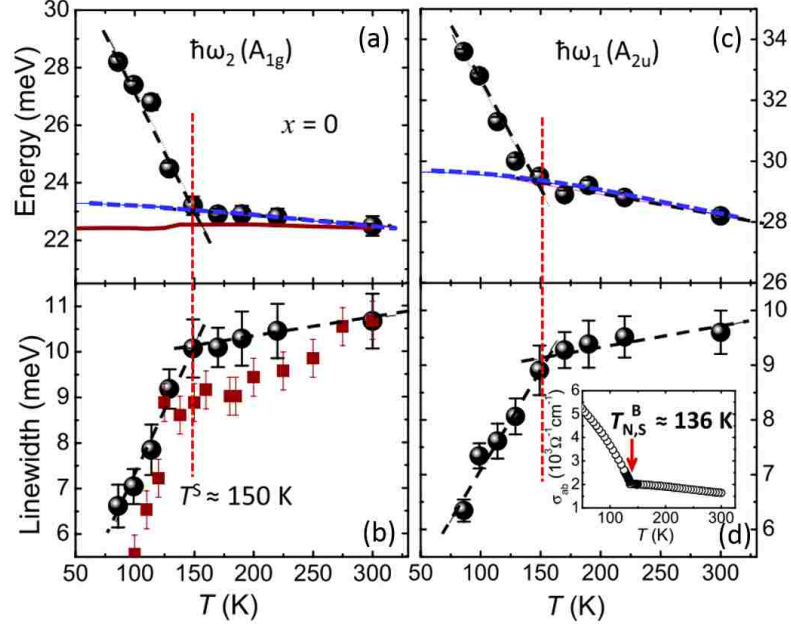
FIGURE 3.8: T dependence of the phonon energy and line width of the surface phonon modes $\hbar\omega_2$ ((a) and (b)) and $\hbar\omega_1$ ((c) and (d)) on $BaFe_2As_2$.

not at the surface. As stated previously, the modes for the surface of Ba122 look more like the bulk modes of Ca122 than Ba122. For comparison, we also plot in Figure 3.8 the data for the A_{1g} mode in the bulk [1] (red solid line), originally displayed in Figure 3.1 inset. Both the surface and bulk modes are similar in the HT phase but very different in the LT phase. To illustrate the difference between the surface and bulk in the LT phase, one can compare the T variation of energy (E) and line width (Γ) of the A_{1g} mode in the parent compound: $dE(A_{1g})/dT$ is -83 μeV/K and $d\Gamma(A_{1g})/dT$ is +58 μeV/K for the surface. The equivalent numbers for the bulk A_{1g} mode are only -0.27 and +13 μeV/K, respectively.

Before discussing the data shown in Figure 3.6 and 3.8, we would like to point out that the observed behavior cannot be caused by mixing of a surface Brillouin zone center phonon mode with the bulk dispersion of this mode in the direction perpendicular to the surface. Figure 3.5 shows the energy and width of the bulk A_{1g} mode at 46 and 300 K for the undoped sample [1] compared with the experi-
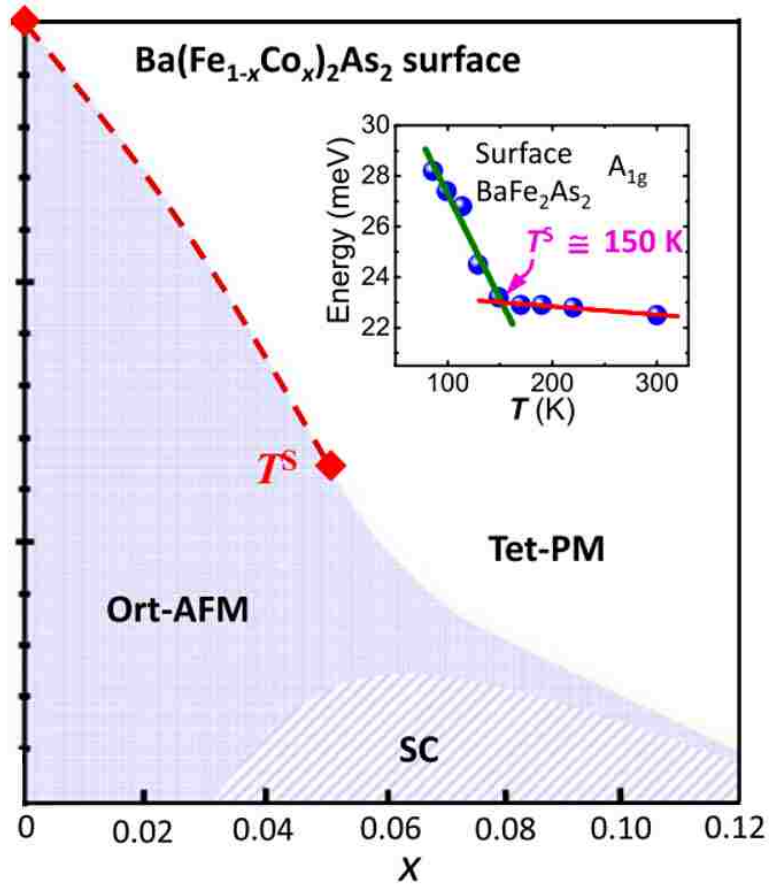
FIGURE 3.9: Proposed T-x phase diagram for the surface of $Ba(Fe_{1-x}Co_x)_2As_2$ based on the results presented here. (Inset) The temperature-dependent phonon shift of A_{1g} surface mode of $BaFe_2As_2$. The transition point is indicated as T^S at 150 K.

mental data for $x = 0.05$. Bulk Raman data show very little shift in energy with doping[120]. It is clear that the surface A_{1g} mode at LT is appreciably higher in energy than the bulk mode at the bulk Brillouin center. Although there is no bulk phonon dispersion measurement for this compound, it is not expected that such an optical mode would have appreciable dispersion in the direction normal to the plane of a layered material. Data for Sr_2RuO_4 [121] and theoretical calculations for a cuprate [122] and an Fe-based superconductor [123] indicate almost no dispersion perpendicular to the plane. In addition, dispersion of the A_g mode in Sr_2RuO_4 is to lower energy, which would not couple to the higher-energy surface mode. Thus, we believe that the observed behavior reflects the properties of the surface.

3.4   Analysis and Conclusions

Table 3.1 presents the characteristic values for the phonon modes at the surface and in the bulk (where data are available). In the LT phase, $dE/dT(LT)$ increases by ~ 300 times for the A_{1g} mode at the surface compared with the bulk ($x = 0$). The slope of the A_{1g} mode line width, $d\Gamma/dT(LT)$, is approximately five times larger at the surface than in the bulk. The large value of $d\Gamma/dT(LT)$ at the surface is independent of doping. However, there is significant doping dependence on $dE/dT(LT)$: approximately two times increase for both modes in the doped sample ($x = 0.05$) compared with the undoped compound ($x = 0$).

TABLE 3.1: Data for the energies, widths, and temperature-dependent changes in the surface and corresponding bulk phonon modes A_{1g} and A_{2u}[1, 2].

	$dE/dT(LT)$ (μeV/K)	$d\Gamma/dT(LT)$ (μeV/K)	$dE/dT(HT)$ (μeV/K)	$d\Gamma/dT(HT)$ (μeV/K)	E (300K) (meV)	Γ (300K) (meV)	χ_α	$\hbar\omega_0$ (meV)
Surface								
$A_{1g}(\hbar\omega_2)(x=0)$	-83.0±9.5	58.2±4.7	-3.2±0.8	4.2±0.6	22.5±2.3	10.6±0.8	0.021±0.003	24.3±0.3
$A_{1g}(\hbar\omega_2)(x=0.05)$	-138.3±11.7	44.6±6.3	-5.6±0.3	2.6±0.3	22.7±1.4	4.9±0.6	0.030±0.002	25.5±0.1
Bulk								
$A_{1g}(x=0)$	-0.27	13	-1.1	1.1	22.4	0.94	0.004	22.6
Surface								
$A_{2u}(\hbar\omega_1)(x=0)$	-69.6±8.4	37.2±4.4	-7.7±1.8	3.9±1.5	28.2±2.3	9.6±0.8	0.035±0.005	31.9±0.5
$A_{2u}(\hbar\omega_1)(x=0.05)$	-128.5±11.4	35.5±3.9	-8.6±0.8	2.8±0.2	39.0±1.4	6.0±0.5	0.042±0.003	33.6±0.3
Bulk								
Ca B_{1g} ($x=0$; 532 nm)	-1.99	5.60	2.01	1.38	25.30	1.24	0.012±0.002	26.3±0.1

The corresponding characteristic values $[dE/dT(HT)$, $d\Gamma/dT(HT)$, E (300 K), and Γ(300 K)] for the HT phase are presented in Table 3.1 as well. At 300 K, the energies of the surface modes are the same for the doped and undoped sample and the same as in the bulk for A_{1g} where data exist. For the undoped samples, there is a three- to fourfold increase in both $dE/dT(HT)$, and $d\Gamma/dT(HT)$ for the A_{1g} mode at the surface compared with the bulk. There is almost no dependence of these quantities on doping level for either mode. The only measurable dependence on doping in the HT phase is the width at 300 K. The modes in the undoped sample have approximately two times the width as in the doped sample, which is counter to the idea that Co dopant will create disorder but consistent with the differences in $d\Gamma/dT(HT)$.

Historically, the change in energy and linewidth of a surface vibration mode with temperature has been modeled with a simple anharmonic potential, such as a Moorse potential [124, 125]. Although it is easy to explain the T dependence of the modes in the HT phase, the mode energy and width in the LT phase cannot be fit using such a simple approach. With an anharmonic potential, the energy between adjacent states is $\Delta E = E_n - E_{n-1} = (1 - 2\chi_\alpha n)\hbar\omega_0$, where χ_α is a dimensionless measure of the anharmonicity [126]. When fitting the temperature dependence of the data, there are two parameters, χ_α and $\hbar\omega_0$. All of the results from the fitting are included in Table 3.1. For an ordinary metal surface, such as Cu(110), χ_α is ~ 0.032 compared with 0.015 in the bulk [124]. The fitting for the HT phase A_{1g} surface mode is shown in both Figure 3.8(a) for x=0 and 3.6(a) for x=0.05. For the parent compound, $\chi_\alpha = 0.021$ and $\hbar\omega_0 = 23.3$ meV, whereas $\chi_\alpha = 0.030$ and $\hbar\omega_0 = 24.0$ meV for x=0.05. A fit for the HT bulk A_{1g} mode (Figure 3.8(a)) gives $\hbar\omega_0 = 22.6$ meV with $\chi_\alpha = 0.004$. These fits give a quite reasonable explanation for the T dependence of the HT modes. The surface has an enhanced anharmonicity as

expected, but the zero temperature mode energy $\hbar\omega_0 = 24.0$ is almost the same for the surface and bulk, and there is no variation with doping. However, the unusual phonon behavior in the LT phase cannot be explained with such a simple model.

Figure 3.7(a) is a plot of the T dependence of in-plane electrical conductivity measured from the single crystal used in this experiment (5% Co doping). Note that, with increasing temperature, conductivity increases until it reaches a maximum at $\sim$ 60 K and then decreases. Figure 3.7(a) inset shows $d\rho_{ab}/dT$ vs.T and indicates the procedure to identify the magnetic transition temperature $T_N(\sim d\rho_{ab}/dT$ maximum) and the structural transition $T_S(d\rho_{ab}/dT = 0)$. Figure 3.7(b) is the measured Drude weight obtained from the background shown in Figure 3.2. It is quite apparent that there is almost no correspondence between the surface Drude weight (surface metallicity) and the bulk in-plane conductivity. However, if the Drude weight for the doped compound is compared with the in-plane conductivity for the parent compound (Figure 3.8(d) inset), the two are very similar. They fall rapidly as the temperature increases in the LT phase but are much less temperature dependent in the HT phase. With the lack of a nonmonotonic T dependence of the Drude spectral weight (Figure 3.7(b)), we conclude that the surface magnetic and structural transitions occur at approximately the same temperature for x=0.05 compound, which is what was implied in the surface phase diagram in Figure 3.9. The continuous nature of the temperature dependence of both energy and line width for x=0 and x=0.05 suggests the absence of a tricritical point at surface.

The dramatic phonon broadening and the sharp phonon softening as $T \to T^S$ unambiguously indicate that the observed surface phonon modes have strong interactions with both charge and spin degrees of freedom. As shown in Figure 3.7(b), the Drude weight decreases rapidly with increasing temperature in the LT phase, indi-

cating the decrease of spectral weight in low-energy electron-hole pair excitation. If the ordinary electron-phonon coupling (EPC; in the nonmagnetic case) is the only channel for phonon decay through electron-hole pair excitations, thus causing phonon broadening, one would not anticipate such a substantial increase of phonon linewidth as $T \to T^S$. In a simple approximation, the probability of phonon decay through EPC is proportional to magnitude of the low-energy electron-hole pair excitations. In Fe-based superconductors, recent theoretical studies indicate that the EPC is weak [127], and angle-resolved photoemission spectroscopy (ARPES) data do not show a large renormalization of the bands near the Fermi energy [128]. Another channel for phonon decay is associated with a strong spin-phonon interaction, such that the change of spin structure may significantly renormalize the phonon energy and lifetime. Because the two phonon modes discussed here are in the As-Fe layer associated with the magnetic ions, spin-charge-lattice coupling should be included, caused by the modulation of the spin exchange integral by lattice vibrations [129, 130, 131, 132, 133]. It should be pointed out that one cannot talk about spin-phonon interaction without the involvement of EPC [133, 132] or spin-orbit coupling [134].

Spin-phonon coupling exists throughout the whole temperature range but only induces a coherent shift of phonon energy in the magnetically ordered phase. When $T > T^S$, the coupling goes incoherent, which results in (1) large phonon peak broadening (incoherence shortens the phonon lifetime) and (2) anharmonicity-induced broadening that dominates the temperature dependence of phonon modes in the HT paramagnetic phase. In $BaFe_2As_2$, the displacement patterns of both A_{1g} (As antiphase vibration) and A_{2u} (mixed Fe/As vibration) modes distort the Fe-As-Fe bond angles, which are involved in the J_{1a} and J_{1b} exchange integrals. All of the short-range exchange integrals between Fe ions occur through the As orbitals. Any

phonon with the lattice vibration in the Fe/As layer should transmit the magnetic interaction and simultaneously modulate the phonon behavior. In the paramagnetic phase with no spin ordering and only the incoherent spin-phonon interaction, the weak temperature dependence of energy reflects only the contribution of anharmonicity. As soon as the system enters the magnetically ordered phase, marked effects caused by magnetic exchange interactions in phonon behavior are expected. This feature is in accordance with other studies of $Ba(Fe_{1-x}Co_x)_2As_2$[114] and LaFeAsO [115], which show strong coupling of the phonon spectra with the magnetic moment of Fe sublattices. Our data indicate that such coupling is enhanced at the surface.

Evidently, the surface amplifies the spin-lattice coupling, leading to a stronger phonon anomaly than in the bulk. As mentioned previously, the presence of a surface enhances the orthorhombicity, which promotes both spin ordering and spin-orbit coupling. Therefore, there is a surface-enhanced magnetoelastic interaction in the LT phase, leading to the higher structural/magnetic transition temperature at the surface (T^S=65 K for x=0.05 and 150 K for x=0).

STM measurements have shown the existence of orthorhombicity beyond the superconducting regime where the bulk is always tetragonal. Shown in Fig. 3.10 is the comparison of surface tetragonal and orthorhombic lattice. The tetragonal surface lattice indicated by the black square changes from a square shape into a diamond shape. The new unit cell is defined by the blue square has the rectangle shape. The orthorhombicity is defined by $(a - b)/(a + b)$. There are two possible reconstructions on the cleaved surface, (1×2) and $(\sqrt{2} \times \sqrt{2})$. Figure 3.11 shows the deviation (orthorhombicity) from the tetragonal unit cell measured by STM on both reconstructed surfaces.
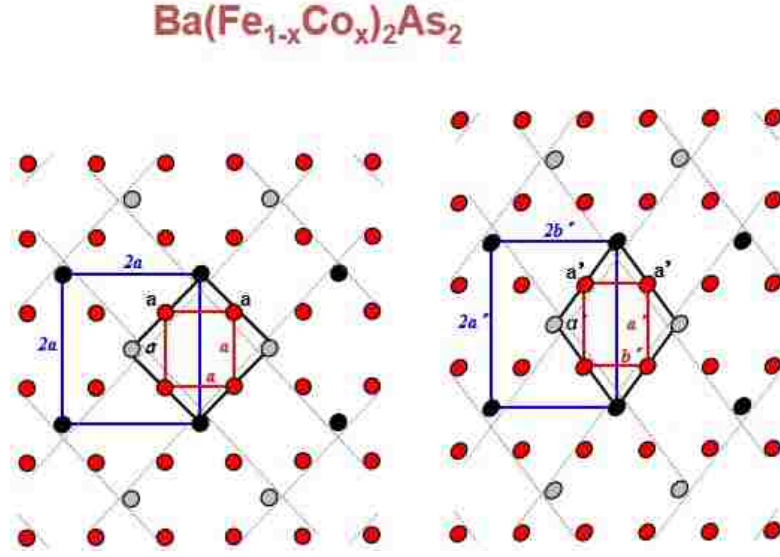
FIGURE 3.10: Comparison of surface tetragonal and orthorhombic lattice. Figure is adapted from [18].

Fig. 3.11(a) is the sketched bulk phase diagram. Figure 3.11(b) is the orthorhombicity measured on both surfaces, measure at liquid helium temperature. It is non-zero at all doping levels for both (1×2) and $(\sqrt{2} \times \sqrt{2})$ surfaces, even when the bulk is tetragonal and conducting. Figure 3.11(c) is the measured angle at the corresponding doping levels. Again it shows non-90° values for all measured samples. These results indicate the surface always enhances the orthorhombicity.

The obvious question is why the surface induces gigantic changes in lattice dynamics for $Ba(Fe_{1-x}Co_x)_2As_2$. The first clue comes from a neutron scattering study of the effect of uniaxial pressure on the coupled structural/magnetic-phase transition in $BaFe_2As_2$[111]. The application of a critical pressure of 0.7 MPa, beyond the pressure needed to detwin the sample, dramatically increases the structural transition temperature (147 K) accompanied by the onset of long-range magnetic ordering at the same temperature. As shown above, the surface transition temperature for $BaFe_2As_2$ is very close to the temperature observed by the application of a uniaxial pressure. Although it is difficult experimentally to quantify the in-
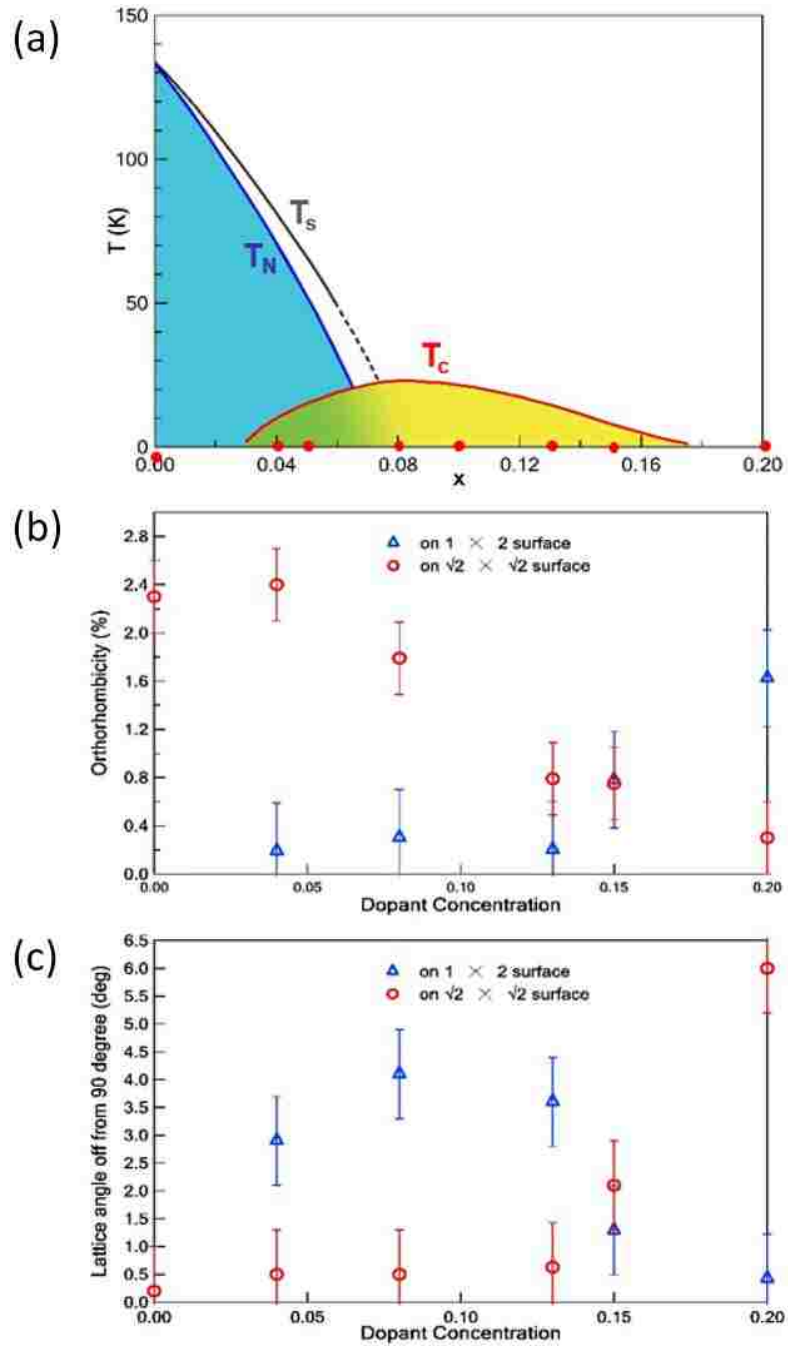
FIGURE 3.11: Orthorhombicity and lattice angle off from 90° measured by STM. Figure is adapted from [18].

duced strain along all directions by creating the surface, the observation of surface-enhanced orthorhombicity suggests that the surface behaves similarly to the bulk sample under uniaxial pressure, increasing the structural transition temperature concomitant with long-range magnetic ordering, both with second-order-like characteristics [111]. The second clue is the dramatic 10-fold increase in the line width in the HT phase at 300 K for the A_{1g} mode (column 8 in Table 3.1). This observation is a clear indication that the spin-lattice coupling through incoherent spin fluctuations is an order of magnitude higher at the surface, dramatically decreasing the lifetime of the mode. To illustrate this behavior, Figure 3.8(b) shows the line width measured for the A_{1g} mode in the bulk [1] normalized to the surface line width at 300 K (Table 3.1). If, by the application of a uniaxial pressure in the bulk, the spin-lattice coupling could be increased to what it is at the surface, the bulk would look like the surface. The final observation is that the presence of the enhanced orthorhombicity at the surface stiffens the LT modes appreciably. An extrapolation of the energy of the surface A_{1g} mode to T=0 K for the parent compound gives $\hbar\omega_{1g}$ (T=0 K)= 36.7 meV compared with the bulk energy of 22.44 meV. Everything that we observe can be rationalized with increased spin-lattice coupling, coherent in the LT phase. The differences in the doped sample must again reflect a decrease in the spin-lattice coupling at the surface because of Co doping. For example, $\hbar\omega_{1g}$ (T=0 K)= 33.0 meV is lower for x=0.05, and its line width at 300 K is only 46% of the linewidth of the parent compound.

In conclusion, cleaving a single crystal to create a surface breaks the translational symmetry and thus, disturbs the delicate balance between structure and magnetism, which may result in completely new emergent behavior. EELS results reveal dramatic temperature dependence both in the energy and width of the two dipole-active modes A_{1g} and A_{2u} in the LT phase of both the parent and Co doped

$BaFe_2As_2$. This behavior is in contrast to the behavior of these phonon modes in the HT phase, which is nearly identical to the bulk and can be explained within a simple anharmonic potential model. The surface transition temperature T^S is higher than in the bulk, most likely driven by the strain induced by creating a surface. A hypothetical surface phase diagram for the Co doped Ba122 system, based on HREELS data presented here combined with STM [135], is displayed in Figure 3.9. STM studies have shown that the surface stabilizes and enhances the orthorhombic structure throughout the whole range of doping relevant to superconductivity, while maintaining a superconducting gap characteristic of the bulk [135]. We report the temperature dependence of two phonon modes for two compositions of $Ba(Fe_{1-x}Co_x)_2As_2$ with $x = 0$ and $x = 0.05$. As summarized in Figure 3.9, the observed surface transition temperature is appreciably higher than in the bulk, and the temperature dependence of the vibrational modes in the LT phase is dramatically different from in the bulk. An example is shown in Figure 3.9 inset, where the energy of the A_{1g} mode for the compound with $x = 0$ is displayed as a function of temperature, and should be compared with Figure 3.1 inset for the bulk mode. The surface surely has tipped the balance between the competing phases. These features mirror the bulk properties under uniaxial stress [111]. Hence, our surface measurements resolve the question of the origin of the increase in magnetic ordering in the bulk under the application of a uniaxial pressure. It is a consequence of strong spin-lattice coupling in this system.

Chapter 4

Surface Structure-Property Coupling of $Sr_3(Ru_{1-x}Mn_x)_2O_7$

4.1 Introduction
4.1.1 Bulk Phase of Parent $Sr_3Ru_2O_7$

A more detailed review of $Sr_3(Ru_{1-x}Mn_x)_2O_7$ bulk properties is introduced in section 1.7.2. These observations are briefly summarized here. The parent $Sr_3Ru_2O_7$ shows metamagnetic quantum critical endpoint under magnetic field [73, 74, 20]. Under pressure it shows FM order, with expansion of the outer apical Ru-O bond and slight change in rotation angle [136, 21]. The magnetization is greatly enhanced under pressure at low temperature [21], indicating FM instability in its ground state. With Mn doping a MIT has been reported for the bulk [22, 68]. Starting from $x \sim 0.05$, the resistivity has an upturn towards zero temperature, with a decrease in the spectral weight between 0.07 - 0.24 eV at low temperatures measured by optical conductivity, implying a reduce in density of states near the Fermi energy [22]. In addition, as the percentage of Mn increases the transition temperature T_{MIT} increases associated with the decrease of octahedral rotation. An AFM order also emerges starting from $x = 0.05$ [82]. The bulk phase diagram is shown in Fig. 4.1.

4.1.2 Surface Phase Study of Mn doped $Sr_3Ru_2O_7$

Early stage study shows that there is lattice tilt distortion on the surface. LEED pattern has shown broken glideline symmetry at both room temperature and low temperature [87]. This broken glideline lowers the LEED pattern symmetry than C_{4v} for a surface with rotation only. Detailed calculation shows that the tilt angle is $4.5 \pm 2.5°$ at 300 K and $2.5 \pm 1.7°$ at 80 K, both with enhanced octahedral rotation around $\sim 12°$.
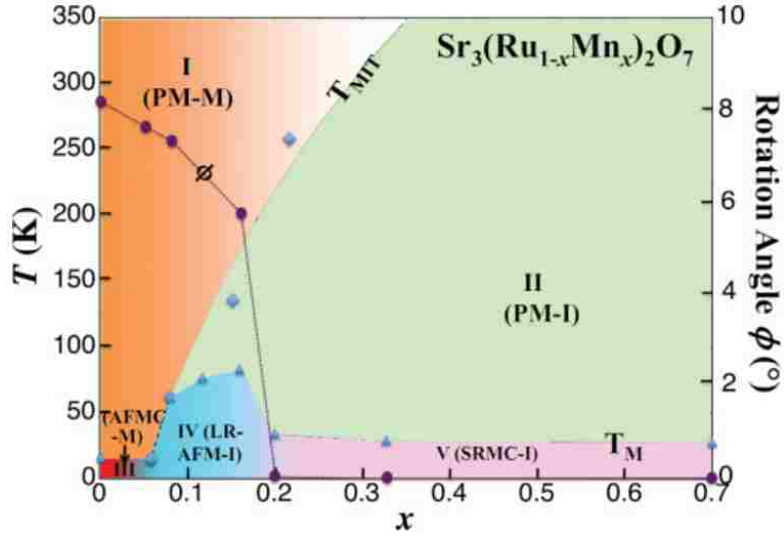
FIGURE 4.1: Bulk phase diagram of $Sr_3(Ru_{1-x}Mn_x)_2O_7$ ($0 \leqslant x \leqslant 0.7$). Diamonds and triangles represent T_{MIT} and T_M, respectively. Region I is a paramagnetic metallic (PM-M) phase. Region II is a paramagnetic insulating (PM-I) phase. Region III is a metallic phase with AFM correlation (AFMC-M). Region IV represents a long-range AFM insulating phase (LR-AFM-I). Region V is an insulating phase with short-range magnetic correlation (SRMC-I). The right axis indicates the x dependence of the rotation angle ϕ of the $(Ru/Mn)O_6$ octahedron at 90 K. Figure is adapted from [68].
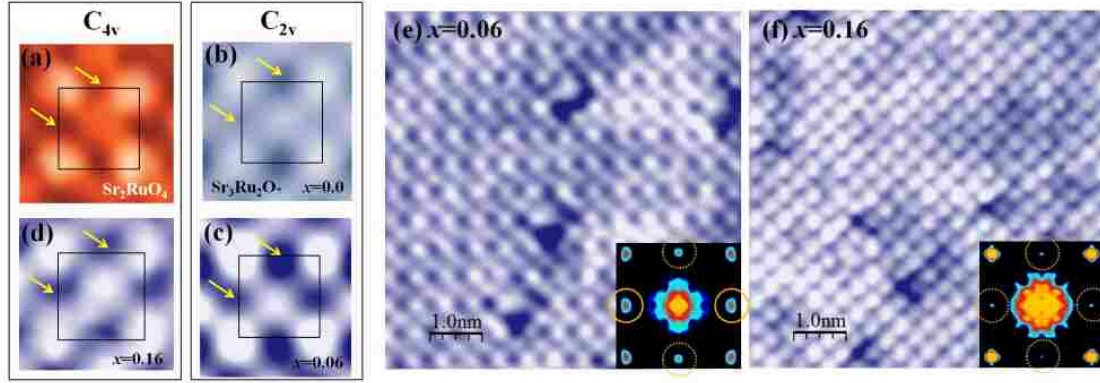
FIGURE 4.2: STM images with indicated symmetries for different doped surfaces. (a) Sr_2RuO_4 at a bias of 0.75 V at 300 K, reproduced from [47], (b) $Sr_3Ru_2O_7$ ($x=0$) at a bias of 7 mV at 0.56 K, reproduced from [86], (c) $x=0.06$, for 0.9 V at 100 K, and (d) $x=0.16$, at 0.6 V and 100 K. (e and f) 7.0 nm $\times$ 7.0 nm STM topography taken at 0.9 V (100 K) for $x=0.06$ and at 0.6 V (100 K) for $x=0.16$. The insets are corresponding FFT images. The circled FFT spots are corresponding to fractional order spots from $(\sqrt{2}\times\sqrt{2})R45°$ structure. Note that the yellow dotted-line circled spots are less intense than solid-line circled ones for x=0.06, indicating a broken symmetry. Figure is adapted from [19].

STM experiments on $Sr_3(Ru_{1-x}Mn_x)_2O_7$ have seen this broken symmetry shown in Fig. 4.2 [19]. Figure 4.2(a) is the surface for Sr_2RuO_4 from [47] and (b) is the surface for $Sr_3Ru_2O_7$ from [86]. In Fig. 4.2(b) there are two kinds of hollow sites presented by arrows, but the two sites in (a) are similar, This indicates the STM image of $Sr_3Ru_2O_7$ has C_{2v} symmetry, which is consistent with a surface with octahedral tilt. Figure 4.2(c) and (d) are the two STM images from $x = 0.06$ and 0.16, respectively. In Fig. 4.2(c) the hollow sites still have distinct contrast although the difference is reduced. In Fig. 4.2(d) the image looks more like the Sr_2RuO_4 surface. The fast Fourier transform (FFT) of large-scale STM images also supports this symmetry, shown in insets of Fig. 4.2(e) and (f). The fractional spots indicated by the yellow dotted lines are less intense than the spots circled by the solid lines for $x = 0.06$, while they are almost the same for $x = 0.16$.

The relationship between tilt distortion and surface metallicity was also studied by STM. Figure 4.3(a) and (b) are the STM topographic images. There are different
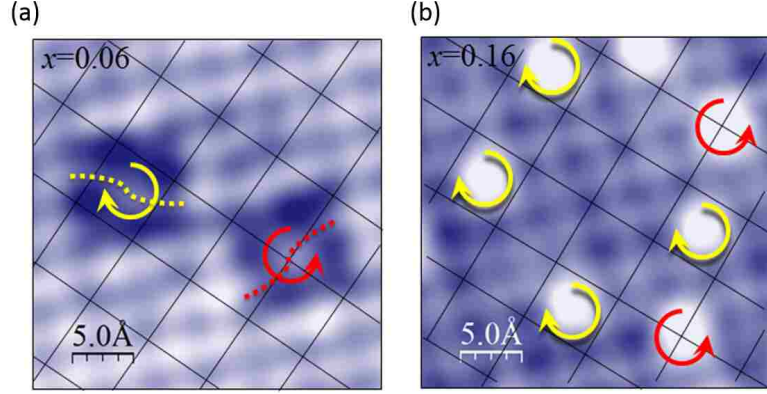
FIGURE 4.3: (a) STM topographic image of $x = 0.06$ compound with the orthorhombic lattice grid (black solid lines). (b) STM topographic image of $x = 0.16$ compound with the lattice grid. The different chirality of the Mn sites is indicated by red and yellow arrows. Figure is adapted from [19].

rotating directions for the octahedral rotation, clockwise and counter-clockwise. Since Mn dopants locate at the center of each octahedron, there are two chiralities around the Mn dopants. The electronic disturbance near the Mn dopants for two doping levels $x = 0.06$ and 0.16 are shown in Fig. 4.3 [19]. Between Fig. 4.3(a) and (b) there are different sizes of the disturbance in the LDOS surrounding a Mn impurity. The disturbance size is related to the magnitude of the tilt at the surface through electronic screening, i.e. more tilt leads to less screening. With reduced screening at lower doping, the chirality easily resolved. In contrast to the bulk properties shown in Fig. 4.1 the surface is less conducting at 80K for $x = 0.06$ than $x = 0.16$. The surface seems to be conducting at $x = 0.16$ while the bulk is an insulator. Considering the structural difference, the surface conductivity is strongly coupled to the surface tilt.

The above example indicates the broken symmetry at the surface disturbs the balance between the structural, electronic, and magnetic degrees of freedom, offering the possibility for new properties to emerge. The layered nature of $Sr_3(Ru_{1-x}Mn_x)_2O_7$ is suitable for cleaving, thus offering an opportunity to study the structure-property

relationship under a unique environment. However, how to understand this new phase and to establish its unusual structural-property relationship remains a challenge.

In this study, combination of surface techniques are utilized to probe the surface structure and metallicity. LEED I-V analysis is used to probe the surface rotational and tilt distortion. Density functional theory (DFT) calculation is used to examine the stability of tilt distortion in a single $Sr_3Ru_2O_7$ perovskite bilayer. HREELS is used to explore the surface electron-phonon coupling for the surface metallicity as a function of Mn doping. With the combined results from these tools, it is confirmed that (1) there exists a surface tilt distortion with possibly different rotation schemes than the bulk, and (2) the doping dependence of conductivity of the surface and the bulk are fundamentally different because the structure is different.

4.2   LEED I-V Analysis of Parent $Sr_3Ru_2O_7$
4.2.1   Stucture Buildup and Coordinates Input

The first step of a LEED I-V calculation is to generate the input files for different structures to be explored. In the case of $Sr_3Ru_2O_7$, the conjectured structures are based on the bulk tetragonal unit cell, shown in Fig. 4.4(a). There are double octahedra stacking along c direction, with the Ru atom located at the center of each octahedron. For the parent compound there is octahedra rotational distortion, with the octahedra in the two planes rotating in opposite directions around c-axis, shown in Fig. 4.4(b) [71].

The unit cell with octahedral rotation is orthorhombic. The top view of this structure is shown in Fig. 4.5. If the tetragonal unit cell is defined as the (1×1) cell, the bulk truncated surface is a $(\sqrt{2} \times \sqrt{2})R45°$ unit cell. The LEED I-V calculation uses the enlarged unit cell, so all the spots on the LEED pattern can be labeled as integer numbers.
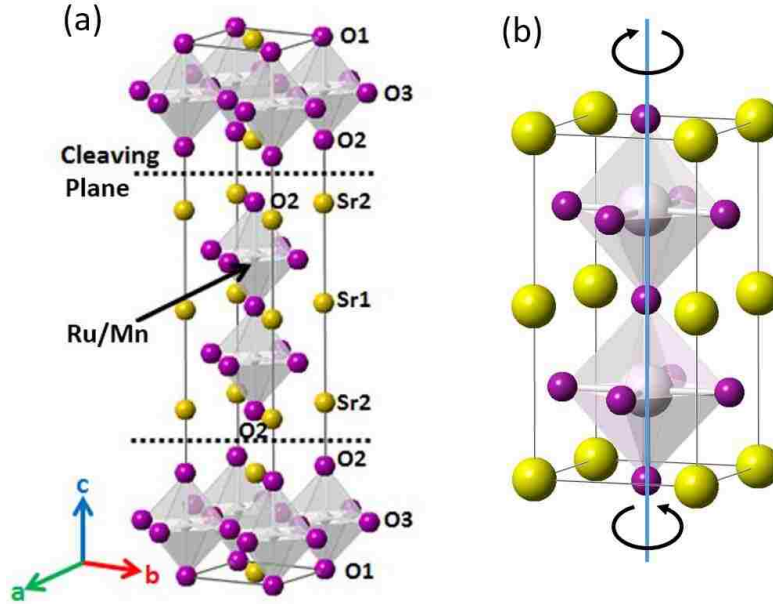
FIGURE 4.4: (a) Tetragonal (tet) unit-cell structure of $Sr_3Ru_2O_7$. The Ru atoms are located in the center of each octahedron. The cleaving plane is indicated by the dashed line, which results in a SrO surface layer. (b) Bulk structure of the double layered ocatahedra. The top and bottom octahedra are rotating in opposite directions.
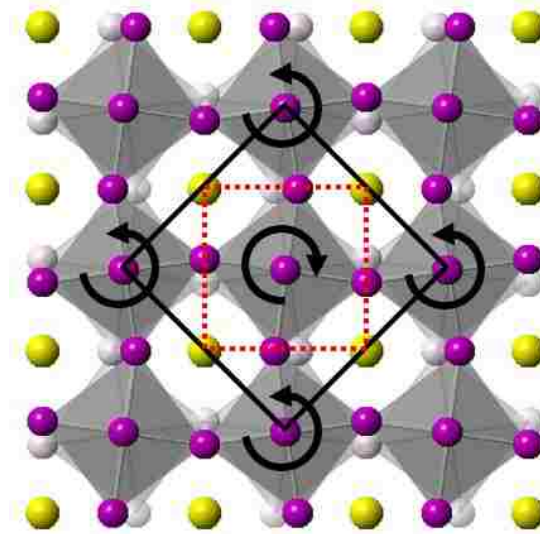
FIGURE 4.5: Rotation of the RO_6 octahedra layer from top view of the surface plane, indicated by black arrows. The top and bottom octahedra are indicated by dark and light grey color respectively. The black square is bulk truncated ($\sqrt{2} \times \sqrt{2})R45°$ unit cell, while the red dashed square is the tet-(1×1) unit cell with no rotational distortion.

When tilt is introduced into the system, which is the case on the surface, the size of the unit cell does not change. Therefore there are no extra fractional spots on the LEED pattern. With tilt the octahedra rotate out of plane around an axis parallel to the octahedral edge. The top and bottom octahedra rotate in opposite directions because they share one oxygen atom. The labels of atoms are shown in Fig. 4.4(a). The tilt angle can be defined in two separate ways: one is between the O3 plane and the ab-plane (θ_{plane}), and the other is between the Ru-O2 bond and the c-axis (θ_{top}). The double octahedra with tilt is shown in Fig. 4.6.

The octahedral rotation will shift the xy coordinates of the in plane O3 atoms. The octahedral tilt will change the coordinates of all the O atoms. The connecting O1 atom and the apical O2 atoms mainly shift in plane, and the O3 atoms mainly shift along c-axis. The lattice constant in this calculation is chosen to be a=b=5.4752Å, and c=20.7980Å, based on the low temperature measurements from reference [87, 85].

With such structure, the atomic coordinates are calculated based on the following procedures:

(1) The rotational angle is ϕ, and the tilt angle is θ. Considering the difference of the plane and top tilt, it can be estimated through θ_{plane} and θ_{top} respectively. The atomic shift of the plane O atoms due to the rotation can be estimated by $\Delta x = \tan(\phi)/4$, where Δx is in the unit of length of the unit cell along the ab-axis. Similarly the shift due to the tilt can be estimated by the c-axis shift of the plane O3 atoms, $\Delta h = \tan(\theta)/10$, in the unit of length of the unit cell along the c-axis. Note that θ_{plane} and θ_{top} can be applied here for calculating plane and top tilt separately, resulting in Δh_{plane} and Δh_{top}. Furthermore, the estimation of the coordinates shift of the O1 and O2 atoms is $\Delta t_x = \Delta h \times 3.8$, and $\Delta t_y = \Delta t_x \times \tan(\phi)$.
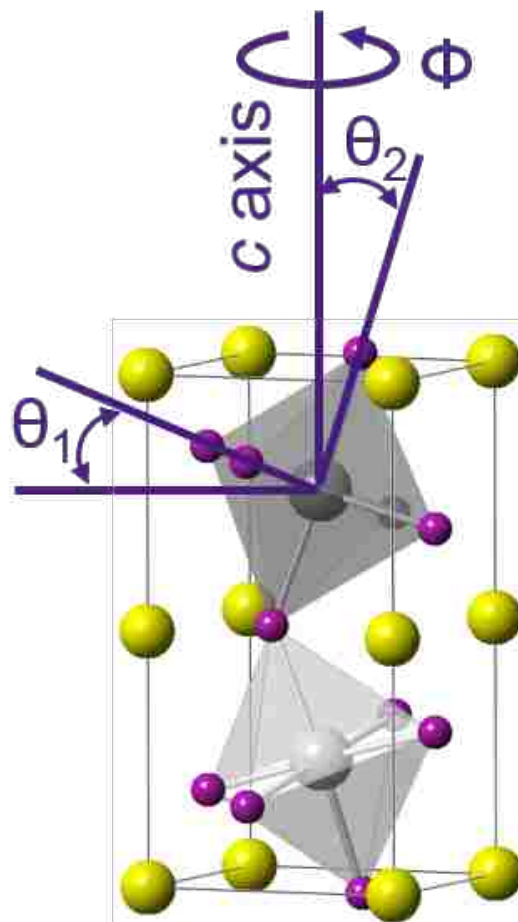
FIGURE 4.6: Schematic view of tilt distortion of the double-layer octahedra with the surface tilt angle (θ) defined by either the angle between the xy plane and the plane that contains the four O3 atoms (θ_1), or the angle between the Ru-Top O2 bond and c axis (θ_2).

(2) Now consider one double-layered octahedra layer with both rotation and tilt, there are 24 atoms in one unit cell. The coordinates of these atoms in the unit of lattice parameters are shown in Table 4.1. Based on the formula in this table, the coordinates in $\mathring{A}$ can then be calculated by simply multiplying the calculated numbers by the lattice parameters. The numbers in unit of $\mathring{A}$ can be used for LEED I-V input file "tleed5.i".

TABLE 4.1: Coordinates for the 24 atoms in a unit cell of a double-layered octahedra. The unit is lattice parameter.

Atomic No.	Label	x (5.4752Å)	y (5.4752Å)	z (20.7980Å)
1	Sr2	0	0	0
2	Sr2	0.5	0.5	0
3	O1	$-\Delta t_x$	$0.5-\Delta t_y$	0.0049
4	O1	$0.5+\Delta t_x$	$-\Delta t_y$	0.0049
5	O4	$0.25+\Delta x$	$0.25+\Delta x$	$0.2-(0.0969+\Delta h)$
6	O4	$0.25-\Delta x$	$-0.25+\Delta x$	$0.2-(0.0969+\Delta h)$
7	Ru	0	0.5	0.1022
8	Ru	0.5	0	0.1022
9	O3	$-0.25+\Delta x$	$0.25-\Delta x$	$0.2-(0.0969-\Delta h)$
10	O3	$0.75-\Delta x$	$0.75-\Delta x$	$0.2-(0.0969-\Delta h)$
11	O2	Δt_x	$0.5+\Delta t_y$	0.2
12	O2	$0.5-\Delta t_x$	Δt_y	0.2
13	Sr1	0	0	0.2
14	Sr1	0.5	0.5	0.2
15	O3	$x(10)$	$y(10)$	$0.4-z(10)$
16	O3	$x(9)$	$y(9)$	$0.4-z(9)$
17	Ru	$x(8)$	$y(8)$	$0.4-z(8)$
18	Ru	$x(7)$	$y(7)$	$0.4-z(7)$
19	O4	$x(6)$	$y(6)$	$0.4-z(6)$
20	O4	$x(5)$	$y(5)$	$0.4-z(5)$
21	O1	$x(4)$	$y(4)$	$0.4-z(4)$
22	O1	$x(3)$	$y(3)$	$0.4-z(3)$
23	Sr2	$x(2)$	$y(2)$	$0.4-z(2)$
24	Sr2	$x(1)$	$y(1)$	$0.4-z(1)$

One thing worth noting here is that the current calculation assumes that the top and bottom octahedron in one unit cell is rotating along the same direction, which is different from the bulk. The effect from such difference will be discussed later. However there is slight difference between the two rotation schemes on the calculation of coordinates: (1) The x and y coordinates of the bottom octahedron are the same with the top one if they rotate in the same direction. If they are rotating in opposite directions just like bulk, the bottom coordinates can be calculated based on the inversion symmetry from their original positions without rotation and tilt. For example, if the top atom shifts along positive (negative) x direction, the bottom corresponding atom would shift along negative (positive) direction. (2) If they are rotating in opposite schemes, based on the symmetry Δt_y would always be zero. In such case there is inevitable octahedral distortion.

4.2.2   Phase Shift Calculation with Optimized Muffin-Tin Model

The phase shift calculated here uses optimized muffin-tin (OMT) potential proposed and developed by Rundgren *et. al.* [137]. The structure input assumes the bulk structure with the octahedral rotation only. A complete unit contains two double-layered octahedra, so there are 20 bulk layers in the input. Here a "bulk layer" is defined as either a SrO layer, or a RuO_2 layer. There are 6 inequivalent atomic species in the bulk, which are Sr1, Sr2, Ru, O1, O2, O3/4, corresponding to the atomic labels in Table 4.1.

Compared to the traditional phase shift calculations obtained from the atomic charge density, there are two main advantages of this OMT method: (1) The phase shifts are smoothier. This is because the conventional method has muffin-tin (MT) radii not continuous, presenting steps. The phase shifts calculated at these discontinuous distances will have quasi-standing waves and resonance behavior. This can lead to inaccuracies in the following LEED I-V calculation. In
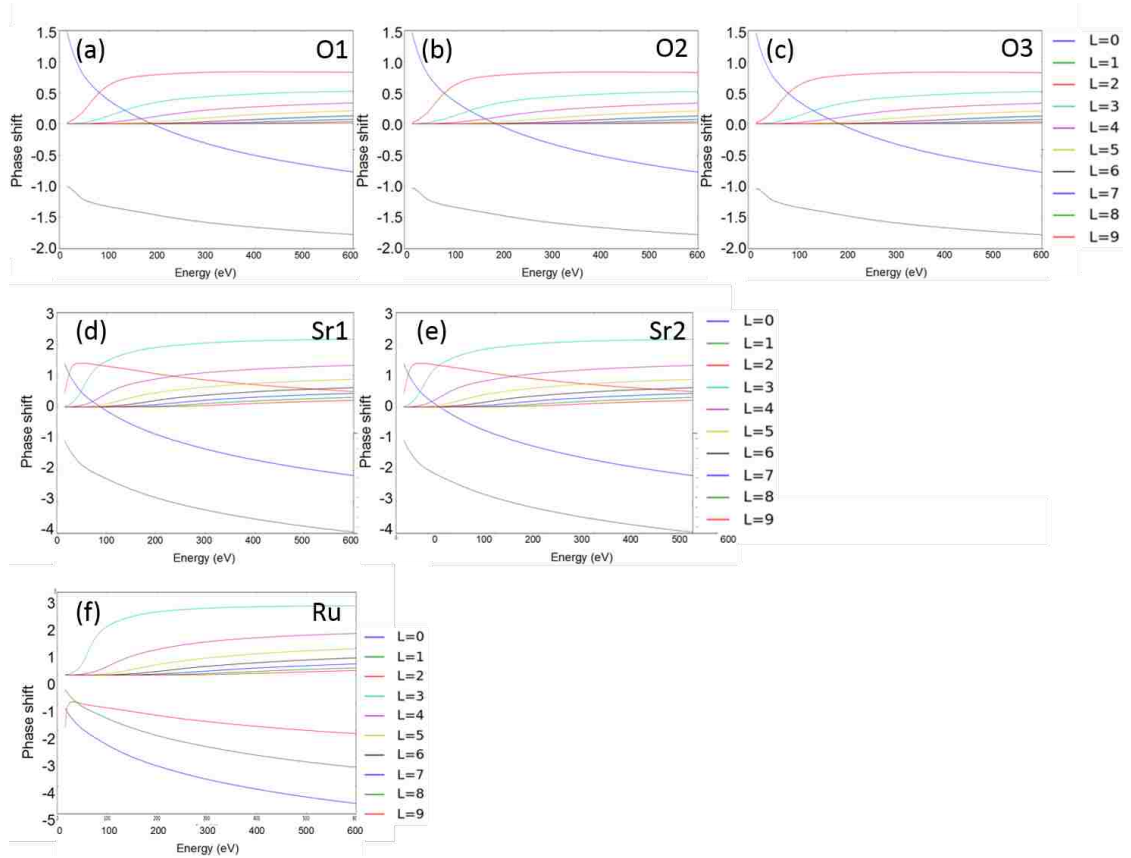
FIGURE 4.7: Calculated phase shifts of the 6 inequivalent atoms. The same atomic species are presented in one row. There is little difference in phase shifts within the same species.

other words, a smooth, non-oscillating energy dependent phase shift is considered ideal. (2) In the OMT method, the inner potential is considered energy dependent. $V_o = V_o(E) = V_{or}(E) + iV_{oi}(E)$. This inner potential has been proven to be very useful when calculating the complex oxides surfaces [138]. Only when including this part the octahedral rotation and tilt angles are at reasonable range with a best R_P value.

The calculated phase shifts using the OMT method for the 6 atoms are shown in Fig. 4.7. They are used for the input file "tleed5.i". It can be seen from here that the different chemical environment of the atoms of the same species (O and Sr) does not change the phase shift very much.
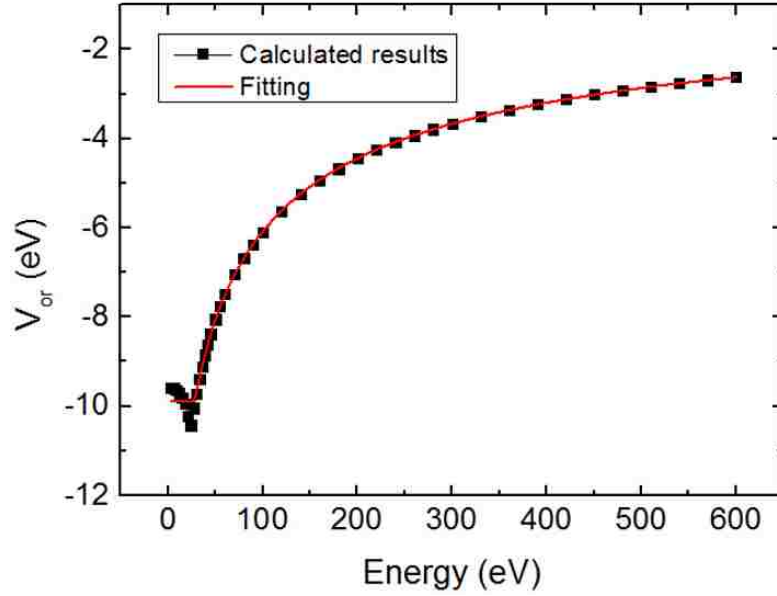
FIGURE 4.8: Energy dependent inner potential. Black dots: calculated value. Red line: fitting value.

Meanwhile the energy dependence of the real part of inner potential is also calculated, shown in Fig. 4.8. This inner potential is fitted with equation 2.4. The calculation gives the cut-off energy: E_c=16, const=-9.89, A_0=0.02, A_1=-65.48, and A_2=15.49. These numbers are applied in a separate subroutine to calculate the modified electron beam energy, and the results are then passed to the main calculating program "tleed1".

4.2.3 LEED I-V Calculation Based on Simulated Annealing Algorithm

The simulated annealing (SA) is implemented into the conventional LEED I-V searching method for two purposes: (1) SA is a better method for global minimum optimization. (2) The conventional searching method does not respect the glideline symmetry, which is the only symmetry that leftover when the octahedra have rotation and tilt. If the conventional searching is adapted, with no constraint in symmetry, the coordinates will relax in a completely free behavior. This will lead to unreasonable results, although the R_P factor obtained could be smaller.

In the current calculation, the atoms are allowed to relax under the constraint of the glideline symmetry. In order to achieve this, the corresponding atoms have to shift the same distance but in opposite directions along x direction, while exactly the same direction along y and z directions. Here the term "corresponding atoms" means that the atoms in a unit cell that coincide with each other under the glide symmetry operation. For example, in a unit cell, the two Sr2 atoms (atomic No. 1 and 2 in Table 4.1) on top are considered the corresponding atoms. During the calculation, if one Sr2 atom moves Δx, Δy and Δz in its three coordinates, the other Sr2 atom must move $-\Delta x$, Δy and Δz in its coordinates.

The SA algorithm used here is the "scipy.optimize.anneal" package written in Python. The objective function that needs to be optimized is defined by the R_P factor as a function of the atomic coordinates. To take full advantage of the calculation speed of the tensor-LEED method, the objective function is constructed as following: (1) There is a starting structure with certain rotation and tilt angles but no other lattice distortions. This starting structure is used in file "tleed5.i" for the 1st step calculation "tleed1", and the file that contains the tensor information, "short.t", is obtained. (2) The atoms start to relax by a random number determined by SA package under the glideline constraint, and the deviation from the starting structure is thus calculated. This deviation in coordinates is then used to generate the "tleed4.i" file, which is then used for the 2nd step calculation "tleed2". (3) Once the second step is finished, the R_P value can be read from the file "search.s", and serves as the corresponding value of the objective function at the deviated structure.

4.2.4 Rotation and Tilt Angles Determined by LEED I-V Calculation

For the convenience of the LEED I-V structure input and calculation, the unit cell here is defined by the larger orthorhombic unit cell. Thus all the spots on the

LEED pattern can be labeled by integer numbers. The equivalency of spots defined in such a way can be easily recognized.

Prior to calculation the LEED I-V data is smoothed using Savitzky-Golay method with polynomial order of 3. Each I-V curve is averaged among at most 4 corresponding spots depending on (1) they are affected by the gun or (2) they are along the axis such as (1,0) and (3,0). For example, (1,2) is averaged among (1,2), (1,-2), (-1,2), and (-1,-2), whichever is not affect by the LEED gun.

It should be mentioned that in principle they are not symmetry equivalent spots because the surface unit cell loses all the symmetry except for a glide plane. The 2D space group of the surface lattice is *pg*. This structure will cause the LEED pattern having only one reflection symmetry with respect to the y-axis. With this symmetry the (1,2) and (-1,2) are considered symmetry equivalent spots, as well as (1,-2), and (-1,-2).

However, due to the existence of domains the I-V curve of each spot contains I-V information from other spots. In addition, averaging the spots can help reduce the noise level, which is beneficial because the signal to noise (S/N) level from the orthorhombic unit cell (fractional) spots is much worse than from tetragonal unit cell (integer) spots. Without such averaging the R_P factor is always bigger than 0.3 due to the large noise from the data. With averaging the energy range is smaller thus the estimated error is larger, but the final R_P is acceptable.

The experimental and calculated LEED I-V curves are presented in Fig. 4.10. The fitting procedure adapts a SA searching algorithm. The fitting parameters are the x, y and z coordinates of all atoms in a unit cell with rotation and tilt distortions of the octahedra. Here the two tilt angles (plane and top) are assumed to be equal to each other. All the movements are under the constraint of glideline symmetry.
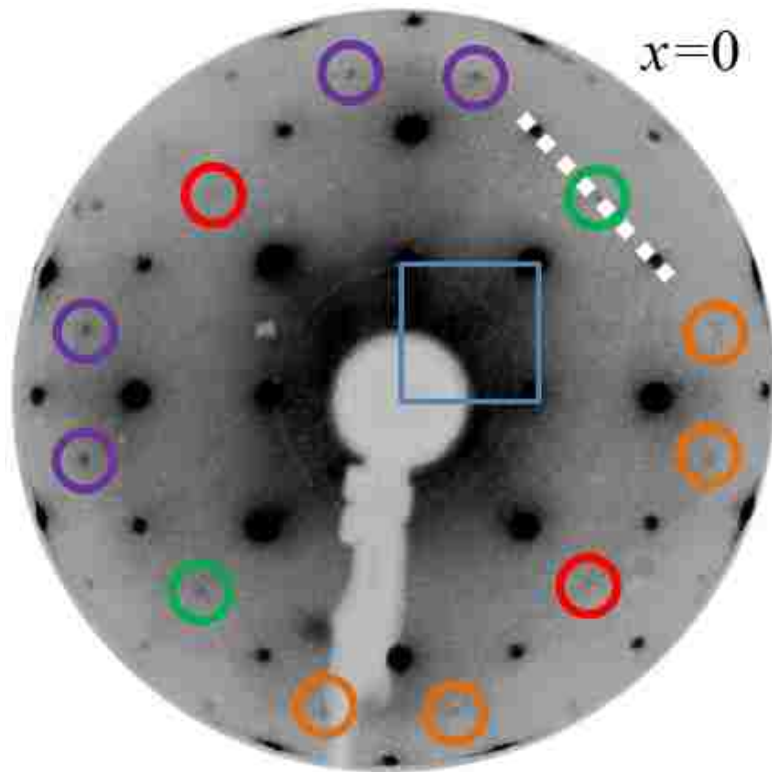
FIGURE 4.9: LEED pattern of $Sr_3Ru_2O_7$ at 86K. The reciprocal lattice from the orthorhombic unit cell is indicated by the blue square. The dashed line crosses the (3,1), (3,0), (3,-1) spots of the pattern. The green circles show the locations of the two diffracted spots along the broken glideline, and the red circles show the locations of the two extinguished spots along the reserved glideline. The yellow and orange circles indicate the locations of the spots with different intensities (yellow for large intensities and orange for small intensities).
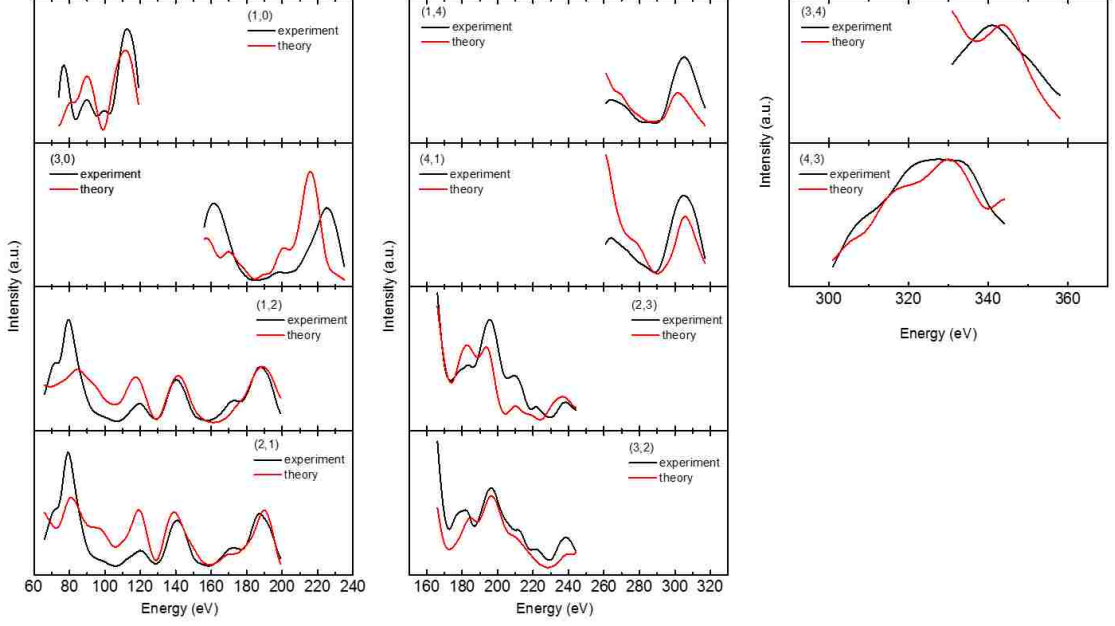
FIGURE 4.10: Experimental data and calculated LEED I-V curves for the optimized structure with minimum R_P factor.

The experimental data used here are solely from the spots due to the larger unit cell. The reason for this is that these spots are sensitive to the rotation and tilt of the octahedra. The total energy range is 759 eV with a minimum R_P=0.28. The associated error in the structural parameters is estimated with the equation $\sigma = (R_P^{Total})_{min}\sqrt{\frac{8|V_{oi}|}{\Delta E}}$ proposed by Pendry in [99], where ΔE is the energy range, and V_{oi} is set at 6 eV here, which is a relatively large value. With the total R_P factor of 0.28, the estimated error is $\sim$0.07.

Fig. 4.11 shows the rotation and tilt angle dependence of R_P values deviated from the optimum solution (10.5° for rotation and 2.6° for tilt). From the cut of the maximum allowed R_P value (0.35) with the two curves, the error of rotation and tilt angles can be estimated, yielding 10.5±3.0° for rotation and 2.6±0.8° for tilt. These numbers are consistent with reference [87] (12±3° for rotation and 2.5±1.7° for tilt). The smaller error in tilt value is because only the fractional beams are used in the current calculation. In addition, due to the low sensitivity of atom's

in-plane movement of LEED I-V analysis, the error of the rotation angle is much larger than tilt.
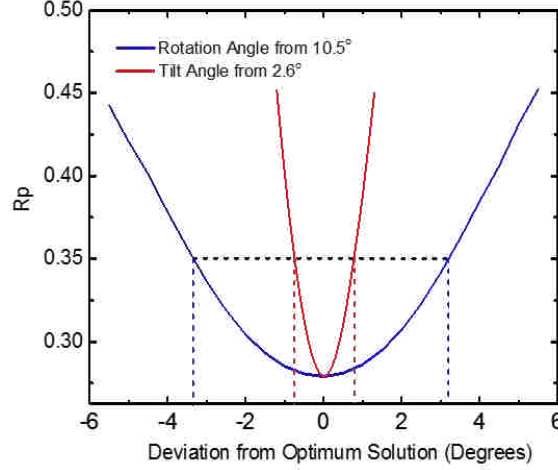
FIGURE 4.11: The R_P factor at angles deviated from the optimum solution, blue for rotation angle and red for tilt angle, respectively. The values for rotation and tilt angle at optimum solution are $10.5°$ and $2.6°$, respectively, where the two different tilt angles are fixed at the same value ($\theta_1=\theta_2=\theta$). The error of the corresponding parameters can be estimated from the values where the black dashed line crosses the blue and red curves.

4.2.5 Tilt Angles Determined by LEED I-V Broken Symmetry Simulation

There is further broken symmetry on the LEED pattern which has never been discussed before. Shown in Fig. 4.9 is the LEED pattern of parent $Sr_3Ru_2O_7$ at 86K. On one side the fractional spots indicated by the purple circles have higher intensities than the other side where the corresponding spots are indicated by the orange circles. This is such delicate intensity difference that cannot be differentiated from integer spots analysis, however detailed I-V analysis from averaged corresponding spots can. Shown in Fig. 4.12(a) for $x=0$ sample (unsmoothed), the two I-V curves clearly possess different shapes, and at the beam energy $\sim$225eV there is a peak for the curve averaged from the four existing spots while the other curve does not.
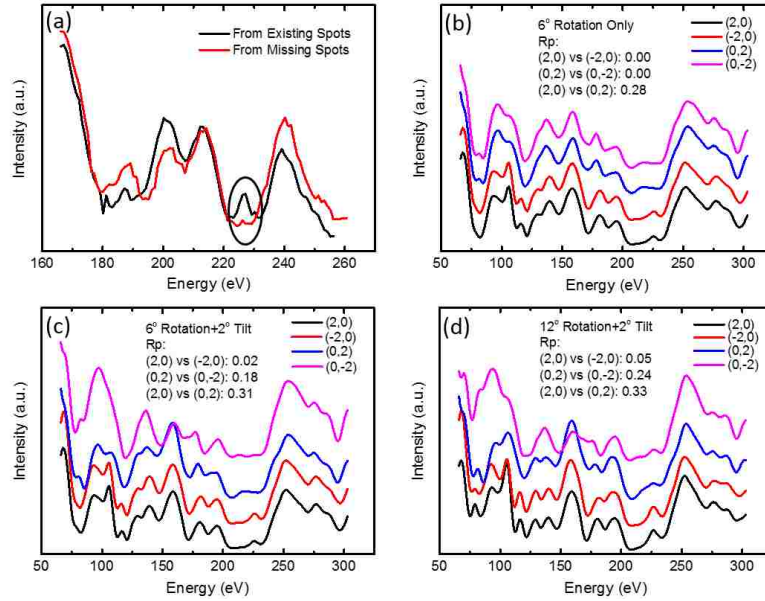
FIGURE 4.12: (a) LEED I-V curve averaged from four existing spots (2,3), (3,2), (-2,3), (-3,2) on one side of the broken glideline compared to the other side from four missing spots (2,-3), (3,-2), (-2,-3), (-3,-2) for x=0. The I-V data are collected from LEED pattern at different beam energies, including Fig. 4.9. The difference between two I-V curves is not large but there is a clear peak around 225eV from existing spots than the other. (b)~(d) Theoretical generated LEED I-V curves from three different structural inputs. (b) With 6° octahedral rotation only (c) With 6° rotation and 2° tilt. (d) With 12° rotation and 2° tilt.

Theoretical simulation generating LEED I-V curves confirms that the symmetry breaking behavior is due to combination of rotational and tilt distortion, regardless of the number of octahedra in the unit cell. Figure 4.12(b) (d) are theoretically generated LEED I-V curves from three different structural inputs: with 6° octahedra rotation only for Fig. 4(b), 6° rotation and 2° tilt for Fig. 4(c), and 12° rotation and 2° tilt for Fig. 4(d). Four spots (0,±2) and (±2,0) are selected because they are representative for the broken reflection symmetry examination. When there is only 6° rotational symmetry on the surface like Fig. 4(b), the R_P value between (2,0)&(-2,0) pair and (0,2)&(0,-2) pair are both zero, meaning they are exactly the same. The LEED pattern in this situation reserves two reflection symmetries perpendicular to each other. In Fig. 4(c), 2° tilt is introduced while the rotation keeps the same. By comparison there is big difference between the (0,2)&(0,-2) pair while the (2,0)&(-2,0) pair keeps a small difference. This means the reflection plane along the broken glideline direction is broken, while the other one survives, consistent with our previous argument from experimental results. When the surface rotational distortion is enhanced to 12°, the R_P value between every pair is increased, shown in Fig. 4(d). This result confirms that the enhanced rotation plays a role on breaking the surface symmetry.

Fig. 4.13 shows the experimental I-V for these beams as a function of incident electron energy at 86 K. The R_P between these two beams is 0.68. The sensitivity of LEED intensity difference as a function of tilt has been explored by conducting a theoretical simulation.

I-V curves are simulated for the lattice with 10.5° rotation and various tilt angles. BY comparing the simulated I-V curves of the purple to the orange fractional spots, the R_P value is calculated. The simulated R_P as a function of tilt angle is shown in the inset of Fig. 4.13. The experimental R_P of 0.68 translates into a tilt angle
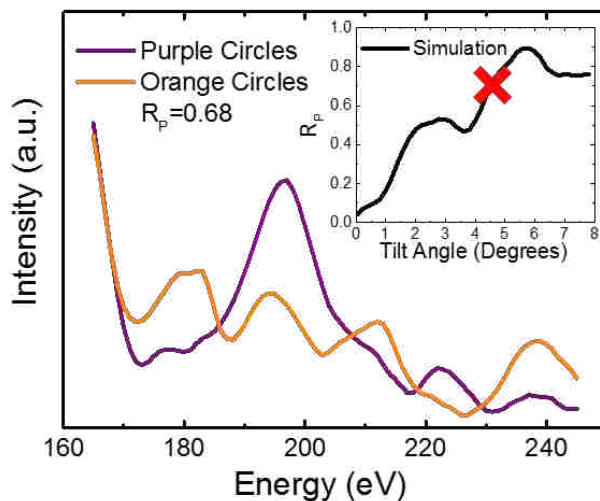
FIGURE 4.13: Comparison of averaged LEED I-V curves from the purple and orange spots shown in Fig. 4.9. (Inset) R_P values based on simulated I-V's at various tilt angles. The simulation is based on 10.5° octahedral rotation. The red cross shows the R_P=0.68 calculated from experimental I-V curves.

of 4.4°, shown by the red cross, which is appreciably larger than the value of 2.6° determined by the LEED I-V fit. It is clear why this simulation overestimates the tilt angle, it underestimates the change in R_P as the tilt angle increases because it does not allow for distortion of the octahedra.

The effect of octahedral distortion can be illustrated by calculating R_P between experiment and theory, where the tilt distortion is described by two angles (Fig. 1(f), one between the O3 plane and the ab-plane (θ_1), and the other between the Ru-O2 bond and the c-axis (θ_2). In the previous fit shown in Fig. 2(c) the two angles are constrained identical with $\theta_1=\theta_2=2.6\pm0.8°$. This unrestricted relaxation gives a slight improvement in R_P of 0.01, an increase in the in-plane angle $\theta_1=2.7$ and a decrease in the c-axis angle $\theta_1=2.3$. Because of the large error bars, difference between the two angles is not significant. This tendency of the tilt angle change is suggestive.
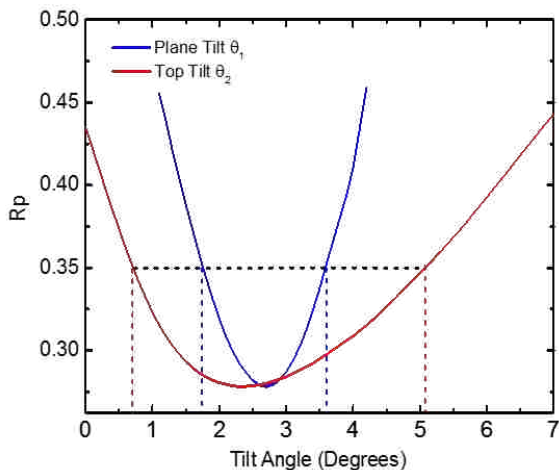
FIGURE 4.14: The R_P factor at different tilt angles where the plane tilt (θ_1) and top tilt (θ_2) in Fig. 4.6 are relaxed separately. The R_P improvement is <0.1, with final values θ_1=2.7°±1.0° and θ_2=2.3°±1.6°.

4.2.6 DFT Calculation of the Stable Structure

As described before, the octahedral tilt can be described by two different angles 4.6. In previous calculation in Fig. 4.11 these two angles are assumed to be the same with results θ_1=θ_2=2.6±0.8°. If they are set to relax independently, the new calculation has R_P improvement smaller than 0.01, with θ_1=2.7°±1.0° and θ_2=2.3°±1.6° shown in Fig. 4.14. The reason for a larger θ_2 error is that tilt of O2 oxygen off the c-axis is mainly in-plane movement. This result indicates that current LEED I-V calculation can hardly resolve the octahedra distortion because the difference between two tilt angles is smaller than the error.

Furthermore, there are actually two possible octahedra rotation schemes for the surface of this compound with the existence of tilt. In the bulk the top and bottom octahedra rotate in opposite directions. With this scheme on the surface they simply tilt in opposite directions without changing the rotational direction of the bottom octahedron. In another scheme these two octahedra can rotate in the same
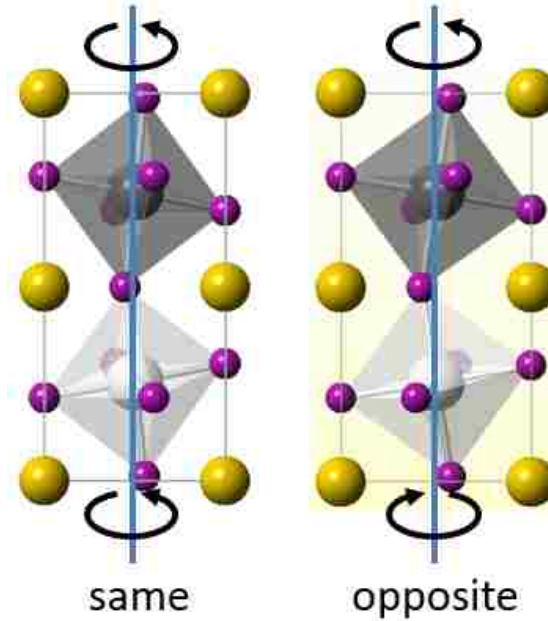
FIGURE 4.15: Schematic view of the double layered octahedra with two different rotation schemes. One has both top and bottom octahedra rotating along the same direction, with the other one along the opposite direction.

direction, while the tilt is still in opposite directions. These two schemes are shown in Fig. 4.15. The opposite rotation scheme might be understood intuitively since it follows the bulk, but the same rotation scheme cannot be completely ruled out. Previous study shows when Ca is doped into the system and tilt is introduced in the bulk, the two octahedra actually rotate in the same direction [85, 139]. Unfortunately because of the surface sensitivity of LEED, the current I-V calculation, although based on the same rotation scheme, cannot decide the bottom octahedral rotational direction.

However, our DFT results provide support to the same rotation scheme. In Fig. 4.16(a), we show the energy dependence on the in-plane lattice constant for four different structures. The total energies are calculated for the single $Sr_3Ru_2O_7$ bilayer, which includes four octahedra, and the energy of the structure with opposite rotation and without tilt is set to 0. Those structures initiated with tilt are consider to have no tilt, and therefore are not displayed in the two tilt curves, if the
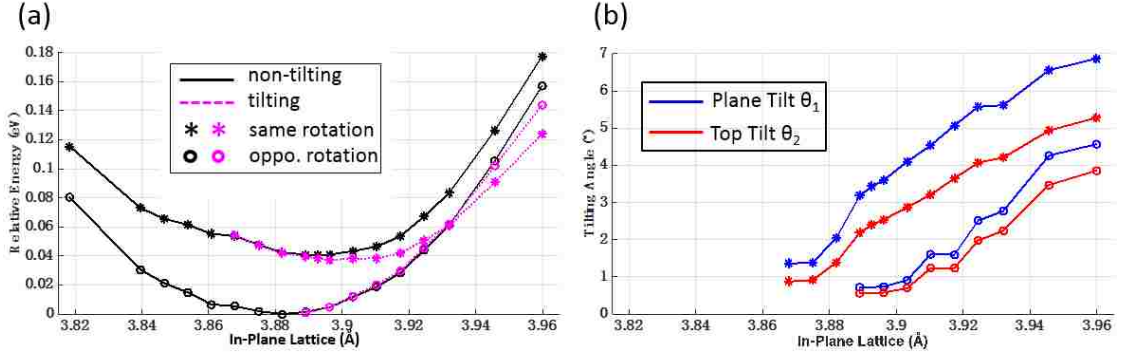
FIGURE 4.16: (a) Lattice constant dependence of the total energy calculated by DFT. When the two octahedra have the same rotation direction, there is a energy minimum with the existence of tilt. When the octahedra are rotating in different directions, the energy difference with and without tilt cannot be clearly distinguished. The overall energy with different rotation is smaller than with same rotation. (b) Tilt angles at the corresponding lattice parameters. At minimum energy with the same rotation, the tilt angles are $\theta_1 \sim 3.5°$ and $\theta_2 \sim 2.5°$, consistent with the results from LEED I-V simulation.

relaxed $\theta_2 < 0.5$. Figure 4.16(b) shows the plane and top tilt angles at various lattice constants for the same- and opposite-rotation structure, separately.

For the structure with opposite rotation, the energy difference between with and without tilt is negligible, with the minimum energy having no tilt. While for the structure with same rotation, as the in-plane lattice constant increases, the structure with tilt clearly has lower energy than without tilt. Meanwhile, the minimum-energy structure with same rotation has tilt angles $\theta_1 \sim 3.6$ and $\theta_2 \sim 2.5$, consistent with the LEED I-V calculation in Fig. 4.14.

4.3 LEED and HREELS Analysis of Mn Doped $Sr_3(Ru_{1-x}Mn_x)_2O_7$
4.3.1 LEED Line-profile Analysis of $Sr_3(Ru_{1-x}Mn_x)_2O_7$

Fig. 4.17(a)$\sim$(d) show the LEED pattern taken at 86K at 225eV for the four different doping level samples which are also used in HREELS measurement. The existence of tilt distortion causes the broken of glideline symmetry along one direction, thus the LEED pattern symmetry is lower than four-fold C_{4v} which is the case for rotational distortion only. Line-profile curves are collected by measuring

the intensities of the image spots with respect to their locations. Four curves are obtained based on the dashed line on each LEED pattern image for all four doping levels, shown in Fig. 4.17(e). With the orthorhombic unit cell, the reciprocal lattice is indicated by the black square in Fig. 4.17(a). Using this for labeling the LEED pattern, the dashed line crosses (3,1), (3,0), (3,-1) spots in sequence. These line-profiles are normalized with respect to the average intensity of the (3,1) and (3,-1) peaks. For each curve, all three peaks are fitted by Gaussian function, shown as the red and blue peaks in Fig. 4.17(e). As described in [140, 87], the emergence of the (3,0) and (-3,0) spots (indicated by green circles in Fig. 4.17(a)) is from the broken glideline symmetry, thus its intensity is a signature of tilt distortion. The relative intensity of the (3,0) peak is determined by dividing the area of this peak (red) by the average of the two (3,1) and (3,-1) peaks (blue) from the fitting results. The intensity results are shown in the inset of Fig. 4.17(e). The current result shows that as the doping level increases, the intensity of the (3,0) spot reduces, which means a decrease of the tilt distortion with increasing doping.

4.3.2 HREELS Analysis of Electron-Phonon Coupling on the Surface of $Sr_3(Ru_{1-x}Mn_x)_2O_7$

Fig. 4.18 shows the HREELS phonon spectrum $x=0$ and $x=0.16$ samples at 86K. It shows three phonon peaks classes. These three peaks classes have energies of $\omega_1 \sim 30$meV, $\omega_2 \sim 50$meV, and $\omega_3 \sim 70$meV, which are consistent with the previous measurement on Sr_2RuO_4 compound[141] and can be identified as external cage, bending, and stretching mode respectively. By comparing with the bulk $Sr_3Ru_2O_7$ [142] and surface Sr_2RuO_4 [141] measurements, the ω_3 phonon is assigned as the A_{1g} stretching mode of apical oxygen atoms. The movement of atoms in this mode is presented in the inset of Fig. 4.18. In comparison, the corresponding bulk phonon has the energy of 71.5 meV [142], which is higher than the 69.2 meV surface phonon
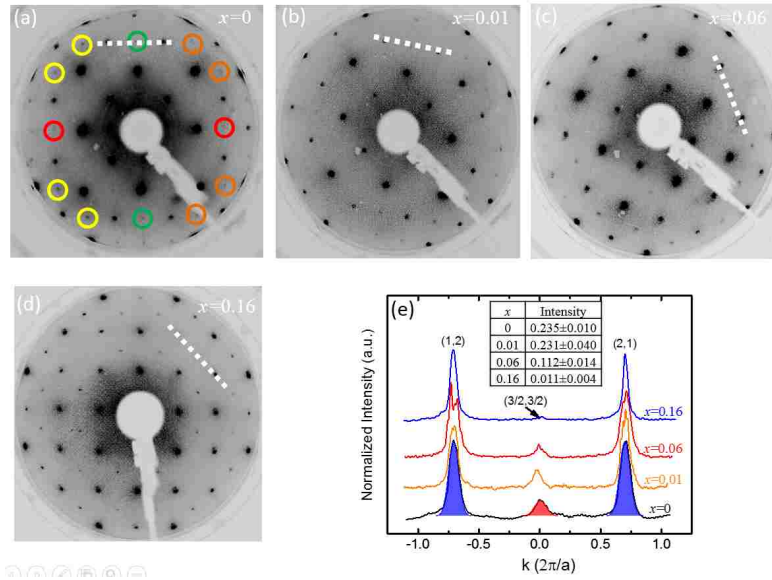
FIGURE 4.17: (a,b,c,d) LEED pattern taken at 86 K at 225 eV for four different doping levels of x=0, 0.01, 0.06, 0.16 respectively. The reciprocal lattice from the orthorhombic unit cell is indicated by the black square. The dashed line crosses the (3,1), (3,0), (3,-1) spots of the pattern. The green circles show the locations of the two diffracted spots along the broken glideline, and the red circles show the locations of the two extinguished spots along the reserved glideline. The yellow and orange circles indicate the locations of the spots with different intensities (yellow for large intensities and orange for small intensities). (e) Normalized line profile along the dashed line in (a)(b)(c) for the corresponding doping levels. The Gaussian fitting of the three peaks are presented by the blue and red shaded peaks. Inset: Table of relative intensity of the (3,0) spot obtained by normalizing its intensity with respect to the average intensities of (3,1) and (3,-1) spots calculated from the fitting results.

measured by HREELS. Note in the bulk this is a Raman mode which has symmetric movements of the two apical oxygen atoms, thus no dipole moment. At the surface, the dipole moment is from the creation of the surface broken symmetry.
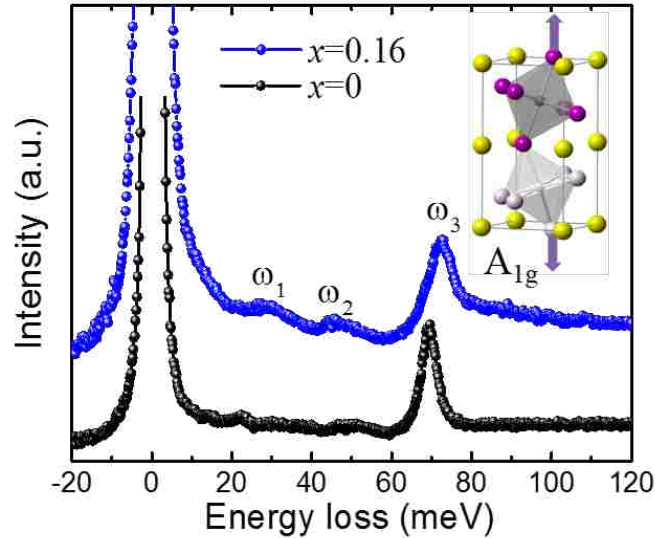
FIGURE 4.18: HREELS phonon spectrum for the surface of $x{=}0$ and $x{=}0.16$ samples at 86K. Inset shows the atomic displacements of the optical phonon modes associated with ω_3. It is an A_{1g} stretching mode of the apical oxygen atoms.

The background removing of the HREELS spectra is presented in Fig. 4.19, which is the $x{=}0.16$ sample at 86 K for better presenting the fitting process. The left side of the elastic peaks is fitted with a Gaussian function. The left side is chosen because there is asymmetry on the elastic peak caused by the Drude tail, which is due to the intraband electron-hole pairing across the Fermi energy. This asymmetry can be clearly observed after zooming in the spectra for $\sim$50 times, shown in Fig. 4.19(b). The Drude tail is determined by the right side of the leftover after removing the Gaussian function, and it is fitted by a Lorentzian function which is also centered at zero in analogy to infrared spectroscopy. The highest energy phonon ω_3 is fitted with a Fano lineshape which has been described in the

main text. The other two peaks are fitted by two symmetric Lorentzian functions. Note that even the higher right side of the ω_3 peak can be partly fitted by the Fano lineshape, there is still spectra weight at energy higher than 100 meV. This is fitted by a Shirley background which results from the electron energy loss when coming out of the sample and approximately proportional to the spectrum intensity, just like the case in X-ray photoelectron spectroscopy (XPS). In a word, the background consists of elastic peak, Drude tail, and Shirley background; the phonon peaks are fitted by Lorentzian functions with one fitted by a Fano lineshape. All the fitting results are shown in Fig 4.19(c), which is ∼60 times zoom in of part of Fig. 4.19(a).

We focus on the highest energy phonon ω_3 because it not only has the largest intensity but also displays apparent asymmetric lineshape especially for the x=0.16 sample. In comparison, each of the other two does not have good enough signal-to-noise ratio for lineshape analysis. This asymmetry is analyzed through Fano lineshape, which is due to the interference between a discrete resonance scattering process and a continuum of background [143], consistent with the previous Raman spectroscopy study on similar compounds [142, 144, 145]. In this case, the "resonance" is the phonon excitation, and the "continuum" is the electron-hole pairing excitation sketched in Fig. 4.20. Therefore larger density of states (DOS) near the Fermi level creates more excitations, and leads to a more asymmetric lineshape.

The equation of Fano lineprofile is $I(\omega) = I_0(\epsilon + q)^2/(1 + \epsilon^2)$, where $\epsilon = (\omega - \omega_0)/\Gamma$, ω_0 is the bare phonon energy, and Γ is the intrinsic linewidth. The parameter q is the Fano parameter which is an indication of the asymmetry of the line profile. The smaller the q is, the more asymmetric the peak line profile is. It is very important in our analysis because it is a direct measurement of the metallicity of the system.
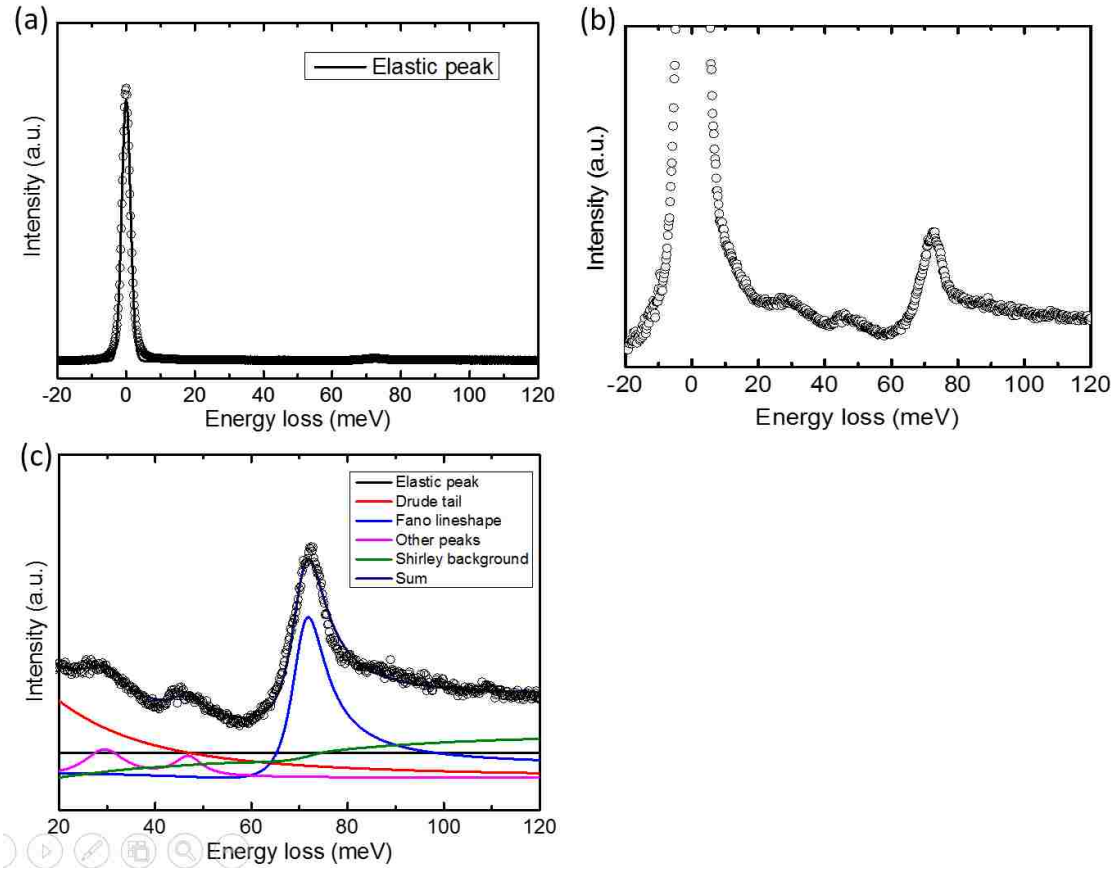
FIGURE 4.19: (a) Full HREELS scan of the x=0.16 sample at 86K. The elastic peak is fitted by a symmetric Gaussian function. (b) 50 times zoom in of (a). The elastic peak shows a clear asymmetry at this scale. (c) 60 times zoom in of part of (a) with the fitting of the spectrum. The background is constructed by the elastic peak, the Drude spectral weight and the Shirley background. The strongest peak around 70 meV is fitted by the Fano lineshape.

123
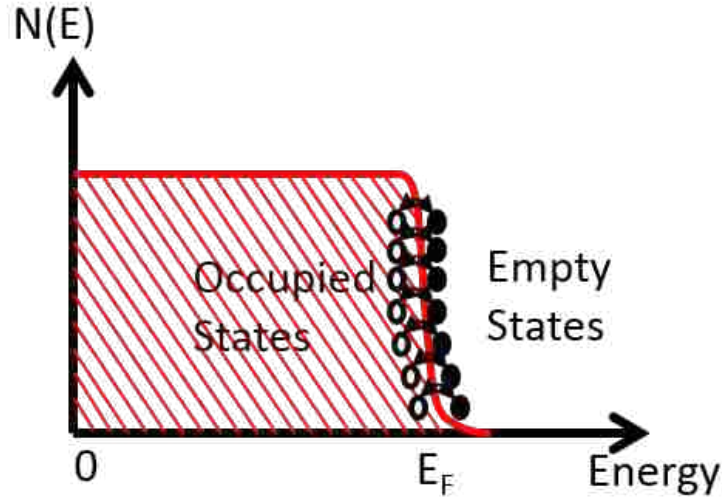
FIGURE 4.20: Sketch of the electron-hole excitations near the Fermi level.

Fig. 4.21 compares the HREELS spectra at the same temperature but with different doping levels. The spectra were obtained after removing the background and other phonon peaks. The measured data were presented in open circles for the four different doping levels x=0, 0.01, 0.06, and 0.16. There is little difference between the spectra of x=0, 0.01, and 0.06 (low doping) compounds, as both exhibits nearly symmetric ω_3 peak lineshape. However, the ω_3 peak from the x=0.16 sample spectrum shows evident asymmetric lineshape. This indicates the coupling of the phonon and the electronic-hole pairing continuum has changed when x=0.16.

The values of q at different doping levels are shown in Fig. 4.22. With increasing Mn concentration the peak becomes more asymmetric with smaller q. This indicates the surface has higher DOS with more Mn. Considering the tilt angle is zero beyond $x = 0.16$, the surface is more metallic with less tilt. The relationship between the surface structure and properties can be inferred from Fig. 4.22, where the metal to poor metal transition is coupled to the tilt angle. The behavior is linear as expected for a 2D second order transition on the surface while the bulk structural transition is 3D like.
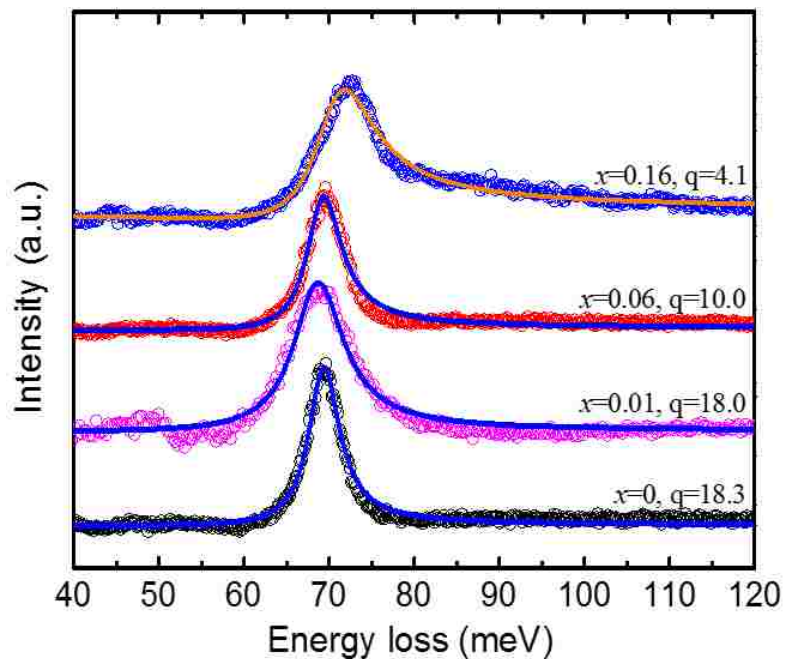
FIGURE 4.21: The 86K EELS data and its Fano lineshape fitting after removing the background and other phonons for four different doping levels. The line profile becomes more asymmetric when the doping level increases.
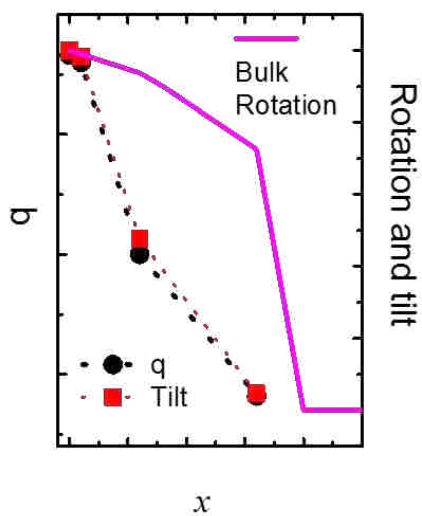
FIGURE 4.22: Summary of values of values of q's and rotation and tilt angles at different doping levels.
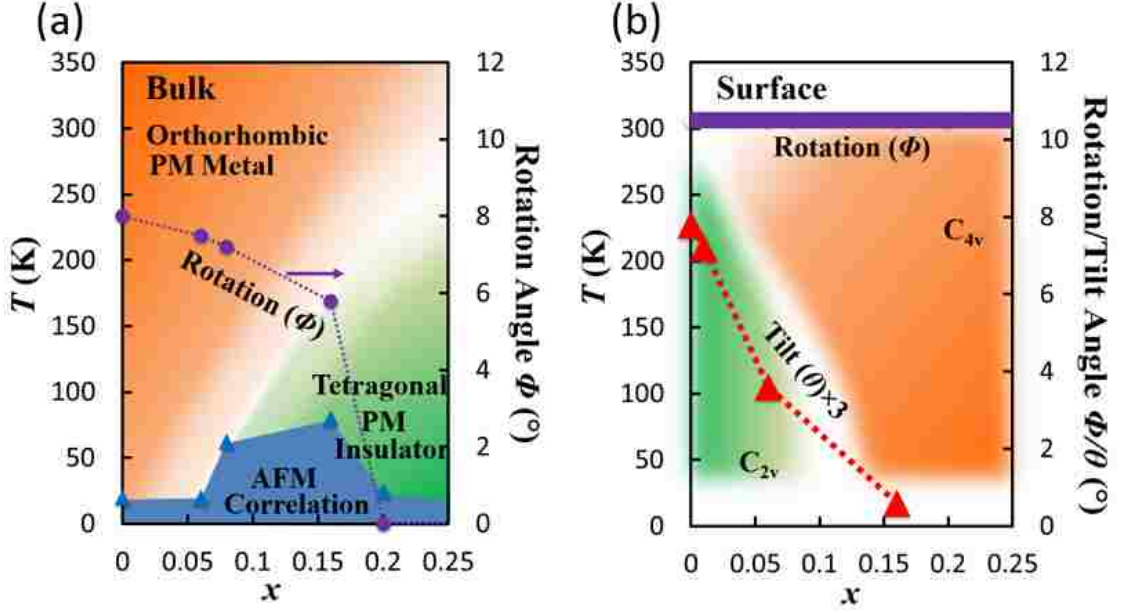
FIGURE 4.23: Comparison of surface and bulk phase diagrams of $Sr_3(Ru_{1-x}Mn_x)_2O_7$. (a) Bulk. (b) Surface.

4.4 Analysis and Conclusions

The surface and bulk structure-property relationship is summarized in Fig. 4.23. As Mn doping increases, surface has a constant rotation and a decreasing tilt, while bulk only has decreasing rotation. With such structural difference, the bulk becomes more insulating when the doping level increases, but the surface shows opposite tendency of the doping dependence. In the bulk, the sample with larger octahedral rotation has larger conductivity, which is the case for $x = 0.16$ surface when the rotational distortion is enhanced and stabilized. However for parent compound and low doping samples, the existence of tilt distortion forces the surface insulating, in the same way as single layer $Ca_{2-x}Sr_xRuO_4$ [8].

For $Ca_{2-x}Sr_xRuO_4$ the surface stabilizes rotation while reduces tilt. However, the $Sr_3(Ru_{1-x}Mn_x)_2O_7$ compound behaves fundamentally different between the surface and the bulk. The $Sr_3(Ru_{1-x}Mn_x)_2O_7$ surface enhances rotation and further induces tilt, not seen in any doping level of $Ca_{2-x}Sr_xRuO_4$. There are two

possible reasons for such structural difference: First is the number of layers (dimensionality n) difference. The non-doped $n = 1$ compound Sr_2RuO_4 does not have any rotation or tilt in the bulk, while the non-doped $n = 2$ compound $Sr_3Ru_2O_7$ already has octahedra rotational distortion. This indicates that structural instability is enhanced as n increases, so there is further distortions for $Sr_4Ru_3O_{10}$ ($n = 3$) and $SrRuO_3$ ($n = \infty$) compounds [146, 147, 148, 149].

The second reason is the difference in doping sites and valences. In $Ca_{2-x}Sr_xRuO_4$ the Ca cation is doped at the alkaline earth metal Sr site and it is an isovalent doping, but in $Sr_3(Ru_{1-x}Mn_x)_2O_7$ the Mn cation is doped at transition metal Ru site and a Mn atom has 1 less valence electron than a Ru atom. In general in the RP series $A_{n+1}B_nO_{3n+1}$ it is considered that A-site ion affects the cage surrounding the octahedra and the overall structure of the compounds, especially the c-axis parameters. In contrast, B-site ion affects the BO_6 octahedra as well as the B-O plane, i.e. the a-axis parameters. Mn could also possibly be an aliovalent dopant, since there is indication that the Mn exhibits 3+ valence instead of the 4+ for Ru [150]. Therefore it can be expected that $Sr_3(Ru_{1-x}Mn_x)_2O_7$ has a more distorted structure both in the bulk and on the surface. The surface lattice distortion of isovalent doped $(Sr_{1-x}Ca_x)_3Ru_2O_7$, which has tilt in the bulk at high doping levels [85, 139], could be more close to its bulk distortion at each corresponding doping level.

The octahedra distort to relieve the excess strain from the neighboring cations. A neutron diffraction study on parent $Sr_3Ru_2O_7$ structural behavior under hydrostatic pressure observed slight increase of rotation angle with increasing pressure [72]. When extra strain is created from the broken symmetry at the surface, rotational distortion cannot fully relieve the strain, resulting in tilt distortion. The double layer nature of this material can bring complicated relationship between

127

the top and bottom octahedra. In the bulk, the two layers in the unit cell rotate in different directions with the same magnitude [68]. At the surface, this is not necessarily true. We do not have enough information from LEED to examine the rotation of the second octahedral layer. However if there is tilt distortion on the first layer, the second layer must also have tilt distortion towards the opposite direction because the two octahedra share an oxygen atom. The tilt angle for the two layers can be different when there is different Jahn-Teller distortion of the first and second layer octahedra.

In summary, we have used the combination of LEED I-V analysis, DFT, and HREELS to investigate the surface structure and its relationship with the surface electronic properties of $Sr_3(Ru_{1-x}Mn_x)_2O_7$. There is a broken reflection symmetry on LEED pattern which is caused by the tilt distortion according to the simulation. The tilt angle from LEED I-V calculation also confirms this origin, and is consistent with DFT calculations. Further HREELS measurements on Mn doped samples indicate that the surface metallicity is strongly coupled to the surface structure. The system is turning more conducting with decreasing tilt and enhanced rotation compared to the bulk. This picture is consistent with the theoretical phase diagram deduced for the single layer $Ca_{2-x}Sr_xRuO_4$ compound with a less distorted structure.

References

[1] M. Rahlenbeck, G. Sun, D. Sun, C. Lin, B. Keimer, and C. Ulrich. Phonon anomalies in pure and underdoped $R_{1-x}K_xFe_2As_2$ (R=Ba, Sr) investigated by Raman light scattering. *Physical Review B*, 80(6), 2009.

[2] K. Y. Choi, N. Ni, S. L. Bud'ko, and P. C. Canfield. Lattice and electronic anomalies of $CaFe_2As_2$ studied by raman spectroscopy. *Physical Review B*, 78(21), 2008.

[3] M Braden, W Reichardt, S Nishizaki, Y Mori, and Y Maeno. Structural stability of Sr_2RuO_4. *Physical Review B*, 57(2):1236, 1998.

[4] Biao Hu. *Evolution of Structural and Physical Properties of Transition Metal Oxide $Sr_3(Ru_{1-x}Mn_x)_2O_7$ ($0 \leq x \leq 0.7$) with Mn Concentration*. Thesis, 2011.

[5] A. Damascelli, D. H. Lu, K. M. Shen, N. P. Armitage, F. Ronning, D. L. Feng, C. Kim, Z. X. Shen, T. Kimura, Y. Tokura, Z. Q. Mao, and Y. Maeno. Fermi surface, surface states, and surface reconstruction in Sr_2RuO_4. *Physical Review Letters*, 85(24):5194–5197, 2000.

[6] II Mazin and David J Singh. Ferromagnetic spin fluctuation induced superconductivity in Sr_2RuO_4. *Physical review letters*, 79(4):733, 1997.

[7] AP Mackenzie, SR Julian, AJ Diver, GJ McMullan, MP Ray, GG Lonzarich, Y Maeno, S Nishizaki, and T Fujita. Quantum Oscillations in the Layered Perovskite Superconductor Sr_2RuO_4. *Physical review letters*, 76(20):3786, 1996.

[8] Z. Fang and K. Terakura. Magnetic phase diagram of $Ca_{2-x}Sr_xRuO_4$ governed by structural distortions. *Physical Review B*, 64(2), 2001.

[9] S Lehwald, JM Szeftel, H Ibach, Talat S Rahman, and DL Mills. Surface phonon dispersion of Ni (100) measured by inelastic electron scattering. *Physical review letters*, 50(7):518, 1983.

[10] PA Cox. *The surface science of metal oxides*. Cambridge university press, 1996.

[11] Rob Moore. *Manifestations of Broken Symmetry: The Surface Phases of $Ca_{2-x}Sr_xRuO_4$*. Thesis, 2006.

[12] R. G. Moore, V. B. Nascimento, Jiandi Zhang, J. Rundgren, R. Jin, D. Mandrus, and E. W. Plummer. Manifestations of Broken Symmetry: The Surface Phases of $Ca_{2-x}Sr_xRuO_4$. *Physical Review Letters*, 100(6):066102, 2008.

[13] Piers Coleman and Andrew J Schofield. Quantum criticality. *Nature*, 433(7023):226–229, 2005.

[14] Joseph I Goldstein, Dale E Newbury, Patrick Echlin, David C Joy, Charles Fiori, and Eric Lifshin. *Electron-Beam-Specimen Interactions*, pages 53–122. Springer, 1981.

[15] Andrew Zangwill. *Physics at surfaces*. Cambridge University Press, 1988.

[16] Guorong Li. *Coupling between spin, lattice, and charge at the surface of complex transition metal compounds*. Thesis, 2013.

[17] W. Ho, R. F. Willis, and E. W. Plummer. Observation of nondipole electron impact vibrational excitations: H on W(100). *Physical Review Letters*, 40(22):1463–1466, 1978.

[18] Shuheng Pan. 2009.

[19] G. Li, Q. Li, M. Pan, B. Hu, C. Chen, J. Teng, Z. Diao, J. Zhang, R. Jin, and E. W. Plummer. Atomic-scale fingerprint of mn dopant at the surface of $Sr_3(Ru_{1-x}Mn_x)_2O_7$. *Sci Rep*, 3:2882, 2013.

[20] R. S. Perry, L. M. Galvin, S. A. Grigera, L. Capogna, A. J. Schofield, A. P. Mackenzie, M. Chiao, S. R. Julian, S. I. Ikeda, S. Nakatsuji, Y. Maeno, and C. Pfleiderer. Metamagnetism and Critical Fluctuations in High Quality Single Crystals of the Bilayer Ruthenate $Sr_3Ru_2O_7$. *Physical Review Letters*, 86(12):2661–2664, 2001.

[21] Shin-Ichi Ikeda, Yoshiteru Maeno, Satoru Nakatsuji, Masashi Kosaka, and Yoshiya Uwatoko. Ground state in $Sr_3Ru_2O_7$: Fermi liquid close to a ferromagnetic instability. *Physical Review B*, 62(10):R6089–R6092, 2000.

[22] R. Mathieu, A. Asamitsu, Y. Kaneko, J. He, X. Yu, R. Kumai, Y. Onose, N. Takeshita, T. Arima, H. Takagi, and Y. Tokura. Impurity-induced transition to a mott insulator in $Sr_3Ru_2O_7$. *Physical Review B*, 72(9), 2005.

[23] Robert J Birgeneau, Marc A Kastner, et al. Frontier physics with correlated electrons. *Science*, 288(5465):437–437, 2000.

[24] J. G. Bednorz and K. A. M?ller. Possible high T_c superconductivity in the ba-la-cu-o system. *Zeitschrift fur Physik B Condensed Matter*, 64(2):189–193, 1986.

[25] DN Basov and Andrey V Chubukov. Manifesto for a higher Tc. *Nature Physics*, 7(4):272–276, 2011.

[26] Y. Kamihara, T. Watanabe, M. Hirano, and H. Hosono. Iron-based layered superconductor $La(O_{(1-x)}F_{(x)})FeAs$ ($x = 0.05$-0.12) with $T(c) = 26$ K. *Journal of the American Chemical Society*, 130(11):3296–7, 2008.

[27] S. Nandi, M. G. Kim, A. Kreyssig, R. M. Fernandes, D. K. Pratt, A. Thaler, N. Ni, S. L. Bud'ko, P. C. Canfield, J. Schmalian, R. J. McQueeney, and A. I. Goldman. Anomalous suppression of the orthorhombic lattice distortion in superconducting $Ba(Fe_{1-x}Co_x)_2As_2$ single crystals. *Physical Review Letters*, 104(5):057006, 2010.

[28] Marianne Rotter, Marcus Tegel, and Dirk Johrendt. Superconductivity at 38 K in the iron arsenide $(Ba_{1-x}K_x)Fe_2As_2$. *Physical Review Letters*, 101(10):107006, 2008.

[29] CW Chu, PH Hor, RL Meng, L Gao, ZJ Huang, Wang, and YQ. Evidence for superconductivity above 40 k in the La-Ba-Cu-O compound system. *Physical Review Letters*, 58(4):405, 1987.

[30] S Medvedev, TM McQueen, IA Troyan, T Palasyuk, MI Eremets, RJ Cava, S Naghavi, F Casper, V Ksenofontov, G Wortmann, et al. Electronic and magnetic phase diagram of β-Fe1. 01Se with superconductivity at 36.7 K under pressure. *Nature materials*, 8(8):630–633, 2009.

[31] Maw-Kuen Wu, Jo R Ashburn, C_J Torng, Ph H Hor, Rl L Meng, Lo Gao, Z J_ Huang, YQ Wang, and CW Chu. Superconductivity at 93 K in a new mixed-phase Y-Ba-Cu-O compound system at ambient pressure. *Physical Review Letters*, 58(9):908, 1987.

[32] Yoshikazu Mizuguchi, Fumiaki Tomioka, Shunsuke Tsuda, Takahide Yamaguchi, and Yoshihiko Takano. Substitution effects on FeSe superconductor. *Journal of the Physical Society of Japan*, 78(7):074712, 2009.

[33] G Cao, CS Alexander, S McCall, JE Crow, and RP Guertin. From antiferromagnetic insulator to ferromagnetic metal: a brief review of the layered ruthenates. *Materials Science and Engineering: B*, 63(1):76–82, 1999.

[34] O. Friedt, M. Braden, G. André, P. Adelmann, S. Nakatsuji, and Y. Maeno. Structural and magnetic aspects of the metal-insulator transition in $Ca_{2-x}Sr_xRuO_4$. *Physical Review B*, 63(17), 2001.

[35] S. Nakatsuji, D. Hall, L. Balicas, Z. Fisk, K. Sugahara, M. Yoshioka, and Y. Maeno. Heavy-mass fermi liquid near a ferromagnetic instability in layered ruthenates. *Physical Review Letters*, 90(13):137202, 2003.

[36] Elbio Dagotto. Complexity in strongly correlated electronic systems. *Science*, 309(5732):257–262, 2005.

[37] R. Moore, M. Lumsden, M. Stone, Jiandi Zhang, Y. Chen, J. Lynn, R. Jin, D. Mandrus, and E. Plummer. Phonon softening and anomalous mode near the $x_c=0.5$ quantum critical point in $Ca_{2-x}Sr_xRuO_4$. *Physical Review B*, 79(17), 2009.

[38] Yoshiteru Maeno, T Maurice Rice, and Manfred Sigrist. The intriguing superconductivity of strontium ruthenate. *Physics Today*, 54(1):42–47, 2001.

[39] K Ishida, H Mukuda, Y Kitaoka, K Asayama, ZQ Mao, Y Mori, and Y Maeno. Spin-triplet superconductivity in Sr_2RuO_4 identified by ^{17}O knight shift. *Nature*, 396(6712):658–660, 1998.

[40] GM Luke, Y Fudamoto, KM Kojima, MI Larkin, J Merrin, B Nachumi, YJ Uemura, Y Maeno, ZQ Mao, Y Mori, et al. Time-reversal symmetry-breaking superconductivity in Sr_2RuO_4. *Nature*, 394(6693):558–561, 1998.

[41] J. A. Duffy, S. M. Hayden, Y. Maeno, Z. Mao, J. Kulda, and G. J. McIntyre. Polarized-neutron scattering study of the cooper-pair moment in Sr_2RuO_4. *Physical Review Letters*, 85(25):5412–5415, 2000.

[42] A. P. Mackenzie, J. W. Reiner, A. W. Tyler, L. M. Galvin, S. R. Julian, M. R. Beasley, T. H. Geballe, and A. Kapitulnik. Observation of quantum oscillations in the electrical resistivity of $SrRuO_3$. *Physical Review B*, 58(20):R13318–R13321, 1998. PRB.

[43] Christoph Bergemann, SR Julian, AP Mackenzie, S NishiZaki, and Y Maeno. Detailed topography of the fermi surface of Sr_2RuO_4. *Physical review letters*, 84(12):2662, 2000.

[44] Y Maeno, H Hashimoto, K Yoshida, S Nishizaki, T Fujita, JG Bednorz, and F Lichtenberg. Superconductivity in a layered perovskite without copper. *Nature*, 372(6506):532–534, 1994.

[45] D. H. Lu, M. Schmidt, T. R. Cummins, S. Schuppler, F. Lichtenberg, and J. G. Bednorz. Fermi Surface and Extended van Hove Singularity in the Noncuprate Superconductor Sr_2RuO_4. *Phys. Rev. Lett.*, 76:4845–4848, Jun 1996.

[46] T Yokoya, A Chainani, T Takahashi, H Ding, JC Campuzano, H Katayama-Yoshida, M Kasai, and Y Tokura. Angle-resolved photoemission study of Sr_2RuO_4. *Physical Review B*, 54(18):13311, 1996.

[47] R. Matzdorf, Z. Fang, Ismail, Jiandi Zhang, T. Kimura, Y. Tokura, K. Terakura, and E. W. Plummer. Ferromagnetism stabilized by lattice distortion at the surface of the p-wave superconductor Sr_2RuO_4. *Science*, 289(5480):746–748, 2000.

[48] Zhong Fang, Kiyoyuki Terakura, and Naoto Nagaosa. Orbital physics in ruthenates: first-principles studies. *New Journal of Physics*, 7:66–66, 2005.

[49] T Imai, AW Hunt, KR Thurber, and FC Chou. O^{17} NMR evidence for orbital dependent ferromagnetic correlations in Sr_2RuO_4. *Physical review letters*, 81(14):3006, 1998.

[50] Y. Sidis, M. Braden, P. Bourges, B. Hennion, S. NishiZaki, Y. Maeno, and Y. Mori. Evidence for incommensurate spin fluctuations in Sr_2RuO_4. *Physical Review Letters*, 83(16):3320–3323, 1999. PRL.

[51] F. Servant, B. F?k, S. Raymond, J. Brison, P. Lejay, and J. Flouquet. Magnetic excitations in the normal and superconducting states of Sr_2RuO_4. *Physical Review B*, 65(18), 2002.

[52] II Mazin and David J Singh. Competitions in layered ruthenates: ferromagnetism versus antiferromagnetism and triplet versus singlet pairing. *Physical review letters*, 82(21):4324, 1999.

[53] K Ishida, H Mukuda, Y Minami, Y Kitaoka, ZQ Mao, H Fukazawa, and Y Maeno. Normal-state spin dynamics in the spin-triplet superconductor Sr_2RuO_4. *Physical Review B*, 64(10):100501, 2001.

[54] M Braden, G Andre, S Nakatsuji, and Y Maeno. Crystal and magnetic structure of Ca_2RuO_4: Magnetoelastic coupling and the metal-insulator transition. *Physical Review B*, 58(2):847, 1998.

[55] M Uehara, S Mori, CH Chen, and S-W Cheong. Percolative phase separation underlies colossal magnetoresistance in mixed-valent manganites. *Nature*, 399(6736):560–563, 1999.

[56] H. Köppel, D.R. Yarkony, and H. Barentzen. *The Jahn-Teller Effect: Fundamentals and Implications for Physics and Chemistry*. Springer Series in Chemical Physics. Springer Berlin Heidelberg, 2009.

[57] Dalgis Mesa. *Neutron Scattering Studies of Unusual Spin Structure and Local Correlation in Complex Oxides*. PhD thesis, Louisiana State University, 2014.

[58] John Bardeen. Surface states and rectification at a metal semi-conductor contact. *Physical Review*, 71(10):717, 1947.

[59] IE Tamm. On the possible bound states of electrons on a crystal surface. *Phys. Z. Sowjetunion*, 1:733–735, 1932.

[60] William Shockley. On the surface states associated with a periodic potential. *Physical review*, 56(4):317, 1939.

[61] S. D. Kevan. Evidence for a new broadening mechanism in angle-resolved photoemission from cu(111). *Phys. Rev. Lett.*, 50:526–529, Feb 1983.

[62] M. Z. Hasan and C. L. Kane. Colloquium: Topological insulators. *Reviews of Modern Physics*, 82(4):3045–3067, 2010.

[63] Michele Lazzeri and Stefano de Gironcoli. Ab-initio dynamical properties of the Be(0001) surface. *Surface Science*, 402:715–718, 1998.

[64] Ronald Fuchs and KL Kliewer. Optical modes of vibration in an ionic crystal slab. *Physical Review*, 140(6A):A2076, 1965.

[65] H Nienhaus and W Mönch. Dispersion of GaAs (110) surface phonons measured with HREELS. *Physical Review B*, 50(16):11750, 1994.

[66] R. Matzdorf, Ismail, T. Kimura, Y. Tokura, and E. Plummer. Surface structural analysis of the layered perovskite Sr_2RuO_4 by LEED I(V). *Physical Review B*, 65(8), 2002.

[67] R. G. Moore, J. Zhang, V. B. Nascimento, R. Jin, J. Guo, G. T. Wang, Z. Fang, D. Mandrus, and E. W. Plummer. A surface-tailored, purely electronic, Mott metal-to-insulator transition. *Science*, 318(5850):615–9, 2007.

[68] Biao Hu, Gregory T McCandless, Vasile O Garlea, S Stadler, Yimin Xiong, Julia Y Chan, E Ward Plummer, and R Jin. Structure-property coupling in $Sr_3(Ru_{1-x}Mn_x)_2O_7$. *Physical Review B*, 84(17):174411, 2011.

[69] J. Teng, C. Chen, Y. Xiong, J. Zhang, R. Jin, and E. W. Plummer. Anomalous surface lattice dynamics in the low-temperature phase of $Ba(Fe_{1-x}Co_x)_2As_2$. *Proceedings of the National Academy of Sciences of the United States of America*, 110(3):898–903, 2013.

[70] Guorong Li, Xiaobo He, Jiandi Zhang, Rongying Jin, A. S. Sefat, M. A. McGuire, D. G. Mandrus, B. C. Sales, and E. W. Plummer. Coupled structural and magnetic antiphase domain walls on $BaFe_2As_2$. *Physical Review B*, 86(6):060512, 2012.

[71] Q Huang, JW Lynn, RW Erwin, J Jarupatrakorn, and RJ Cava. Oxygen displacements and search for magnetic order in $Sr_3Ru_2O_7$. *Physical Review B*, 58(13):8515, 1998.

[72] H. Shaked, J. D. Jorgensen, O. Chmaissem, S. Ikeda, and Y. Maeno. Neutron diffraction study of the structural distortions in $Sr_3Ru_2O_7$. *Journal of Solid State Chemistry*, 154(2):361–367, 2000.

[73] R. A. Borzi, S. A. Grigera, J. Farrell, R. S. Perry, S. J. Lister, S. L. Lee, D. A. Tennant, Y. Maeno, and A. P. Mackenzie. Formation of a nematic fluid at high fields in $Sr_3Ru_2O_7$. *Science*, 315(5809):214, 2007.

[74] S. A. Grigera, R. S. Perry, A. J. Schofield, M. Chiao, S. R. Julian, G. G. Lonzarich, S. I. Ikeda, Y. Maeno, A. J. Millis, and A. P. Mackenzie. Magnetic field-tuned quantum criticality in the metallic ruthenate $Sr_3Ru_2O_7$. *Science*, 294(5541):329–32, 2001.

[75] SL Sondhi, SM Girvin, JP Carini, and D Shahar. Continuous quantum phase transitions. *Reviews of Modern Physics*, 69(1):315, 1997.

[76] Philipp Gegenwart, Qimiao Si, and Frank Steglich. Quantum criticality in heavy-fermion metals. *Nat Phys*, 4(3):186–197, 2008.

[77] Subir Sachdev and Bernhard Keimer. Quantum criticality. *Physics Today*, 64(2):29, 2011.

[78] John A. Hertz. Quantum critical phenomena. *Physical Review B*, 14(3):1165–1184, 1976.

[79] A. J. Millis. Effect of a nonzero temperature on quantum critical points in itinerant fermion systems. *Physical Review B*, 48(10):7183–7196, 1993.

[80] R. S. Perry, K. Kitagawa, S. A. Grigera, R. A. Borzi, A. P. Mackenzie, K. Ishida, and Y. Maeno. Multiple First-Order Metamagnetic Transitions and Quantum Oscillations in Ultrapure $Sr_3Ru_2O_7$. *Physical Review Letters*, 92(16), 2004.

[81] SA Grigera, P Gegenwart, RA Borzi, F Weickert, AJ Schofield, RS Perry, T Tayama, T Sakakibara, Y Maeno, and AG Green. Disorder-sensitive phase formation linked to metamagnetic quantum criticality. *Science*, 306(5699):1154–1157, 2004.

[82] Dalgis Mesa, Feng Ye, Songxue Chi, J. A. Fernandez-Baca, W. Tian, Biao Hu, R. Jin, E. W. Plummer, and Jiandi Zhang. Single-bilayer E-type antiferromagnetism in Mn-substituted $Sr_3Ru_2O_7$: Neutron scattering study. *Physical Review B*, 85(18), 2012.

[83] Zhe Qu, Leonard Spinu, Huiqiu Yuan, Vladimir Dobrosavljevi?, Wei Bao, Jeffrey Lynn, M. Nicklas, Jin Peng, Tijiang Liu, David Fobes, Etienne Flesch, and Z. Mao. Unusual heavy-mass nearly ferromagnetic state with a surprisingly large wilson ratio in the double layered ruthenates (sr1-xcax)3ru2o7. *Physical Review B*, 78(18), 2008.

[84] Zhe Qu, Jin Peng, Tijiang Liu, David Fobes, Leonard Spinu, and Zhiqiang Mao. Complex electronic states in double-layered ruthenates $(Sr_{1-x}Ca_x)_3Ru_2O_7$. *Physical Review B*, 80(11), 2009.

[85] Jin Peng, Zhe Qu, Bin Qian, David Fobes, Tijiang Liu, Xiaoshan Wu, HM Pham, Leonard Spinu, and ZQ Mao. Interplay between the lattice and spin degrees of freedom in $(Sr_{1-x}Ca_x)_3Ru_2O_7$. *Physical Review B*, 82(2):024417, 2010.

[86] K. Iwaya, S. Satow, T. Hanaguri, N. Shannon, Y. Yoshida, S. I. Ikeda, J. P. He, Y. Kaneko, Y. Tokura, T. Yamada, and H. Takagi. Local tunneling spectroscopy across a metamagnetic critical point in the bilayer ruthenate $Sr_3Ru_2O_7$. *Physical Review Letters*, 99(5):057208, 2007. PRL.

[87] Biao Hu, Gregory T. McCandless, Melissa Menard, V. B. Nascimento, Julia Y. Chan, E. W. Plummer, and R. Jin. Surface and bulk structural properties of single-crystalline $Sr_3Ru_2O_7$. *Physical Review B*, 81(18), 2010.

[88] Georges Friedel. *étude sur les groupements cristallins*. Socit de l'Imprimerie Tholier, 1904.

[89] André Guinier. *X-ray diffraction in crystals, imperfect crystals, and amorphous bodies*. Courier Corporation, 1994.

[90] K. Oura, V.G. Lifshits, A. Saranin, A.V. Zotov, and M. Katayama. *Surface Science: An Introduction*. Advanced Texts in Physics. Springer Berlin Heidelberg, 2013.

[91] Neil Ashcroft and David Mermin. *Solid State Physics*. Thomson Learning, 1976.

[92] K Takubo, R Comin, D Ootsuki, Takashi Mizokawa, H Wadati, Y Takahashi, G Shibata, A Fujimori, R Sutarto, F He, et al. Bond order and the role of ligand states in stripe-modulated $IrTe_2$. *Physical Review B*, 90(8):081104, 2014.

[93] Jixia Dai, Kristjan Haule, JJ Yang, YS Oh, SW Cheong, and Weida Wu. Hierarchical stripe phases in $IrTe_2$ driven by competition between ir dimerization and te bonding. *Physical Review B*, 90(23):235121, 2014.

[94] WC Fan, A Ignatiev, H Huang, and SY Tong. Observation and structural determination of $(\sqrt{3} \times \sqrt{3})r30°$ reconstruction of the Si(111) surface. *Physical review letters*, 62(13):1516, 1989.

[95] Q Huang, JL Soubeyroux, O Chmaissem, I Natali Sora, A Santoro, RJ Cava, JJ Krajewski, and WF Peck. Neutron powder diffraction study of the crystal structures of Sr_2RuO_4 and Sr_2IrO_4 at room temperature and at 10 k. *Journal of Solid State Chemistry*, 112(2):355–361, 1994.

[96] Michel A Van Hove, Wolfgang Moritz, Herbert Over, Philip J Rous, Adrian Wander, Angelo Barbieri, Nick Materer, Ulrich Starke, and Gabor A Somorjai. Automated determination of complex surface structures by leed. *Surface Science Reports*, 19(3):191–229, 1993.

[97] M.A. VanHove, W.H. Weinberg, and C.M. Chan. *Low-Energy Electron Diffraction: Experiment, Theory and Surface Structure Determination*. Springer Berlin Heidelberg, 2012.

[98] J.B. Pendry. *Low Energy Electron Diffraction: The Theory and Its Application to Determination of Surface Structure*. Academic Press, 1974.

[99] JB Pendry. Reliability factors for leed calculations. *Journal of Physics C: Solid State Physics*, 13(5):937, 1980.

[100] H. Ibach and D.L. Mills. *Electron energy loss spectroscopy and surface vibrations.* Academic Press, 1982.

[101] M. G. Kim, R. M. Fernandes, A. Kreyssig, J. W. Kim, A. Thaler, S. L. Bud'ko, P. C. Canfield, R. J. McQueeney, J. Schmalian, and A. I. Goldman. Character of the structural and magnetic phase transitions in the parent and electron-doped $BaFe_2As_2$ compounds. *Physical Review B*, 83(13), 2011.

[102] A. I. Goldman, D. N. Argyriou, B. Ouladdiaf, T. Chatterji, A. Kreyssig, S. Nandi, N. Ni, S. L. Bud'ko, P. C. Canfield, and R. J. McQueeney. Lattice and magnetic instabilities in $CaFe_2As_2$: A single-crystal neutron diffraction study. *Physical Review B*, 78(10):100506, 2008.

[103] A. Jesche, N. Caroca-Canales, H. Rosner, H. Borrmann, A. Ormeci, D. Kasinathan, H. H. Klauss, H. Luetkens, R. Khasanov, A. Amato, A. Hoser, K. Kaneko, C. Krellner, and C. Geibel. Strong coupling between magnetic and structural order parameters in $SrFe_2As_2$. *Physical Review B*, 78(18):180504, 2008.

[104] Stephen Wilson, Z. Yamani, C. Rotundu, B. Freelon, E. Bourret-Courchesne, and R. Birgeneau. Neutron diffraction study of the magnetic and structural phase transitions in $BaFe_2As_2$. *Physical Review B*, 79(18), 2009.

[105] T. Egami, B. V. Fine, D. Parshall, A. Subedi, and D. J. Singh. Spin-lattice coupling and superconductivity in fe pnictides. *Advances in Condensed Matter Physics*, 2010:1–7, 2010.

[106] S LaShell, BAa McDougall, and E Jensen. Spin splitting of an Au (111) surface state band observed with angle resolved photoelectron spectroscopy. *Physical review letters*, 77(16):3419, 1996.

[107] Eli Rotenberg, JW Chung, and SD Kevan. Spin-orbit coupling induced surface band splitting in Li/W (110) and Li/Mo (110). *Physical review letters*, 82(20):4066, 1999.

[108] K. Y. Choi, P. Lemmens, I. Eremin, G. Zwicknagl, H. Berger, G. L. Sun, D. L. Sun, and C. T. Lin. Self-energy effects and electron-phonon coupling in fe-as superconductors. *J Phys Condens Matter*, 22(11):115802, 2010.

[109] A. Akrap, J. J. Tu, L. J. Li, G. H. Cao, Z. A. Xu, and C. C. Homes. Infrared phonon anomaly in $BaFe_2As_2$. *Physical Review B*, 80(18), 2009.

[110] L. Chauvière, Y. Gallais, M. Cazayous, A. Sacuto, M. Méasson, D. Colson, and A. Forget. Doping dependence of the lattice dynamics in $Ba(Fe_{1-x}Co_x)_2As_2$ studied by raman spectroscopy. *Physical Review B*, 80(9), 2009.

[111] Chetan Dhital, Z. Yamani, Wei Tian, J. Zeretsky, A. S. Sefat, Ziqiang Wang, R. J. Birgeneau, and Stephen D. Wilson. Effect of uniaxial strain on the structural and magnetic phase transitions in $BaFe_2As_2$. *Physical Review Letters*, 108(8):087001, 2012.

[112] ZP Yin, S Lebegue, MJ Han, BP Neal, SY Savrasov, and WE Pickett. Electron-hole symmetry and magnetic coupling in antiferromagnetic LaFeAsO. *Physical Review Letters*, 101(4):047001, 2008.

[113] E Aktürk and Salim Ciraci. First-principles study of the iron pnictide superconductor $BaFe_2As_2$. *Physical Review B*, 79(18):184523, 2009.

[114] T. Yildirim. Strong coupling of the Fe-spin state and the As-As hybridization in iron-pnictide superconductors from first-principle calculations. *Physical Review Letters*, 102(3):037003, 2009.

[115] II Mazin and MD Johannes. A key role for unusual spin dynamics in ferropnictides. *Nature Physics*, 5(2):141–145, 2009.

[116] Ni Ni, SL Budko, A Kreyssig, S Nandi, GE Rustan, AI Goldman, S Gupta, JD Corbett, A Kracher, and PC Canfield. Anisotropic thermodynamic and transport properties of single-crystalline $Ba_{1-x}K_xFe_2As_2$ (x= 0 and 0.45). *Physical Review B*, 78(1):014507, 2008.

[117] W. Z. Hu, J. Dong, G. Li, Z. Li, P. Zheng, G. F. Chen, J. L. Luo, and N. L. Wang. Origin of the spin density wave instability in AFe_2As_2(A=Ba,Sr) as revealed by optical spectroscopy. *Physical Review Letters*, 101(25), 2008.

[118] D. Wu, N. Bari?i?, P. Kallina, A. Faridian, B. Gorshunov, N. Drichko, L. J. Li, X. Lin, G. H. Cao, Z. A. Xu, N. L. Wang, and M. Dressel. Optical investigations of the normal and superconducting states reveal two electronic subsystems in iron pnictides. *Physical Review B*, 81(10), 2010.

[119] Xiang-Bai Chen, Nguyen Thi Minh Hien, D Lee, SY Jang, TW Noh, and In-Sang Yang. Resonant a1 phonon and four-magnon Raman scattering in hexagonal $homno_3$ thin film. *New Journal of Physics*, 12(7):073046, 2010.

[120] L Chauvière, Y Gallais, M Cazayous, MA Méasson, A Sacuto, D Colson, and A Forget. Raman scattering study of spin-density-wave order and electron-phonon coupling in $Ba(Fe_{1-x}Co_x)_2As_2$. *Physical Review B*, 84(10):104508, 2011.

[121] M Braden, W Reichardt, Y Sidis, Z Mao, and Y Maeno. Lattice dynamics and electron-phonon coupling in Sr_2RuO_4: Inelastic neutron scattering and shell-model calculations. *Physical Review B*, 76(1):014505, 2007.

[122] W Kress, U Schröder, J Prade, AD Kulkarni, and FW De Wette. Lattice dynamics of the high-t c superconductor $YBa_2Cu_3O_{7-x}$. *Physical Review B*, 38(4):2906, 1988.

[123] David J Singh and M-H Du. Density functional study of LaFeAsO$_{1-x}$F$_x$: a low carrier density superconductor near itinerant magnetism. *Physical Review Letters*, 100(23):237003, 2008.

[124] A. P. Baddorf and E. W. Plummer. Surface anharmonicity temperature dependence of phonon energies on Cu(110). *Journal of Electron Spectroscopy and Related Phenomena*, 1990.

[125] G. Herzberg. *Molecular Spectra and Molecular Structure -*. Number I. Read Books, 1989.

[126] Herbert B Rosenstock. Multiphonon absorption in alkali halides: Quantum treatment of Morse potential. *Physical Review B*, 9(4):1963, 1974.

[127] L Boeri, OV Dolgov, and AA Golubov. Is LaFeAsO$_{1-x}$F$_x$ an electron-phonon superconductor? *Physical Review Letters*, 101(2):026403, 2008.

[128] Chang Liu, GD Samolyuk, Y Lee, Ni Ni, Takeshi Kondo, AF Santander-Syro, SL Budko, JL McChesney, E Rotenberg, T Valla, et al. K-doping dependence of the fermi surface of the iron-arsenic Ba$_{1-x}$K$_x$Fe$_2$As$_2$ superconductor using angle-resolved photoemission spectroscopy. *Physical review letters*, 101(17):177005, 2008.

[129] DJ Lockwood and MG Cottam. The spin-phonon interaction in FeF2 and MnF2 studied by Raman spectroscopy. *Journal of Applied Physics*, 64(10):5876–5878, 1988.

[130] Surajit Saha, Surjeet Singh, B Dkhil, S Dhar, R Suryanarayanan, G Dhalenne, A Revcolevschi, and AK Sood. Temperature-dependent Raman and X-ray studies of the spin-ice pyrochlore Dy$_2$Ti$_2$O$_7$ and non-magnetic pyrochlore Lu$_2$Ti$_2$O$_7$. *Physical Review B*, 78(21):214102_1–214102_10, 2008.

[131] E Granado, A Garcia, JA Sanjurjo, C Rettori, I Torriani, F Prado, RD Sanchez, A Caneiro, and SB Oseroff. Magnetic ordering effects in the raman spectra of La$_{1-x}$Mn$_{1-x}$O$_3$. *Physical Review B*, 60(17):11879, 1999.

[132] Felix Yndurain and Jose M Soler. Anomalous electron-phonon interaction in doped LaFeAsO: First-principles calculations. *Physical Review B*, 79(13):134506, 2009.

[133] L. Boeri, M. Calandra, I. I. Mazin, O. V. Dolgov, and F. Mauri. Effects of magnetism and doping on the electron-phonon coupling in BaFe$_2$As$_2$. *Physical Review B*, 82(2), 2010.

[134] FP Marn and H Suhl. Spin-orbit coupling modulated by the electron-phonon interaction. *Physical review letters*, 63(4):442, 1989.

[135] A. Li, J. Ma, A. Sefat, M. McGuire, B. Sales, D. Mandrus, R. Jin, C. Zhang, P. Dai, and S. Pan. STM Studies on the Surface Structure of Ba122 iron pnictides cleaved at Low Temperature. In *APS Meeting Abstracts*, page 23008, March 2011.

[136] H. Shaked, J. D. Jorgensen, S. Short, O. Chmaissem, S. I. Ikeda, and Y. Maeno. Temperature and pressure effects on the crystal structure of $Sr_3Ru_2O_7$: Evidence for electronically driven structural responses. *Physical Review B*, 62(13):8725–8730, 2000. PRB.

[137] J. Rundgren. Optimized surface-slab excited-state muffin-tin potential and surface core level shifts. *Physical Review B*, 68(12), 2003.

[138] V. B. Nascimento, R. G. Moore, J. Rundgren, Jiandi Zhang, Lei Cai, R. Jin, D. G. Mandrus, and E. W. Plummer. Procedure for leedi?vstructural analysis of metal oxide surfaces: $Ca_{1.5}Sr_{0.5}RuO_4(001)$. *Physical Review B*, 75(3), 2007.

[139] Yoshiyuki Yoshida, Shin-Ichi Ikeda, Hirofumi Matsuhata, Naoki Shirakawa, C. Lee, and Susumu Katano. Crystal and magnetic structure of $Ca_3Ru_2O_7$. *Physical Review B*, 72(5), 2005.

[140] An-Ping Li, Kendal W. Clark, X. G. Zhang, and Arthur P. Baddorf. Electron transport at the nanometer-scale spatially revealed by four-probe scanning tunneling microscopy. *Advanced Functional Materials*, 23(20):2509–2524, 2013.

[141] Ismail, Jiandi Zhang, R. Matzdorf, T. Kimura, Y. Tokura, and E. Plummer. Surface lattice dynamics of layered transition metal oxides: Sr_2RuO_4 and $La_{0.5}Sr_{1.5}RuO_4$. *Physical Review B*, 67(3), 2003.

[142] M. Iliev, S. Jandl, V. Popov, A. Litvinchuk, J. Cmaidalka, R. Meng, and J. Meen. Raman spectroscopy of $Ca_3Ru_2O_7$: Phonon line assignment and electron scattering. *Physical Review B*, 71(21), 2005.

[143] U. Fano. Effects of configuration interaction on intensities and phase shifts. *Physical Review*, 124(6):1866–1878, 1961.

[144] M. N. Iliev, V. N. Popov, A. P. Litvinchuk, M. V. Abrashev, J. B?ckstr?m, Y. Y. Sun, R. L. Meng, and C. W. Chu. Comparative raman studies of $SrRuO_3$, Sr_2RuO_4 and $Sr_3Ru_2O_7$. *Physica B: Condensed Matter*, 358(1-4):138–152, 2005.

[145] H. L. Liu, S. Yoon, S. L. Cooper, G. Cao, and J. E. Crow. Raman-scattering study of the charge and spin dynamics of the layered ruthenium oxide Ca3Ru2O7. *Physical Review B*, 60(10):R6980–R6983, 1999. PRB.

[146] M. Crawford, R. Harlow, W. Marshall, Z. Li, G. Cao, R. Lindstrom, Q. Huang, and J. Lynn. Structure and magnetism of single crystal $Sr_4Ru_3O_{10}$: A ferromagnetic triple-layer ruthenate. *Physical Review B*, 65(21), 2002.

[147] Q. Gan, R. A. Rao, C. B. Eom, L. Wu, and F. Tsui. Lattice distortion and uniaxial magnetic anisotropy in single domain epitaxial (110) films of $SrRuO_3$. *Journal of Applied Physics*, 85(8):5297, 1999.

[148] Brendan J Kennedy and Brett A Hunter. High-temperature phases of $SrRuO_3$. *Physical Review B*, 58(2):653, 1998.

[149] SN Bushmeleva, V Yu Pomjakushin, EV Pomjakushina, DV Sheptyakov, and AM Balagurov. Evidence for the band ferromagnetism in $SrRuO_3$ from neutron diffraction. *Journal of magnetism and magnetic materials*, 305(2):491–496, 2006.

[150] Muhammed A Hossain, Z Hu, MW Haverkort, T Burnus, CF Chang, S Klein, JD Denlinger, H-J Lin, CT Chen, R Mathieu, et al. Crystal-field level inversion in lightly mn-doped $Sr_3Ru_2O_7$. *Physical review letters*, 101(1):016404, 2008.

Vita

Chen Chen was born in 1989 in Changchun City, Jilin Province, China. He attended University of Science and Technology of China for the Special Class for the Gifted Young in 2005, and finished his undergraduate study in physics in June 2009. In August 2009, he came to Louisiana State University to pursue doctoral study in condensed matter physics under advisor Dr. Ward Plummer. He is currently a candidate for the degree of Doctor of Philosophy in physics, which will be awarded in May 2016.